Doctoral theses at NTNU, 2023:442

Moein Assar

A Model Library for Oil/Water Emulsion Separation and Transport Processes

Doctoral thesis

NTNU
Norwegian University of Science and Technology
Thesis for the Degree of
Philosophiae Doctor
Faculty of Natural Sciences
Department of Chemical Engineering

NTNU
Norwegian University of
Science and Technology

Moein Assar

A Model Library for Oil/Water Emulsion Separation and Transport Processes

Thesis for the Degree of Philosophiae Doctor

Trondheim, December 2023

Norwegian University of Science and Technology
Faculty of Natural Sciences
Department of Chemical Engineering

NTNU
Norwegian University of
Science and Technology

NTNU
Norwegian University of Science and Technology

Thesis for the Degree of Philosophiae Doctor

Faculty of Natural Sciences
Department of Chemical Engineering

ISBN 978-82-326-7586-9 (printed ver.)
ISBN 978-82-326-7585-2 (electronic ver.)
ISSN 1503-8181 (printed ver.)
ISSN 2703-8084 (online ver.)

Doctoral theses at NTNU, 2023:442

Printed by NTNU Grafisk senter

PREFACE

This PhD thesis is submitted to the Norwegian University of Science and Technology (NTNU) for partial fulfillment of the requirements for the degree of doctor of philosophy. The PhD was carried out from Oct. 2019 to Sep. 2023 at the Department of Chemical Engineering, NTNU. This work has been conducted under the supervision of Assoc. Prof. Brian Arthur Grimes and co-supervision of Prof. Magne Hillestad and Prof. Audun Faanes. The doctoral study was funded by SUBPRO which is a center for research-based innovation (SFI) within subsea production and processing. The research center is funded by the research council of Norway, and several industry partners.

Acknowledgements

I could not have finished this Ph.D. study without the help of everyone involved in this project. Many people deserve thanks for sharing their knowledge, motivation, and support.

I want to start by thanking my supervisor, Associate Professor Brian Arthur Grimes, for his unwavering support and guidance during my Ph.D. journey. I'd also like to express my gratitude to my co-supervisor, Professor Magne Hillestad, and my industrial co-supervisor, Professor Audun Faanes, for their invaluable support. Their insights, expertise, and encouragement have been truly appreciated.

I am grateful to my colleagues and friends at NTNU, Department of Chemical Engineering, and particularly at Ugelstad Laboratory, for creating an open and collaborative environment.

This research is a part of SUBPRO, a center for Research-based Innovation (SFI) in subsea production and processing (www.ntnu.edu/subpro/). I'd like to thank everyone involved in SUBPRO for allowing me to be a part of this great community. Special thanks to Professor Sigurd Skogestad, Pål Jarle Aune, and Esma Benzaim. Your support has been much appreciated.

Additionally, I want to extend my thanks to Sebastien Simon and Hamidreza Asaadian for their invaluable assistance with experimental data and sincere guidance. I'd also like to express my appreciation to Total Energies for granting permission to use and publish their experimental data.

Lastly, I would like to acknowledge that this thesis represents not just my individual effort, but also contributions of my loved ones. I would like to express my deepest gratitude to my wife Parvaneh Zavareh for her unwavering support and encouragement. I am also immensely thankful to my adorable daughter Tara, who brought joy, laughter, and a sense of perspective to my life during these challenging academic pursuits.

Summary

In the petroleum industry, the separation and transportation of multiphase fluids, especially crude-oil and water emulsions, hold immense economic and environmental significance. Thus, development of fundamentally advanced, yet simply implemented, models for these processes would be invaluable for engineers engaged in designing and optimizing transport and separation processes.

To develop models for multiphase separation and transport processes, accounting for factors like dispersed phase droplet size distribution, a population balance model is indispensable. These models offer a theoretical foundation to simulate processes involving droplet interactions, sedimentation, and creaming, which collectively influence the evolution of droplet size distributions over time, and this understanding is crucial for predicting physical properties as well as separation equipment efficiencies.

This project's central objective involves incorporating fundamental droplet coalescence and breakage modeling into a population balance model framework. We have developed a C++ class library for dynamic drop size evolution in 0, 1, and 2 spatial dimensions, specifically tailored for modeling crude oil/water emulsion processes. Leveraging C++'s class inheritance structure, we've enabled a modular approach to develop transport and separation models of varying complexity. Coupled with C++'s memory handling capabilities and existing parallel computational libraries for solving differential equations, this ensures rapid calculations on modern computational platforms.

Furthermore, we have addressed various challenges associated with these models during this project.

Table of Contents

Chapter 1

1. Introduction

1.1. Background and motivation

The separation and transport of multiphase fluids, particularly liquid-liquid dispersions in the form of crude-oil and water emulsions, is an economically and environmentally crucial process in the petroleum industry [1]. Consequently, the development of fundamentally advanced, yet simply implemented, models for separation and transport of multiphase fluids would be a valuable tool for process and system engineers tasked with designing, controlling, and optimizing transport and separation processes.

A key challenge for researchers in multiphase transport modelling is the compromise between computational performance and the level of physical abstraction employed in the model development. Very simple models with a high degree of physical abstraction can have excellent computational performance at the cost of poor predictive performance for a wide variety of conditions [2–7]. These simple models often treat the multiphase system as single phases with peculiar properties or, at best, represent the dispersed phase with a single representative characteristic length scale (e.g., drop/bubble size). However, it has been shown that the behaviour of multiphase separation and transport systems is strongly dependent on the droplet size distribution (DSD) of the dispersed phase, especially with respect to coalescence and mass transfer [1,8]. Thus, the droplet size distribution of the dispersed phase is an essential feature that should be included into multiphase separation and transport models to improve predictive capabilities.

Development of multiphase separation and transport models that account for the dispersed phase DSD along with coalescence and breakage phenomena requires a rigorously defined population balance model (PBM) [1] to efficiently link model variables to real and measurable system quantities as well as to ensure scalability [9] of the models. These models provide basically a theoretical framework to model processes involving interaction between droplets as well as sedimentation/creaming, which eventually leads to the dynamic evolution of the DSD. The knowledge of the DSD can play an essential role in predicting physical properties of the fluid as well as determining the efficiency of process equipment. PBMs can easily become computationally

cumbersome while their development and implementation are generally beyond the scope of the professional training for many process and system engineers. Therefore, process and system engineers working to develop multiphase separation and transport processes would benefit greatly from a model library that can generate fast solutions of population balance equations of varying degrees of complexity as well as to be easily "wrapped" into their simulation software of choice.

In the other hand, these models can also allow researchers in industry and academia to utilize the results of coalescence and breakage studies for estimation of model parameters without having to construct advanced models themselves.

1.2. Research objectives

The core activity of this project is to employ the fundamental knowledge about coalescence and breakage modeling in a population balance model framework to construct a class-library in C++ for simulating the dynamic evolution of a droplet size distribution in 0, 1, and 2 spatial dimensions. The application of this library is to model processes involving crude oil/water emulsion. The class inheritance structure of the C++ language has been utilized to facilitate a modular approach for development of transport and separation models with varying complexity suited to different tasks while the memory handling of C++ and existing parallel computational libraries for the solution of differential equations ensures fast calculation speeds on modern computational platforms. Therefore, in this project a multidimensional C++ class library of population balance models has been developed that can utilize user defined coalescence and breakage relations and be used to construct modular process models involving multiphase fluids. Additionally, in this project along with building and developing the models, we have tried to address some of the challenges associated with these models. These issues are captured in the following research objectives:

Efficient and robust numerical solvers for PBMs

The fast and reliable numerical solutions for PBMs is crucial in this project. Specifically, we focused on tackling challenges associated with the numerical solutions of PBMs. These challenges can be summarized as follows:

- **Proper choice of truncation points for the droplet size coordinate**

  A PBM describes the polydispersity of droplet sizes in a dispersion system. In cases involving breakage and coalescence phenomena, this is mathematically represented by integral terms with an integration bound extending to infinity. To numerically tackle these terms, one must truncate the droplet size coordinate at a finite value. This choice can have a significant impact on the accuracy and efficiency of the solution [10]. Specifically, underestimation leads to inaccurate numerical results, while overestimation results in a set of stiff equations, causing computational inefficiency in the numerical solution.

- **Fast and reliable numerical solvers for steady-state PBMs**

  Numerical solution of steady-state PBMs to obtain the equilibrium DSDs is another challenge. This occurs typically in situations where the equations exhibit strong non-linearity, making it challenging to directly achieve a stable, equilibrium solution [10,11].

- **High dimensionality of the equations**

  When spatial dimensions are incorporated into the system, the number of discretized equations expand rapidly, making their solution numerically demanding. In this context, utilizing techniques that provide accurate solutions with coarse grids can be a potential solution.

Interfacial coalescence rate and formation of dense packed layer

In a gravity separator, the dispersion system is under the influence of the gravity. As a result, droplets of the dispersed phase move toward the interface level between the two immiscible phases where they can coalesce and integrate with the continuous phase in the adjacent dispersion layer. The rate at which this coalescence occurs can dictate whether a dense packed layer (DPL, a collection of dispersed-phase droplets densely packed with a high volume fraction) forms or not [12]. Within this layer, the dispersed phase volume fraction can significantly increase because of polydispersity and the droplets' inclination to deform under the compressive force exerted from the droplets above. A better understanding of the underlying mechanisms for interfacial coalescence can significantly improve the predictive capabilities of such separation models. Additionally, a proper

mathematical description of the problem can mitigate the oversimplification normally used in building these advection-diffusion PBMs which can eventually lead to unrealistic volume fraction predictions, potentially exceeding the physical boundary of unity.

To address the aforementioned issue, a collaboration was established with another research project conducted at the Ugelstad Laboratory. The experimental findings from that project, which includes NMR experiments using a stabilized model oil-in-water system, were employed to fine-tune the batch separation model, and tackle the challenges outlined above.

Extending PBMs to continuous gravity separators

To develop a versatile model for the continuous gravity separation problem, several key aspects must be taken into account. The model should incorporate the hydrodynamic characteristics of these systems, including velocity fields and turbulence intensity. It should also account for various mechanisms involved in droplet breakage and coalescence. This consideration becomes especially vital when simulating both operational scenarios and non-operational cases (e.g., transient situations like start-up and shutdown).

Furthermore, it is essential to experimentally validate and tune such models. To accomplish this, a collaboration has been established with another SUBPRO sub-project focused on experimental studies of subsea oil-water bulk separation in pipe separators.

1.3. Thesis outline

Chapter 1 introduces the project's background, highlighting the need for creating a model library for multi-fluid separation and transport applications. It outlines potential applications and discusses the current challenges and gaps in modeling these processes. Additionally, the chapter provides an overview of the thesis structure and includes a list of related publications.

Chapter 2 provides information regarding the library's structure and the philosophy behind program development. It introduces various classes within the library as well as descriptions of the techniques and external dependencies employed. The chapter also contains a short literature review of mathematical discretization and solution techniques

used for population balance equations. Furthermore, it delves into different modules within the library and explains the possibility of performing modular simulations.

Chapter 3 introduces the mathematical model for spatially homogeneous dispersion systems using a 0D-PBM. It describes the numerical discretization and solution technique employed. The chapter also outlines an approximate approach for estimating the time and length scales of the system, addressing a key challenge associated with numerical solutions of PBMs, which involves selecting an appropriate truncation point for the internal domain.

Chapter 4 outlines the 1D-PBM model that has specifically been developed for batch oil-water separators. It delves into various constituent relations and sub-models that have been incorporated. Emphasis has been placed on modeling the formation of the dense pack layer and ensuring physical volume fraction within the system. Additionally, the chapter includes a comprehensive comparison of experimental results with model predictions, along with a detailed description of the model parameter estimation. Information regarding the numerical discretization and solution techniques employed are also provided in the chapter.

Chapter 5 outlines the model developed for continuous oil-water separators. It presents the modeling of various sections of a 3-phase separator, encompassing both the inlet section and the separation section. The chapter provides a comprehensive description of various constituent relations and sub-models integrated into each section's model. Furthermore, the chapter covers the description of steady-state and transient solvers, elaborating on the mathematical strategies and solution techniques employed. In addition, it includes a comparison of experimental results with model predictions.

Chapter 6 focuses on the application of spectral discretization within circular geometries through the utilization of geometric transformations. It elucidates how to mathematically tackle the circular segment geometries formed in two and three-phase flows, as well as two and three-phase gravity separators, which is critical for extending the continuous separation model to 3D. The chapter provides a comprehensive overview of numerical

procedures for solving partial differential equations (PDE) within circular geometries, accommodating various boundary conditions for both steady-state and transient scenarios. It also thoroughly addresses various implementation considerations and discusses several aspects of these techniques, including their error characteristics and computational efficiency. Furthermore, the chapter presents a study that applies this technique to solve the simplified Navier-Stokes equations for two and three-phase multi-fluid gravity flows in sloped pipes.

Chapter 7 presents the conclusions drawn from this project as well as insights, and recommendations for future research.

1.4. List of publications

Journal publications

I- Moein Assar, Brian Arthur Grimes, A new approach to analyze the equilibrium and transient behaviors of particulate systems and the subsequent application to multiphase fluid systems, Chemical engineering research and design, 188 (2022) 1083-1096.

II- Moein Assar, Sebastien Charles Roger Simon, Geir Sørland, Brian Arthur Grimes, A theoretical and experimental investigation of batch oil-water gravity separation, Chemical engineering research and design, 194 (2023)136-150.

III- Moein Assar, Hamidreza Asaadian, Milan Stanko, Brian Arthur Grimes, A theoretical and experimental investigation of continuous oil-water gravity separation, Prepared manuscript.

IV- Moein Assar, Brian Arthur Grimes, Geometrically transformed spectral methods to solve partial differential equations in circular geometries, application for multi-phase flow, Mathematics and Computers in Simulation, 215 (2024) 456-475.

Thesis is based on the above four papers.

Other publications

Karthik Raghunathan, Moein Assar, Sulalit Bandyopadhyay, Brian Arthur Grimes, The shapes of gold nanoparticles: modelling symmetry breaking by solving a moving boundary, prepared manuscript.

Mahdi Ahmadi, Moein Assar, Arne Lindbråthen, Eivind Johannessen, Liyuan Deng, Magne Hillestad, Subsea Natural Gas Dehydration with Membrane Processes: Process Design and Optimization, prepared manuscript.

Oral presentations

Moein Assar, Sebastien Charles Roger Simon, Brian Arthur Grimes, Population balance model for gravitational separation; axial dispersion and densely packed volume fraction restriction, 7th International Conference on Population Balance Modeling (PBM 2022), May 2022, Lyon, France.

Poster presentations

Moein Assar, Brian Arthur Grimes, A new approach to analyze the equilibrium and transient behaviors of particulate systems with breakage and coalescence, 7th International Conference on Population Balance Modeling (PBM 2022), May 2022, Lyon, France.

Moein Assar, Hamidreza Asaadian, Milan Stanko, Brian Arthur Grimes, A novel population balance model for subsea multi-parallel pipes separator, 28th underwater technology conference, June 2022, Bergen, Norway.

1.5. Declaration of authorship

The thesis is organized as a compilation of four papers, with three of them already published and one in preparation. The declaration of co-authorship is outlined as follows:

Paper I- Moein Assar, Brian Arthur Grimes, A new approach to analyze the equilibrium and transient behaviors of particulate systems and the subsequent application to multiphase fluid systems, Chemical engineering research and design, 188 (2022) 1083-1096.

Moein Assar is responsible for developing the mathematical model, creating computational programs, writing the manuscript, and organizing the manuscript submission and revision. Brian Arthur Grimes contributed to scientific discussions,

reviewing and revision of the manuscript, and provided overall supervision for the project.

Paper II- Moein Assar, Sebastien Charles Roger Simon, Geir Sørland, Brian Arthur Grimes, A theoretical and experimental investigation of batch oil-water gravity separation, Chemical engineering research and design, 194 (2023)136-150.

Moein Assar was responsible for developing the mathematical model, creating computational programs, writing the manuscript, and organizing the manuscript submission and revision. Sebastien Simon collected and organized the experimental data and authored the experimental section and was also involved in the scientific discussions. Geir Sørland was involved in the experimental activities and contributed to scientific discussions. Brian Arthur Grimes was involved in building the mathematical model, scientific discussions, reviewing and revision of the manuscript, and provided overall supervision for the project.

Paper III- Moein Assar, Hamidreza Asaadian, Milan Stanko, Brian Arthur Grimes, A theoretical and experimental investigation of continuous oil-water gravity separation, Prepared manuscript.

Moein Assar was responsible for developing the mathematical model, creating computational programs, writing the manuscript. Hamidreza Asaadian collected and organized the experimental data and authored the experimental section. Milan Stanko was involved in the experimental activities and contributed to scientific discussions. Brian Arthur Grimes was involved in building the mathematical model, scientific discussions, reviewing the manuscript, and provided overall supervision for the project.

Paper IV- Moein Assar, Brian Arthur Grimes, Geometrically transformed spectral methods to solve partial differential equations in circular geometries, application for multi-phase flow, Mathematics and Computers in Simulation, 215 (2024) 456-475.

Moein Assar is responsible for developing the mathematical model, creating computational programs, writing the manuscript, and organizing the manuscript submission and revision. Brian Arthur Grimes contributed to scientific discussions, reviewing and revision of the manuscript, and provided overall supervision for the project.

1.6. References

[1] B.A. Grimes, Population balance model for batch gravity separation of crude oil and water emulsions. part I: Model formulation, J. Dispers. Sci. Technol. 33 (2012) 578–590. https://doi.org/10.1080/01932691.2011.574946.

[2] S. Hartland, S.A.K. Jeelani, Choice of model for predicting the dispersion height in liquid/liquid gravity settlers from batch settling data, Chem. Eng. Sci. 42 (1987) 1927–1938. https://doi.org/10.1016/0009-2509(87)80139-2.

[3] S.A.K. Jeelani, S. Hartland, The continuous separation of liquid/liquid dispersions, Chem. Eng. Sci. 48 (1993) 239–254. https://doi.org/10.1016/0009-2509(93)80012-F.

[4] S.A.K. Jeelani, R. Hosig, E.J. Windhab, Kinetics of low Reynolds number creaming and coalescence in droplet dispersions, AIChE J. 51 (2005) 149–161. https://doi.org/10.1002/aic.10283.

[5] S.A.K. Jeelani, S. Hartland, Effect of Dispersion Properties on the Separation of Batch Liquid-Liquid Dispersions, Ind. Eng. Chem. Res. 37 (1998) 547–554. https://doi.org/10.1021/ie970545a.

[6] M. Henschke, L.H. Schlieper, A. Pfennig, Determination of a coalescence parameter from batch-settling experiments, Chem. Eng. J. 85 (2002) 369–378. https://doi.org/10.1016/S1385-8947(01)00251-0.

[7] T. Das, C.J. Backi, J. Jäschke, A model for subsea oil-water gravity separator to estimate unmeasured disturbances, in: Comput. Aided Chem. Eng., Elsevier B.V., 2017: pp. 1489–1494. https://doi.org/10.1016/B978-0-444-63965-3.50250-6.

[8] K. Kovalchuk, E. Riccardi, B.A. Grimes, Multiscale modeling of mass transfer and adsorption in liquid-liquid dispersions. 2. application to calcium naphthenate precipitation in oils containing mono- and tetracarboxylic acids, Ind. Eng. Chem. Res. 53 (2014) 11704–11719. https://doi.org/10.1021/ie501296t.

[9] C.J. Backi, B.A. Grimes, S. Skogestad, A Control- and Estimation-Oriented Gravity Separator Model for Oil and Gas Applications Based upon First-Principles, Ind. Eng. Chem. Res. 57 (2018) 7201–7217. https://doi.org/10.1021/acs.iecr.7b04297.

[10] S. Rigopoulos, A.G. Jones, Finite-element scheme for solution of the dynamic population balance equation, AIChE J. 49 (2003) 1127–1139.

https://doi.org/10.1002/aic.690490507.

[11] Z. Zhu, C.A. Dorao, H.A. Jakobsen, Mass Conservative Solution of the Population Balance Equation Using the Least-Squares Spectral Element Method, (n.d.). https://doi.org/10.1021/ie900710y.

[12] B. Panjwani, A. Amiri, S. Mo, M. Fossen, H. Linga, V. Pauchard, Dense Packed Layer Modeling in Oil-Water Dispersions: Model Description, Experimental Verification, and Code Demonstration, (2015). https://doi.org/10.1080/01932691.2014.1003221.

Chapter 2

2. Computational program and library structure

2.1. Numerical solution of population balance models

The droplet size distribution (DSD) in dispersion systems can be modeled using a population balance model (PBM). This knowledge of the DSD can play an essential role in predicting physical properties and determining the efficiency of process equipment. Applying population balance models to complex multiphase fluid systems usually entails accounting for extra phenomena acting on the DSD. Examples of such phenomena, other than breakage and coalescence, are gravitational effects on the droplets as well as flow dynamics. Additionally, these complex systems typically demand adding external spatial dimensions to the model. The population balance equation (PBE) for these systems can be formulated by considering advection and dispersion terms, as shown below:

$$\frac{\partial f_n(v,t,\mathbf{r})}{\partial t} - \nabla.[D(v,t,\mathbf{r})\nabla f_n] + \nabla.[\mathbf{u}(v,t,\mathbf{r})f_n] = +B_+ - B_- + C_+ - C_- \qquad (2.1)$$

where f_n represents the number density distribution with functionality in terms of droplet size (v), time (t), and spatial coordinate ($\mathbf{r}$), D is the dispersion coefficient, $\mathbf{u}$ is the droplet velocity vector, and ∇ is the del operator representing the gradient.

The right-hand side of the Eq. 1 comprises the accumulation term, dispersion term, and convection term, while the left-hand side of the equation includes source terms involving four birth and death rates according to breakage and coalescence phenomena.

In the case of binary droplet breakage, the rates for breakage birth (B_+) and death (B_-) can be expressed in the following forms:

$$B_+(v,t,\mathbf{r}) = \int_v^\infty 2g(v',t,\mathbf{r})\beta(v',v)f_n(v',t,\mathbf{r})\,dv' \qquad (2.2)$$

$$B_-(v,t,\mathbf{r}) = g(v,t,\mathbf{r})f_n(v,t,\mathbf{r}) \qquad (2.3)$$

where g represents the frequency for binary droplet breakage, and β represents the daughter droplet distribution. The daughter droplet distribution pertains to the range of smaller particle sizes generated as a consequence of the breakage of larger parent particles. Mathematically, this term is articulated through a probability density function, and its purpose is to ensure the continuity of the overall size distribution with that of the parent particles. This probability density function must possess essential properties to ensure the conservation of both number and volume throughout the distribution.

Meanwhile, the birth and death rates resulting from coalescence (C_+ and C_-, respectively) take the following forms:

$$C_+(v,t,\mathbf{r}) = \int_0^{\frac{v}{2}} k_c(v', v-v', t, \mathbf{r}) f_n(v', t, \mathbf{r}) f_n(v-v', t, \mathbf{r})\, dv' \tag{2.4}$$

$$C_-(v,t,\mathbf{r}) = f_n(v,t,\mathbf{r}) \int_0^{\infty} k_c(v', t, \mathbf{r}) f_n(v', t, \mathbf{r}) dv' \tag{2.5}$$

where k_c is the coalescence rate between droplets.

There are certain challenges associated with discretizing the internal coordinate (i.e., droplet size) and numerically solving the PBMs. This is particularly the case when the DSD exhibits significant variations over extensive size and time ranges [1]. These challenges can be summarized as follows [2,3]:

- the computationally demanding evaluation of the nonlinear integral source terms,
- establishing a reliable numerical method for discretizing birth and death rate terms to ensure internal consistency, particularly in conserving mass and number densities,
- making a suitable choice for the upper bound of the integrals (∞) to ensure a robust and reliable solution,
- ensuring proper grid generation and the solution's robustness to achieve grid-independent results,
- attaining equilibrium in situations when one of the kernels dominates,
- establishing reliable time integration for the discretized system of ordinary differential equations (ODE), which is often stiff.

As a result, many researchers have developed specialized algorithms to numerically simulate these systems. An efficient class of numerical methods used to solve PBMs are the method of moments (MOM). This approach is most frequently employed in coupling PBMs with computational fluid dynamics (CFD) [4]. These methods transform the population balance equation (PBE) into a set of statistical moment transport equations. Instead of a DSD, it predicts the first few statistical moments (e.g., total number or total volume) of the DSD, which can be adequate for many applications. Therefore, direct information of the DSD is inherently lost [4]. However, it is possible to reproduce the DSD even though it lacks uniqueness [1]. In this approach, the set of transformed equations is unclosed; this necessitates approximations to provide closure. Consequently,

the source terms in the PBM can be closed by expressing them as lower-order moments. Various choices for closure has led to variations in these methods [5] where some examples are shown below [6]:

- polynomial closure,
- minimum entropy closure,
- Kershaw closure,
- quadrature-based closures such as:
    - direct quadrature closure,
    - extended quadrature closure,
    - conditional quadrature closure,
    - extended conditional quadrature closure,
    - hyperbolic quadrature closure.

In multiphase flow, where only the dispersed droplet/bubble size is needed as an input from the population balance equation, as few as four moments can often be enough [7]. Different variations of these methods have been proposed, where the most well accepted approaches are:

- quadrature method of moments (QMOM),
- direct quadrature method of moments (DQMOM).

These methods have a low computational cost, and the set of moment ODEs is non-stiff, making it easy to couple them with a CFD solver. Another advantageous feature of these moment methods is that they effectively conserve droplet mean and integral properties. However, all these advantages come at the expense of losing direct information of the DSD shape. Reconstructing the DSD from its low-order moments can encounter issues related to uniqueness and stability, often resulting in the assumption of parametrized distributions like the generalized lambda family distributions [6]. Another limitation is that extending these methods to bivariate and higher dimensions of the dispersed phase space is not well-established and still relies on problem-dependent formulations [6].

On the contrary, sectional or class methods and weighted residue methods are considered numerical schemes that directly give the DSD. In sectional methods, the continuous PBE is discretized to a finite number of classes in which the DSD is assumed to be uniform. The main concern here is to redistribute the newly formed droplets in such a way to

conserve one or more of the moment properties of the DSD [8]. The fixed and moving pivot techniques developed by Kumar and Ramkrishna [9,10] and the cell-average technique by Kumar et al. [11] are the most well-established methods in this class. Another alternative approach is the conservative finite-volume method which is based on a conservative form of the PBE [12]. Despite the moment preserving properties, all these methods usually demand many sections to describe the DSD adequately.

Other popular techniques are the weighted residue methods. Same as sectional methods, these methods also directly provide information on the shape of the DSD. Nevertheless, they offer significantly faster convergence resulting in higher accuracy [13,14]. This feature enhances computational efficiency. In simpler terms, when using coarser grids, they can achieve the same level of accuracy as other methods [15].

In this approach, we approximate the dependent variable using a truncated series of trial functions across the entire computational domain. Simultaneously, we minimize the product of the governing equation and the test function [13]. Variations of these techniques have been developed using different trial and test functions, including Galerkin, Tau, collocation, and least square methods. In collocation technique, the test function is a Dirac delta, ensuring that the governing equations are satisfied at the collocation points [13]. Additionally, the implementation of the collocation method is straightforward and computationally more efficient, while providing accuracy and stability similar to the Galerkin method [13,16].

To enhance the flexibility of these techniques, some researchers have also utilized them in an element-based framework [2,17–23]. These element approaches can provide the opportunity to generate more robust grids based on preliminary knowledge about the distribution of the droplet size.

2.2. Model structure of the library

The model library encompasses various applications related to the separation and transport of oil-water emulsions. As previously mentioned, population balance equations are employed as an essential component in these models for multiphase flow modeling. Depending on the complexity and external dimensions involved, three modules are envisaged for modeling various applications, as illustrated in Figure 2-1.

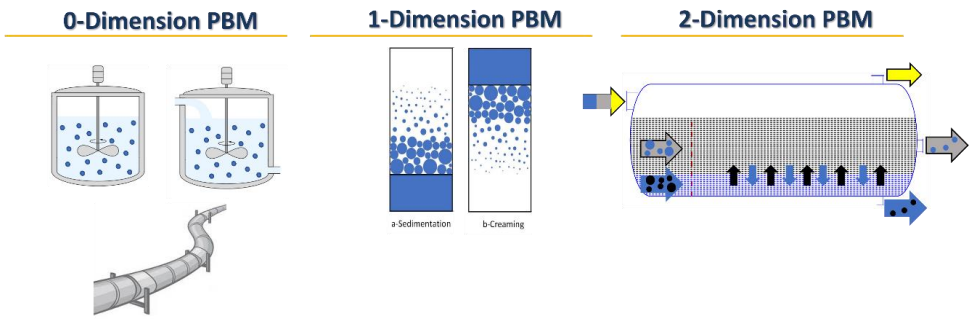

Figure 2-1: 0, 1 & 2 dimensional PBM applications.

The modules together with the underlining assumptions, sub-models, and applications are summarized in Table 1.

Table 2-1: Description of the library's different modules.

Modules	Physics	Solver	Industrial Application
0D-PBM	**Spatial homogenous mixer:** ✓ inflow and outflow ✓ binary droplet breakage ✓ droplet coalescence	steady-state, transient	inlet section of 3-phase separator
	Homogenous pipe flow: ✓ binary droplet breakage ✓ droplet coalescence	steady-state	fully turbulent oil/water pipe
1D-PBM	✓ gravitational sedimentation / rising of droplets ✓ droplet coalescence ✓ interfacial coalescence ✓ moving interface between the layers ✓ dense packed layer formation (diffusion model)	transient	batch gravitational separation including sedimentation and creaming
2D-PBM	✓ velocity profile (plug flow or laminar profile) ✓ gravitational sedimentation / rising of droplets ✓ binary droplet breakage ✓ droplet coalescence (buoyancy-induced and turbulent-induced) ✓ interfacial coalescence ✓ dense packed layer formation (diffusion model) ✓ dispersed phase volume transfer between layers and axially variable flow rates ✓ transient level change and spatial transformation of cross-section	steady-state, transient	3-phase separator, multi-parallel pipe separator

A combination of these modules can simultaneously be employed in a modular simulation to model complex processes in oil production, transport, and processing. This approach could enable the tracking of the DSD through transport and separation facilities, thereby facilitating a more realistic estimation of separation equipment efficiency. For instance, a 3-phase separator can be more realistically simulated by considering the upstream facilities in the model. In this approach, the upstream pipeline and valve can be modeled using 0D-PBM modules. To model a 3phase separator, we can divide it into two parts: the inlet section and the separation section. The inlet section can be modeled using two coupled 0D-PBM modules, while the separation section can be simulated using two sets of coupled 2D-PBM modules for the oil continuous and water continuous layers. The schematic of this configuration is depicted in Figure 2-2.

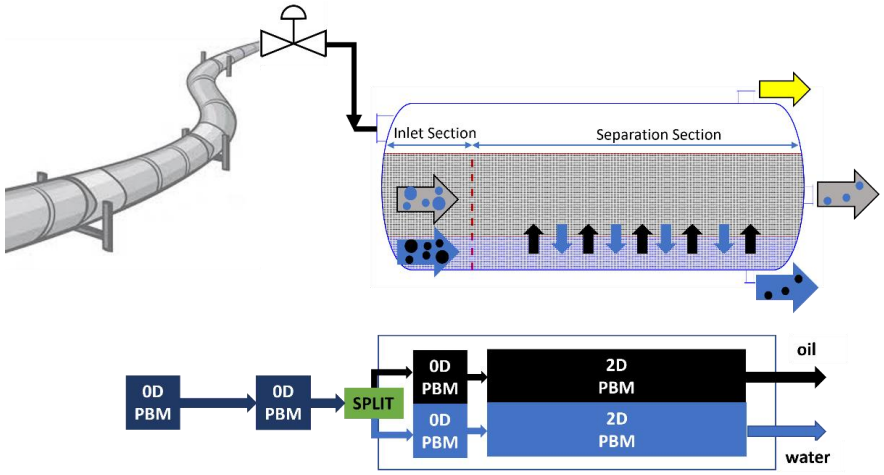

Figure 2-2: Stepwise and parallel configurations of modules to perform modular modeling.

2.3. Code structure of the library

The models are programmed in C++ in a modular way using object-oriented features of C++. Special attention has been devoted to portability as well as the computational efficiency of the programs. The latter case is critical as these models can quickly become computationally demanding by increasing the number of dimensions considered for the model. The primary principles for developing the C++ library are outlined as follows:

- modular design using object-oriented features of C++,
- portability and potentially easy linkage to external software,
- computationally efficient using optimized codes,
- readable, reusable, and simple to maintain codes,
- integration of efficient external libraries into the library if required,
- extendibility.

Furthermore, the library structure is designed in four layers as:

- pre-processing classes,
- solver classes,
- post processing classes,
- utility classes.

Figure 2-3 shows the class structure diagram of the library, providing an overview of the program's class organization and relationships. Furthermore, Figure 2-4 presents a flowchart illustrating the flow of data and interactions among various program components.

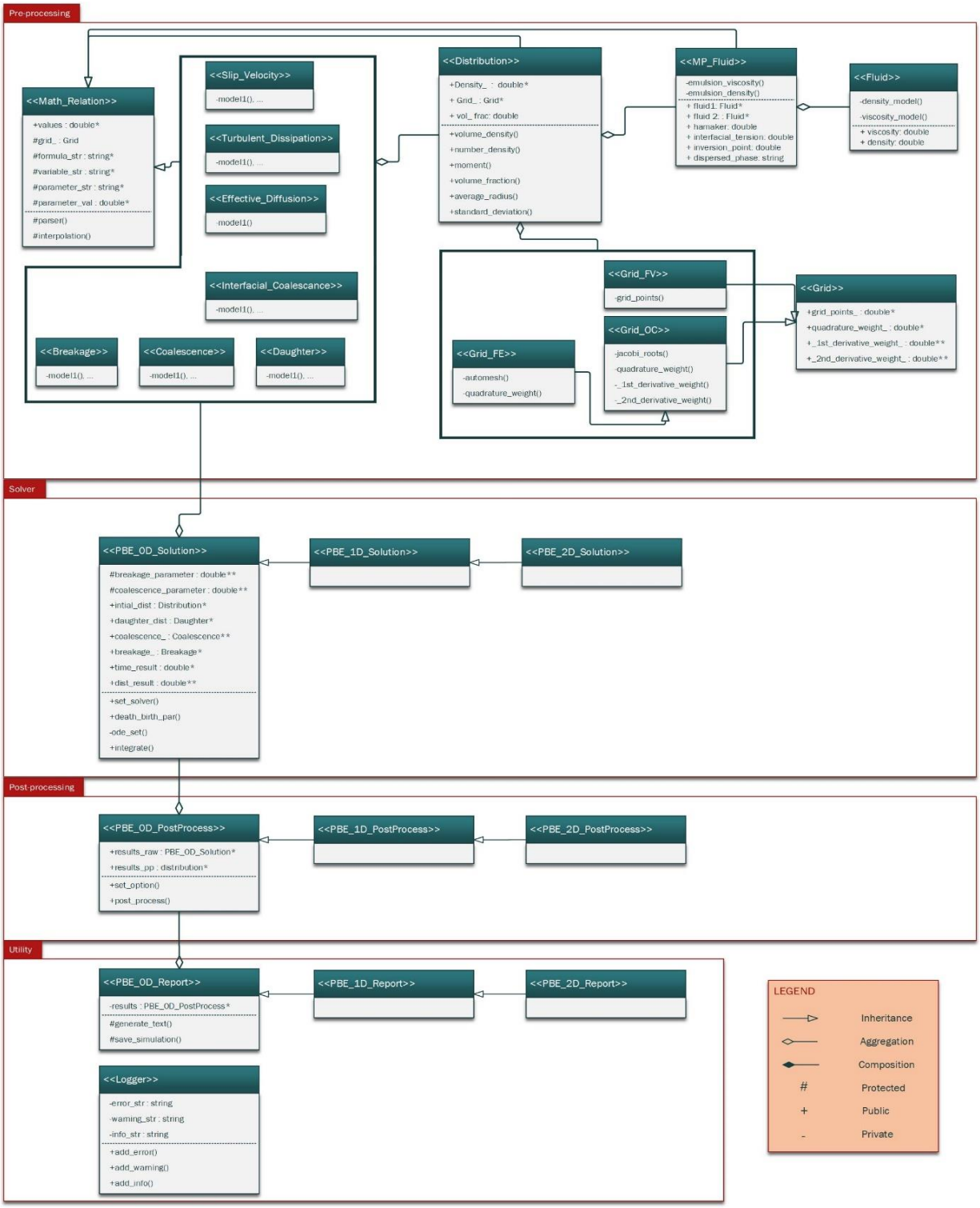

Figure 2-3: Class structure of the library.

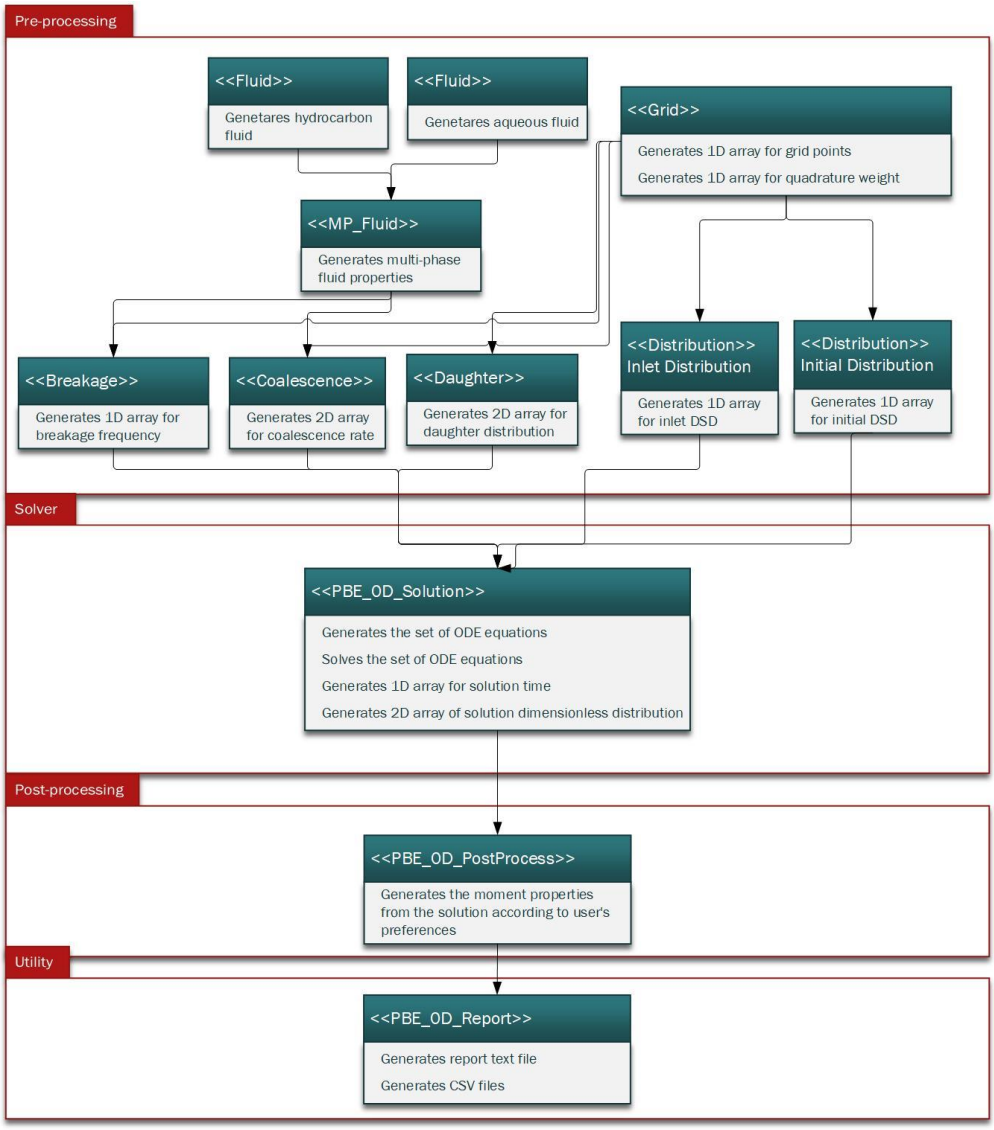

Figure 2-4: Data flow diagram for 0D-PBM.

In the following sections, we will delve deeper into the discussion of these program elements.

2.3.1. Preprocessing classes

In the pre-processing layer, the physics of the problem, as well as the choice of numerical grids, are specified. The following is a list of constituent relations and sub-models required to configure the problem for different modules of the library:

- coalescence rate,
- breakage frequency,
- daughter droplet distribution,
- interfacial coalescence time,
- droplet slip velocity,
- effective diffusion,
- turbulent energy dissipation rate.

In addition to the above list, to set up a problem, one needs to define the following inputs:

- initial and boundary DSDs,
- multiphase fluid physio-chemical properties.

Several strategies are envisioned for the user's input data entry, which are summarized as follows:

- In-built functions for constituent sub-models, including available models from the literature, which are programmed inside each related class.
- Parsing strings into mathematical relations using the inherited functionality from the "Math Relation" superclass.
- User-specified data and mapping the data to the grid points using interpolation methods inherited from the "Math Relation" superclass.

Math relation super class

This is the parent class, encompassing the primary functionalities for defining various mathematical relations by utilizing an external dependency (expression parser toolkit, ExprTk). With this capability, mathematical expressions (in the form of strings) containing multiple independent variables and parameters can be parsed, and their numerical values can be computed at grid points.

Furthermore, this superclass also integrates the necessary functionality for various interpolation methods to map user-specified data onto the grid points. The programmed interpolation techniques include:

- Jacobi interpolation,
- monotone piecewise cubic Hermite interpolation polynomial (MPCHIP).

As depicted in Figure 2-3, many classes in the preprocessing layer inherit the functionalities from this superclass. This enables specifying various constituent models using these capabilities.

Distribution class

This class serves two primary purposes:

- defining the initial and boundary distributions,
- Post-processing of simulation results.

The log-normal distribution is available as an in-built function. However, distributions can also be generated using user-specified data and the inherited interpolation functionality from the "Math Relation" superclass.

Additionally, the class possesses the necessary functionality to generate secondary variables such as various radius-based, volume-based, dimensional, and dimensionless variables. The list of these secondary variables extracted from a distribution is as follows:

- volume density,
- number density,
- statistical moments of different order,
- total droplet number,
- volume fraction,
- average droplet radius,
- average droplet volume,
- standard deviation,
- Sauter mean droplet radius,
- surface to volume ratio.

Grid classes

These classes are equipped with the necessary internal functionalities and attributes for discretizing continuous partial integro-differential equations.

For the internal domain, a class based on the spectral-element orthogonal collocation technique [24] has been incorporated. The selection of elements' boundaries can be customized based on initial and boundary DSDs, as well as estimated length scales using the developed approximation technique in this project.

Additionally, a class employing the finite volume technique has been included for the discretization of external dimensions. The finite volume technique relies on a grid with equidistant cells. Advection terms are discretized using the MUSCL technique [25], which involves linear reconstruction of profiles and the use of a slope limiter to ensure Total Variation Diminishing (TVD) property. This is crucial for handling sharp shock waves that may form due to strong advection terms. Central differences are employed for diffusive fluxes, resulting in an overall scheme that offers second-order accuracy.

Single and multiphase fluid classes

The primary function of the single fluid class is to generate hydrocarbon and aqueous fluids and establish the necessary properties for them, namely viscosity and density. Various options for configuring the physical properties are considered as follows:

- setting value directly,
- interpolation based on user specified data,
- the potential to integrate with external libraries in the future (e.g., NEXSIM developed by Equinor, HYSYS, and UNISIM).

Multi-phase fluids can subsequently be created by combining aqueous and hydrocarbon fluid objects, along with additional properties like inversion point, interfacial tension, and Hamaker constant. With the volume fraction available, this new multiphase fluid object enables the calculation of essential properties such as emulsion viscosity and density, as well as the determination of the dispersed and continuous phases through the class functionality. Furthermore, this class incorporates essential attributes as placeholders, enabling the specification of other required properties such as interfacial tension and the Hamaker constant based on the determined dispersed/continuous phases. The depicted process is also illustrated in Figure 2-5.

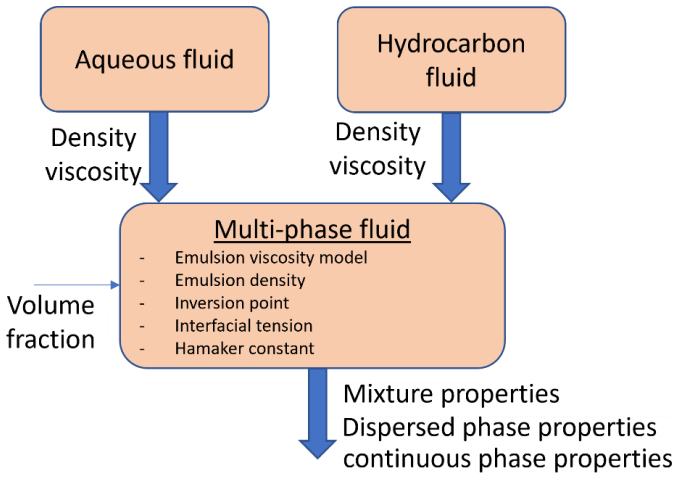

Figure 2-5: Schematic of the multiphase class.

2.3.2. Solver classes

Solvers for various modules (0D, 1D, 2D PBMs) are programmed, with each solver inheriting from the previous one. This approach minimizes the amount of code, which is crucial for maintaining the library.

Solver classes discretize the governing equations into a set of ODEs, pre-calculate coefficient vectors and matrices, and ultimately solve the problem using an external ODE solver library. Two external libraries have been integrated for this purpose, including "odeint" from the "Boost C++ library" and "sundials." This offers users several options for solvers.

Considerable attention has been given to the computational efficiency of the program. The primary programming strategies for optimizing the computational code and reducing computational time are as follows:

- Utilizing a robust coarse grid for the internal domain, established through the spectral-element orthogonal collocation technique. The grid is configured based on prior information regarding the inlet, initial, and estimated equilibrium distributions.
- Setting up the ODE systems in alignment with the underlying physics, employing C++ overloading and template programming capabilities. This approach considers

the presence of different phenomena (e.g., breakage and coalescence), and utilizes the pertinent ODE set function according to that. In this manner, computations that are not needed will be avoided.

- Prior to executing the ODE time integrator, performing pre-calculation and storing all feasible matrices and vectors. This approach enables efficient reuse during computations, thereby reducing floating-point operations.
- Implementing an optimized algorithm for MPCHIP interpolation, a crucial component of the program. Instead of relying on the off-the-shelf libraries, which can introduce computational overhead, we have efficiently programmed this algorithm. Furthermore, we have split the interpolation process into distinct steps, such as calculating the cubic polynomial coefficients and determining the interpolated function at specified points, each in separate functions. This approach allows us to customize the use of these functions to meet our specific computational requirements and perform the computation more efficiently.

2.3.3. Post processing classes

The post-processing classes make use of the distribution class functionality to compute distribution moment properties, such as volume fraction, average droplet size, and standard deviation from the simulation results, based on user preferences. Moreover, if the model incorporates spatial dimensions, these classes facilitate the calculation of spatial averages, integrals, as well as surface fluxes, numerical imbalances and separation efficiency.

2.3.4. Utility classes

Two classes are envisaged as below:

“Logger class” captures events from different stages of a simulation in forms of “Event Flag”, ”Error”, ”Warning” and ”Info” strings.

“Report class” has three main functions:

- Generates text file for the simulation report based on the logger class attributes.
- Generates comma-separated value (CSV) files for the numerical results.

2.4. References

[1] R. Gunawan, I. Fusman, R.D. Braatz, High Resolution Algorithms for Multidimensional Population Balance Equations, AIChE J. 50 (2004) 2738–2749. https://doi.org/10.1002/aic.10228.

[2] S. Rigopoulos, A.G. Jones, Finite-element scheme for solution of the dynamic population balance equation, AIChE J. 49 (2003) 1127–1139. https://doi.org/10.1002/aic.690490507.

[3] Z. Zhu, C.A. Dorao, H.A. Jakobsen, A least-squares method with direct minimization for the solution of the breakage-coalescence population balance equation, Math. Comput. Simul. 79 (2008) 716–727. https://doi.org/10.1016/j.matcom.2008.05.001.

[4] S. Rigopoulos, Population balance modelling of polydispersed particles in reactive flows, Prog. Energy Combust. Sci. 36 (2010) 412–443. https://doi.org/10.1016/j.pecs.2009.12.001.

[5] D. Li, Z. Li, Z. Gao, Quadrature-based moment methods for the population balance equation: An algorithm review, Chinese J. Chem. Eng. 27 (2019) 483–500. https://doi.org/10.1016/j.cjche.2018.11.028.

[6] L. Müller, A. Klar, F. Schneider, A numerical comparison of the method of moments for the population balance equation, Math. Comput. Simul. 165 (2019) 26–55. https://doi.org/10.1016/j.matcom.2019.02.020.

[7] G. Bhutani, P.R. Brito-Parada, J.J. Cilliers, Polydispersed flow modelling using population balances in an adaptive mesh finite element framework, Comput. Chem. Eng. 87 (2016) 208–225. https://doi.org/10.1016/j.compchemeng.2016.01.011.

[8] D. Ramkrishna, Population balances : theory and applications to particulate systems in engineering, Academic Press, 2000. https://doi.org/https://doi.org/10.1016/B978-0-12-576970-9.X5000-0.

[9] S. Kumar, D. Ramkrishna, On the solution of population balance equations by discretization - I. A fixed pivot technique, Chem. Eng. Sci. 51 (1996) 1311–1332. https://doi.org/10.1016/0009-2509(96)88489-2.

[10] S. Kumar, D. Ramkrishna, On the solution of population balance equations by discretization - II. A moving pivot technique, Chem. Eng. Sci. 51 (1996) 1333–

1342. https://doi.org/10.1016/0009-2509(95)00355-X.

[11] J. Kumar, M. Peglow, G. Warnecke, S. Heinrich, L. Mörl, Improved accuracy and convergence of discretized population balance for aggregation: The cell average technique, Chem. Eng. Sci. 61 (2006) 3327–3342. https://doi.org/10.1016/j.ces.2005.12.014.

[12] F. Filbet, P. Laurençot, Numerical Simulation of the Smoluchowski Coagulation Equation, SIAM J. Sci. Comput. 25 (2004) 2004–2028. https://doi.org/10.1137/S1064827503429132.

[13] N. V. Mantzaris, P. Daoutidis, F. Srienc, Numerical solution of multi-variable cell population balance models. II. Spectral methods, Comput. Chem. Eng. 25 (2001) 1441–1462. https://doi.org/10.1016/S0098-1354(01)00710-4.

[14] J. Solsvik, H.A. Jakobsen, Effects of Jacobi polynomials on the numerical solution of the pellet equation using the orthogonal collocation, Galerkin, tau and least squares methods, Comput. Chem. Eng. 39 (2012) 1–21. https://doi.org/10.1016/j.compchemeng.2011.11.015.

[15] C.A. Dorao, H.A. Jakobsen, A least squares method for the solution of population balance problems, Comput. Chem. Eng. 30 (2006) 535–547. https://doi.org/10.1016/j.compchemeng.2005.10.012.

[16] J. Solsvik, H.A. Jakobsen, Evaluation of Weighted Residual Methods for the Solution of a Population Balance Model Describing Bubbly Flows: The Least-Squares, Galerkin, Tau, and Orthogonal Collocation Methods, Ind. Eng. Chem. Res. 52 (2013) 52. https://doi.org/10.1021/ie402033b.

[17] F. Gelbard, J.H. Seinfeld, Numerical solution of the dynamic equation for particulate systems, J. Comput. Phys. 28 (1978) 357–375. https://doi.org/10.1016/0021-9991(78)90058-X.

[18] M. Nicmanis, M.J. Hounslow, A finite element analysis of the steady state population balance equation for particulate systems : Aggregation and growth, Comput. Chem. Eng. 20 (1996) S261–S266. https://doi.org/10.1016/0098-1354(96)00054-3.

[19] M. Nicmanis, M.J. Hounslow, Finite-element methods for steady-state population balance equations, AIChE J. 44 (1998) 2258–2272. https://doi.org/10.1002/aic.690441015.

[20] L.I. Costa, G. Storti, S. Lazzari, Solution of population balance equations by logarithmic shape preserving interpolation on finite elements, Comput. Chem. Eng. 119 (2018) 13–24. https://doi.org/10.1016/j.compchemeng.2018.08.008.

[21] N. V. Mantzaris, P. Daoutidis, F. Srienc, Numerical solution of multi-variable cell population balance models. III. Finite element methods, Comput. Chem. Eng. 25 (2001) 1463–1481. https://doi.org/10.1016/S0098-1354(01)00711-6.

[22] A.W. Mahoney, D. Ramkrishna, Efficient solution of population balance equations with discontinuities by finite elements, Chem. Eng. Sci. 57 (2002) 1107–1119. https://doi.org/10.1016/S0009-2509(01)00427-4.

[23] Z. Zhu, C.A. Dorao, D. Lucas, H.A. Jakobsen, On the Coupled Solution of a Combined Population Balance Model Using the Least-Squares Spectral Element Method, Ind. Eng. Chem. Res. 48 (2009) 7994–8006. https://doi.org/10.1021/ie900088q.

[24] J. Villadsen, M.L. Michelsen, Solution of differential equation models by polynomial approximation, Prentice-Hall, Englewood Cliffs, New York, 1978.

[25] V.S. Dale Anderson, John C. Tannehill, Richard H. Pletcher, Ramakanth Munipalli, Computational Fluid Mechanics and Heat Transfer, CRC Press, 2020.

Chapter 3

3. Spatially homogeneous PBM (paper I)

This chapter includes the paper-I published in "Chemical Engineering Research and Design". In this work, we have addressed a key challenge in numerical solution of population balance equations (PBE), namely, the uncertainty pertaining to the truncation of the droplet size domain. This choice of truncation point can significantly impact both the accuracy of the solution and the stiffness of the subsequent system of equations. To tackle this issue, we propose a novel approach that involves utilizing a closed-form analytical solution of the PBE in the form of a dimensionless group. We have successfully applied this approach to estimate the time and length scales of the system through an iterative algorithm. These findings are crucial for numerical grid generation based on spectral-element orthogonal collocation technique, which holds promise for conducting robust, efficient, and accurate transient and steady-state computations.

Paper I- Moein Assar, Brian Arthur Grimes, A new approach to analyze the equilibrium and transient behaviors of particulate systems and the subsequent application to multiphase fluid systems, Chemical engineering research and design, 188 (2022) 1083-1096.

Available online at www.sciencedirect.com

Chemical Engineering Research and Design

journal homepage: www.elsevier.com/locate/cherd

A new approach to analyze the equilibrium and transient behaviors of particulate systems and the subsequent application to multiphase fluid systems

*Moein Assar, Brian Arthur Grimes**

Ugelstad Laboratory, Department of Chemical Engineering, Norwegian University of Science and Technology (NTNU), N-7491 Trondheim, Norway

ARTICLE INFO

Article history:
Received 9 June 2022
Received in revised form 25 October 2022
Accepted 26 October 2022
Available online 29 October 2022

Keywords:
Population balance equation
Multiphase fluid
Particulate system
Orthogonal Collocation
Approximation technique

ABSTRACT

Fast and robust computation for population balance models is a crucial requirement for simulating particulate systems. Despite all the recent advances in developing relevant computational algorithms, either efficiency or robustness can only be achieved at the expense of the other. However, optimal compromise is possible by having prior estimates of the system's internal length and time scales. Thus, an approximation technique is introduced in this study to extract equilibrium and transient behaviors for a particulate system considering coalescence and breakage phenomena. The approximation method is developed by simplifying assumptions on the available analytical solution for a spatially homogeneous population balance equation with simple kernels. The derived equilibrium and transient equations suggest that the system is governed by a dimensionless group that can describe the equilibrium distribution of the system as well as the rate and the direction that the system is likely to evolve. The method is applied to two different sets of complex breakage and coalescence kernels used for liquid-liquid dispersed systems. The approximated time and length scales were validated with numerical results; thus, the approximation can be used to generate targeted element-based orthogonal collocation grids for fast and robust computation of transient and steady-state particulate systems. This approach can significantly decrease the computation time, typically by 40–70 % for steady-state conditions.

1. Introduction

Population balance modeling has been widely used throughout past decades as the main backbone to describe particulate systems via evolution of the particle size distribution as well as functions of system operating conditions and physicochemical properties (Ramkrishna, 2000). Such models are used frequently in different areas such as crystallization, microbial cell growth, granulation, polymerization, and multiphase fluid systems to support process design, optimization, and control (Falola et al., 2013; Qamar, 2014). Notably, the population balance equation (PBE) is the primary tool to simulate separation and transport processes involving multiphase fluids by applying fundamental knowledge regarding coalescence and breakage phenomena. Such simulations aim to predict the evolution of droplet size distribution (DSD) formed by breakage and coalescence phenomena that might significantly impact equipment performance.

* Corresponding author.
E-mail address: brian.a.grimes@ntnu.no (B.A. Grimes).

https://doi.org/10.1016/j.cherd.2022.10.044

Nomenclature

c	Constant coalescence rate in analytical solution (m^3s^{-1}).
c_{est}	Estimated constant coalescence rate (m^3s^{-1}).
C_1, C_2	Tuning parameters used in approximation of transient time.
$f_{n,r}$	Radius-based number density function (m^{-4}).
$f_{n,v}$	Volume-based number density function (m^{-6}).
$f_{v,r}$	Radius-based volume density function (m^{-1}).
$\hat{f}_{v,r}$	Dimensionless radius-based volume density function ($f_v r_m$).
g	Breakage frequency (s^{-1}).
k	Coalescence rate (m^3s^{-1}).
k_{c1}, k_{c2}	Tuning parameters used in coalescence model.
k_{b1}, k_{b2}	Tuning parameters used in breakage model.
k_1	Time-dependent coefficients used in the analytical solution (m^{-6}).
k_2	Time-dependent coefficients used in the analytical solution (m^{-3}).
$\hat{k}_1$, $\hat{k}_2$	Dimensionless time-dependent coefficients used in the analytical solution.
m_0	0th order moment equal to number of droplets per unit volume (m^{-3}).
m_3	3rd order moment.
M	Dimensionless group number.
N	Number of droplets per unit volume (m^{-3}).
$\hat{n}$	Dimensionless time-dependent coefficient used in the analytical solution.
r	Droplet radius (m).
$\hat{r}$	Dimensionless droplet radius (r/r_m).
r_m	Upper bound of droplet radius internal domain (m).
s	Parameter used in breakage frequency kernel ($m^{-3}s^{-1}$).
s_{est}	Estimated parameter used in breakage frequency kernel ($m^{-3}s^{-1}$).
t	Time (s).
$\hat{t}$	Dimensionless time (t/t_c).
t_c	Characteristic time (s).
v	Droplet volume (m^3).
v_m	Upper bound of droplet volume internal domain (m^3).
β_r	Radius-based daughter distribution (m^{-1}).
β_v	For volume-based daughter distribution (m^{-3}).
Γ	Gamma function.
Γ^{-1}	Inverse gamma function.
δ	Dirac delta function.
μ_r	Average droplet radius (m).
$\hat{\mu}_r$	Dimensionless average droplet radius.
σ_r	Droplet radius standard deviation (m).
$\hat{\sigma}_r$	Dimensionless droplet radius standard deviation.
ϕ	Volume fraction.
ε	Turbulent energy dissipation rate (m^2s^{-3}).
τ	Dispersed phase surface tension (Nm^{-1}).
ρ_c	Continuous phase density (kgm^{-3}).
ρ_d	Dispersed phase density (kgm^{-3}).
ψ_E	Collision efficiency used in coalescence rate model.
ω	Coalescence efficiency used in coalescence rate model (m^3s^{-1}).

One powerful class of methods for solving PBE is the weighted residue methods (MWR). They have the so-called infinite order of accuracy comparing to other methods such as class methods, finite volume method, and finite element method (FEM) (Mantzaris et al., 2001a), as well as better convergence behavior (Solsvik and Jakobsen, 2012). These properties can increase the computational efficiency as normally coarser grids can adequately provide the same accuracy compared with other methods (Dorao and Jakobsen, 2006). Here, the dependent variable (i.e. DSD) is approximated with a truncated series of so-called trial function over the entire computational domain subject to minimization of the product of the governing equation with the test function (Mantzaris et al., 2001a). Several spectral methods have been proposed based on the choice of trial and test functions, namely Galerkin, Tau, collocation, and least square. In collocation methods, the test function is a Dirac delta function, assuring exact satisfaction of equation at the collocation points (Mantzaris et al., 2001a). Moreover, the collocation method provides the simplest and most computationally efficient scheme with accuracy and stability similar to the Galerkin method (Mantzaris et al., 2001a; Solsvik and Jakobsen, 2013). To add more flexibility to these methods, several researchers have also used MWR in an element-based framework (Costa et al., 2018; Gelbard and Seinfeld, 1978; Mahoney and Ramkrishna, 2002; Mantzaris et al., 2001b; Nicmanis and Hounslow, 1998, 1996; Rigopoulos and Jones, 2003; Zhu et al., 2009).

The current study is part of a bigger effort in which a modular C++ model library (PBmulib) is being developed based on a population balance modeling approach for separation and transport of multiphase fluids in the form of crude oil and water emulsions. According to the level of complexity in the systems as well as the physics involved, these models are developed for 0, 1, and 2 spatial dimensions. These three modules can cover wide applications ranging from multiphase pipe flow to batch settlers/skimmers and 3-phase separators. The structure of the library facilitates a modular design and development for building more complex processes fast. Additionally, leveraging a C++ core ensures fast computation speeds on modern platforms. The library will allow the PBE models to be readily incorporated into common general-purpose or specialized simulation software environments such as MATLAB, Python, and HYSYS.

The main challenge for developing such a library is the ability to perform fast and robust computations to solve equilibrium and transient population balance models. This is compromised by the inherent numerical challenges associated with the PBE. A good description of such challenges is presented by Rigopoulos and Jones (2003); Zhu et al. (2008), which can be summarized as follows:

- Proper choice for truncation of the PBE internal domain.
- Internal consistency of the numerical schemes.
- Efficient computation of equilibrium distributions.

- Strong non-linear behavior introduced by the coalescence terms resulting in a complex convergence behavior.

Mathematically, the internal coordinate of the PBE expands to infinity. Thereby, for numerical computation, the upper bound of the internal coordinate should be truncated by a finite value. Choice of truncation point can drastically affect the accuracy of the solution as well as the stiffness of the equations. If underestimated, solution methods would fail to produce correct results. Whereas, in the case of overestimation, it would lead to poor results as wider domain ranges demand finer grids. Additionally, a stiffer system of ODEs would be expected, which consequently results in low computational efficiency. This takes place as tiny values in the tail region can attain large particle volumes, making the numerical convergence computationally costly (Nicmanis and Hounslow, 1998). Furthermore, in cases where the system of interest is in equilibrium, the equilibrium distribution is often obtained indirectly by allowing the transient system to evolve over time until it reaches equilibrium. This is usually the case when the equations are highly non-linear and a steady-state solution cannot be obtained directly (Rigopoulos and Jones, 2003). For such problems, having a rough estimation for system transient time can be extremely valuable since many of the available numerical schemes can suffer from accumulated error and lack of internal consistency in excessive numerical time integration.

Reviewing the available literature, the solutions for this challenge can be categorized into two main approaches (Rigopoulos and Jones, 2003):

- Adopting a fixed grid technique, monitoring the solution, and changing the domain bound if required.
- Applying an adaptive or moving grid by remeshing algorithms.

The conventional fixed grid techniques require firm reliance on the user post interpretation of the results and re-selection of the domain bound in case of unphysical results. Attarakih et al. (2004) developed a technique to estimate the total finite domain error. In their approach, the error is checked at each integration step; once the tolerance is violated, the calculations are stopped and restarted again with improved estimation of lower and upper bounds of the domain. However, in this method, the grid is preliminarily generated according to the initial and/or inlet distributions, and for cases with the equilibrium distribution located away from those known distributions, it requires multiple trial and error iteration to modify the grid. Such an approach can be computationally expensive.

The other alternative is to track the changes in the distribution function via a moving grid technique. Several techniques with such a strategy have been proposed by different researchers (Attarakih et al., 2002; Briesen, 2009; Duarte and Baptista, 2007; Lee et al., 2001; Sewerin and Rigopoulos, 2017). However, despite the robustness these techniques offer, the extra computational overhead can be high compared to their counterpart fixed grid techniques due to the required interpolation step involved.

From this brief overview, preliminary information about the equilibrium and transient behavior of the problem can be valuable. A preliminary estimation of the equilibrium distribution, together with the initial/inlet distribution information, can be used to make the fixed grid techniques more robust. On the other hand, the estimated time scale of the system can be used to set proper simulation time, which is vital for robust computation and model parameter estimation particularly for steady-state PBE.

In this study, to address these issues, a new approximation technique is proposed to estimate the steady and transient behaviors in the forms of time and length scales for a spatially homogeneous particulate system considering breakage and coalescence. Subsequently, these scales are utilized to form an element-based orthogonal collocation scheme to discretize and solve both transient and steady-state PBE.

2. Mathematical analysis of spatially homogeneous PBE

2.1. Radius-based truncated PBE for dimensionless volume density function

In this study, we consider the population balance equation for a spatially homogeneous particulate system without inflow/outflow. For more ease of derivation, we use the PBE for a radius-based volume density distribution in dimensionless form. This will make working with DSD more convenient. To be able to analyze the problem numerically, the internal domain is truncated to a maximum droplet radius (r_m) which yields the following equation (for detailed derivation the interested reader is referred to the Supplementary material):

$$\frac{\partial \hat{f}_{v,r}(\hat{r},\hat{t})}{\partial \hat{t}} = (t_c r_m)\int_{\hat{r}}^{1} 2g(\hat{r}')\beta_r(\hat{r}',\hat{r})\hat{f}_{v,r}(\hat{r}',\hat{t})\frac{\hat{r}^3}{\hat{r}'^3}d\hat{r}' - t_c g(\hat{r})\hat{f}_{v,r}(\hat{r},\hat{t}) + \left(\frac{t_c}{v_m}\right)\int_0^{\hat{r}/\sqrt[3]{2}} k(\hat{r}',\hat{r}'')\hat{f}_{v,r}(\hat{r}',\hat{t})\hat{f}_v(\hat{r}'',\hat{t})\frac{\hat{r}^5}{\hat{r}'^3\hat{r}''^5}d\hat{r}' - \left(\frac{t_c}{v_m}\right)\hat{f}_{v,r}(\hat{r},\hat{t})\int_0^1 k(\hat{r}',\hat{r})\hat{f}_{v,r}(\hat{r}',\hat{t})\frac{1}{\hat{r}'^3}d\hat{r}' \quad (1)$$

where the terms on the right-hand side of the equation from left to right are breakage birth, breakage death, coalescence birth, coalescence death. $\hat{r}$ is dispersed phase dimensionless droplet radius (r/r_m), $\hat{t}$ is dimensionless time (t/t_c), $\hat{f}_{v,r}(\hat{r},\hat{t})$ is the dimensionless radius-based volume density for droplet radius $\hat{r}$ at time $\hat{t}$, $g(\hat{r})$ is the breakage frequency for droplet radius $\hat{r}$, $\beta_r(\hat{r}',\hat{r})$ is the radius-based daughter distribution of droplet radius $\hat{r}$ resultant from breakage of droplet size $\hat{r}'$, and $k(\hat{r}',\hat{r}'')$ is the rate of coalescence between droplet sizes of $\hat{r}'$ and $\hat{r}'' = (\hat{r}^3 - \hat{r}'^3)^{1/3}$. t_c is the selected characteristic time scale for the system. v_m is the equivalent droplet volume for droplet size equal to r_m. The factor 2 in the breakage birth term appeared as only binary breakage of droplets are considered in this study.

By truncating the domain, the main uncertainty regarding the numerical solution of the PBE appears in the problem. It must be noticed that at this stage, the proper numerical value of r_m is still unknown. Now, in the mentioned PBE framework, the distribution features can be conveniently computed by:

$$N(\hat{t}) = \frac{1}{v_m}\int_0^1 \frac{\hat{f}_{v,r}(\hat{r},\hat{t})}{\hat{r}^3}d\hat{r} \quad (2)$$

$$\phi(\hat{t}) = \int_0^1 \hat{f}_{v,r}(\hat{r},\hat{t})d\hat{r} \quad (3)$$

$$\hat{\mu}_r(\hat{t}) = \frac{\mu_r(\hat{t})}{r_m} = \frac{1}{\phi(\hat{t})}\int_0^1 \hat{f}_{v,r}(\hat{r},\hat{t}).\,\hat{r}.\,d\hat{r} \quad (4)$$

$$\hat{\sigma}_r(\hat{t}) = \frac{\sigma_r(\hat{t})}{r_m} = \left(\frac{1}{\phi(\hat{t})}\int_0^1 (\hat{r}-\hat{\mu}_r)^2 \hat{f}_{v,r}(\hat{r},\hat{t})d\hat{r}\right)^{0.5} \quad (5)$$

where N, ϕ, $\hat{\mu}_r$ and $\hat{\sigma}_r$ are the total number of droplets per unit volume, volume fraction, dimensionless average droplet radius, and dimensionless droplet radius standard deviation, respectively.

2.2. A simple kernel with an analytical solution

An analytical solution to PBE subject to simple kernels ($g(r) = sr^3$, $k(r', r) = c$, $\beta_r(r', r) = 3r^2/r'^3$ where s and c are constants) has been proposed by Benjamin and Madras (2003). They solved transient PBE for the mentioned system subject to an initial DSD given by an exponential form. The dimensional analysis of PBE for this system shows that equilibrium distribution can be characterized merely by one dimensionless group (details in the Supplementary material). The analytical solution in the form of dimensionless radius-based volume density, takes the following form (derivation in the Supplementary material).

$$\hat{f}_{v,r}(\hat{r}, t) = \hat{k}_1(t)\hat{r}^5 \exp(-\hat{k}_2(t)\hat{r}^3) \quad (6)$$

where $\hat{k}_1$ and $\hat{k}_2$ are as follows:

$$\hat{k}_1(t) = 4\pi\hat{n}(t)^2 \frac{m_0(0)^2}{m_3} {r_m}^6 \quad (7)$$

$$\hat{k}_2(t) = \hat{n}(t)\frac{m_0(0)}{m_3} {r_m}^3 \quad (8)$$

where $m_0(0)$ is 0th order moment and equivalent to the total number of droplets at initial condition. m_3 is the 3rd order moment and related to the volume fraction of the dispersed phase by $3\phi/(4\pi)$. $\hat{n}(t)$ is also defined as:

$$\hat{n}(t) = \hat{n}(\infty)\left[\frac{1+\hat{n}(\infty)\tanh\left(\hat{n}(\infty)\frac{m_0(0)ct}{2}\right)}{\hat{n}(\infty)+\tanh\left(\hat{n}(\infty)\frac{m_0(0)ct}{2}\right)}\right] \quad (9)$$

$$\hat{n}(\infty) = \left(\frac{2sm_3}{c}\right)^{\frac{1}{2}}\left(\frac{1}{m_0(0)}\right) \quad (10)$$

By setting time in Eqs. 7 and 8 to infinity, equilibrium distribution yields using $\hat{k}_1$ and $\hat{k}_2$ as follows:

$$\hat{k}_1(\infty) = 8\pi\left(\frac{s}{c}{r_m}^6\right) \quad (11)$$

$$\hat{k}_2(\infty) = \left(\frac{8\pi}{3}\right)^{1/2}\left(\frac{1}{\phi}\frac{s}{c}{r_m}^6\right)^{\frac{1}{2}} \quad (12)$$

Eq. 6 describes the dimensionless volume density distribution at a specific time. However, the focus of this study is to propose some simple relations that can approximate the equilibrium and transient behavior of any given kernels. To do that, it is necessary to derive some key features for the distributions. Such features are average droplet radius, standard deviation, peak droplet radius as well as head and tail of the distributions. The mentioned features are presented in the Supplementary material for transient distributions.

2.3. Steady-state analysis of general kernels

As mentioned in the previous section, the whole equilibrium distribution for the simple set of kernels can be characterized by only one dimensionless group of parameters. The mentioned property can also be seen in the main volume-density distribution features at equilibrium condition as follows:

$$\hat{\mu}_r = \frac{4}{9}\left(\frac{3}{8\pi}\right)^{\frac{1}{6}}\Gamma^{-1}(1/3, 0)M \cong 0.8355M \quad (13)$$

$$\hat{\sigma}_r = \frac{1}{9}\left(\frac{3}{8\pi}\right)^{\frac{1}{6}}\left(90\Gamma^{-1}\left(\frac{2}{3}, 0\right) - 16\Gamma^{-1}\left(\frac{1}{3}, 0\right)^2\right)^{0.5} M \cong 0.2069M \quad (14)$$

$$\hat{r}_{peak} = \left(\frac{25}{24\pi}\right)^{\frac{1}{6}} M \cong 0.8319M \quad (15)$$

where the dimensionless term M is defined as below:

$$M = \left(\frac{\phi}{\frac{s}{c}{r_m}^6}\right)^{\frac{1}{6}} \quad (16)$$

Accordingly, the significant property of these simple kernels is that all the key features of the equilibrium distribution have a linear relation to the dimensionless number M. Eqs. 13–15 provides the exact values for the equilibrium behavior of the simple kernels. However, it is generally possible to extend this approach to approximate these behaviors for any other kernels of interest. Such a task requires the extraction of some values from the kernel function as representative values for c and s for the equilibrium distribution. In the system with the analytical solution, the values of c and s are constants while generally they can have functionality of the droplet size. For that, we propose averaging these values weighted by the equilibrium volume density distribution over the internal domain as follows:

$$s_{est}(\infty) = \frac{1}{\phi}\int_0^\infty \hat{f}_{v,r}(\hat{r}, \infty)\frac{g(r)}{r^3}d\hat{r} \quad (17)$$

$$c_{est}(\infty) = \frac{1}{\phi^2}\int_0^\infty\int_0^\infty \hat{f}_{v,r}(\hat{r}', \infty)\hat{f}_{v,r}(\hat{r}, \infty)k(r', r)d\hat{r}'d\hat{r} \quad (18)$$

The above terms are computationally expensive as the single, and especially double integrals are expensive to compute numerically; additionally, they contain the equilibrium distribution ($\hat{f}_{v,r}(\hat{r}', \infty)$) that is still unknown at this point, which we aim to estimate. To make the math more manageable and to avoid the difficulties of evaluating of the integral, we assume the whole distribution is concentrated at the average droplet radius. Mathematically, this can be handled using the Dirac delta function at the average points as $\hat{f}_{v,r}(\hat{r}, \infty) = \phi\delta(\hat{r} - \hat{\mu}_r(\infty))$. It is worth mentioning that other forms of functions for $\hat{f}_{v,r}(\hat{r}, \infty)$ can still be assumed (e.g. exponential and log-normal); however, such an assumption would need directly solving the above integrals. In any case, the first thing to do is to start from $\hat{\mu}_r(\infty)$ as an initial guess and solve iteratively.

The mentioned Dirac delta function assumption significantly simplifies the Eqs. 17 and 18 to the following ones:

$$s_{est}(\infty) = \frac{g(\mu_r(\infty))}{\mu_r(\infty)^3} \quad (19)$$

$$c_{est}(\infty) = k(\mu_r(\infty), \mu_r(\infty)) \quad (20)$$

Now, the approximated representative values have only the dependency of the average droplet radius of equilibrium distribution. At the same time, according to Eq. 13, the average droplet radius of equilibrium distribution has the

dependency of dimensionless value M, which can be calculated by knowing the representative values $s_{est}(\infty)$, $c_{est}(\infty)$. In other words, Eqs. 13, 19, and 20 forms a nonlinear system of equations which can be solved by any numerical technique to yield the values for $s_{est}(\infty)$, $c_{est}(\infty)$, and $\hat{\mu}_r(\infty)$. For that purpose, an illustrating iterative approach is proposed and demonstrated in the Supplementary material section.

By knowing the numerical values for $s_{est}(\infty)$, $c_{est}(\infty)$, it is now possible to approximate the equilibrium distribution using Eq. 6. Consequently, the internal domain bound can be simply specified by calculating the head and tail of the equilibrium distribution. One possible way to define head and tail is by obtaining the droplet radius sizes at which the smaller droplet sizes yield a specific value of volume fraction (typically 1 % and 99 % for the tail and head, respectively). This can mathematically be defined as follows:

$$\phi_x = x\phi = \int_0^{\hat{r}_x} \hat{f}_{v,r}(\hat{r}, \infty)d\hat{r} \tag{21}$$

where ϕ_x is the volume fraction of interest and can have a value between 0 and ϕ and the typical values would be 0.01ϕ and 0.99ϕ for tail and head of the distribution, respectively. By using this definition (Eq. 21) and substituting $\hat{f}_{v,r}$ using Eq. 6, the following equation is obtained.

$$\phi_x = x\phi = \quad \phi - \frac{k_1(\infty)exp(-k_2(\infty)\hat{r}_x^3)(k_2(\infty)\hat{r}_x^3 + 1)}{3k_2(\infty)^2} \tag{22}$$

Rearranging Eq. 22, forms the final equation to calculate the head and tail of the equilibrium distribution as follows:

$$\left(\left(\frac{8\pi}{3}\right)^{\frac{1}{2}}\left(\frac{\hat{r}_x}{M}\right)^3 + 1\right)\exp\left(-\left(\frac{8\pi}{3}\right)^{\frac{1}{2}}\left(\frac{\hat{r}_x}{M}\right)^3\right) - (1 - x) = 0 \tag{23}$$

Eq. 23 is a nonlinear equation and can be solved numerically for $\hat{r}_x$ for a target value of x. Consequently, for steady-state PBE, the truncation point for the internal domain can be specified as head plus a safety margin. For transient PBE, this value should be selected considering the initial distribution and approximated equilibrium distribution simultaneously. This issue is explained with more details in Section 3.

2.4. Transient analysis of general kernels

The characteristic time scale for a transient system can be defined as the transient time required for the system to evolve from the initial condition to a particular state closer to the equilibrium state. For our specific case, we approximate this value according to the transient behavior of the average droplet radius. That is, the time required for the average droplet radius to move a fraction of the distance between initial and equilibrium average radii. This can mathematically be expressed by:

$$\hat{\mu}_r(t_x) = x[\hat{\mu}_r(\infty) - \hat{\mu}_r(0)] + \hat{\mu}_r(0) \tag{24}$$

The value of x in Eq. 24 can be selected between 0 and 1. In this study, we consider x as 0.9. This choice was based on our observation (the cases that we studied in this work) that $3 \times t_{0.9}$ can practically be considered as the required time to reach the equilibrium state. However, it might not be appropriate for other kernels, and the proper choice of these values (x and the factor of the time scale) can be evaluated and possibly slightly modified for a specific system under study to achieve an equilibrium state.

For the simple kernels, Eq. 24 can be solved for t_x to yield exact values of transient time; nonetheless, this equation cannot be directly extended to other kernels as the representative values $s_{est}(t)$, $c_{est}(t)$ are not generally constant, and their time functionalities needs to be considered. To overcome this, we propose an approximation of the transient time by integrating the rate of change in the average droplet radius. Mathematically, the problem can be outlined as:

$$t_x = \int_{\hat{\mu}_r(0)}^{\hat{\mu}_r(t_x)} \frac{1}{\frac{d\hat{\mu}_r}{dt}(\hat{\mu}_r)}d\hat{\mu}_r \tag{25}$$

The term $d\hat{\mu}_r/dt(\hat{\mu}_r)$ is the rate of change in the average droplet radius of dimensionless volume density distribution at any given $\hat{\mu}_r$ and has the dimension equal to the inverse of time. A useful property of the analytical solution for the simple kernels is that initial form of the distribution (Eq. 6) is always preserved. Taking advantage of it, we can calculate $d\hat{\mu}_r/dt(\hat{\mu}_r)$ by just setting time to zero provided that we modify the value for the total number of droplets per unit volume, m_0 according to the pertinent $\hat{\mu}_r$. Based on the derived equation for the transient average radius in the appendix section, this term can be mathematically obtained for the simple kernels as follows:

$$\frac{d\hat{\mu}_r}{dt}(\hat{\mu}_r) = -\frac{0.7386}{3}\frac{\phi^{\frac{1}{3}}}{r_m\hat{n}(0)^{\frac{4}{3}}m_0^{\frac{1}{3}}}\frac{d\hat{n}(0)}{dt} \tag{26}$$

where $\hat{n}(0)$ is simply equal to one and $d\hat{n}/dt(0)$ can be calculated as:

$$\frac{d\hat{n}(0)}{dt} = \frac{m_0 c}{2}(\hat{n}^2(\infty) - 1) \tag{27}$$

By substitution, Eq. 26 takes the following form:

$$\frac{d\hat{\mu}_r}{dt}(\hat{\mu}_r) = -\frac{0.7386}{3}\frac{\phi^{\frac{1}{3}}}{r_m}\frac{m_0^{\frac{2}{3}}c}{2}\left(\frac{3}{2\pi}\frac{s\phi}{cm_0^2} - 1\right) \tag{28}$$

As also mentioned, m_0 in Eq. 28 should be corrected by taking the change in the initial number of droplets into account as the distribution evolves. This value can be calculated by Eq. 2. as follows:

$$m_0 = \frac{1}{v_m}\int_0^1 \frac{\hat{f}_{v,r}(\hat{r}, t)}{\hat{r}^3}d\hat{r} \tag{29}$$

Similarly, to simplify the equation and rectify the need to calculate the integral numerically, the whole distribution is assumed to be concentrated at the average radius, $\hat{f}_{v,r}(\hat{r}, t) = \phi\delta(\hat{r} - \hat{\mu}_r)$. By that simplification, number of droplets per unit volume at every $\hat{\mu}_r$ is given by:

$$m_0 \approx \frac{1}{v_m}\int_0^1 \frac{\phi\delta(\hat{r} - \hat{\mu}_r)}{\hat{r}^3}d\hat{r} = \frac{\phi}{v_m\hat{\mu}_r{}^3} \tag{30}$$

By plugging Eq. 30 in 28, it yields:

$$\frac{d\hat{\mu}_r}{dt}(\hat{\mu}_r) \approx 0.0474\frac{\phi}{r_m{}^3}\frac{c(\hat{\mu}_r)}{\hat{\mu}_r{}^2}\left(1 - 8.3776\frac{r_m{}^6}{\phi}\frac{s(\hat{\mu}_r)\hat{\mu}_r{}^6}{c(\hat{\mu}_r)}\right) \tag{31}$$

Eq. 31 describes the key dependencies for the rate of change in the average droplet radius for a dimensionless volume density distribution. However, due to the simplifying assumptions made, Eq. 31 cannot properly predict the time scales for the simple kernel. To remedy this, we reevaluate the constant numerical values in Eq. 31 as follows.

$$\frac{d\hat{\mu}_r}{dt}(\hat{\mu}_r) \approx C_1 \frac{\phi}{{r_m}^3} \frac{c(\hat{\mu}_r)}{{\hat{\mu}_r}^2} \left(1 - C_2 \frac{{r_m}^6}{\phi} \frac{s(\hat{\mu}_r)\hat{\mu}_r{}^6}{c(\hat{\mu}_r)}\right) \tag{32}$$

We can make use of the fact that $d\hat{\mu}_r/dt(0)$ should be equal to zero at equilibrium distribution, i.e., $\hat{\mu}_r = 0.8355M$. This constraint gives the exact value of C_2 equal to 2.94. Additionally, the numerical value of C_1 is tuned for the simple kernels with the available analytical solution using several test cases by changing different numerical values for ϕ, s, and c. Adjusting C_1 was performed by minimization of the average absolute relative deviation (AARD) of total studied cases using MATLAB unconstrained nonlinear optimization functionality (fminunc). The deviation was the calculated between predicted time scale ($t_{0.9}$) by Eq. 32 and that obtained from numerical computation. The final equation takes the following form.

$$\frac{d\hat{\mu}_r}{dt}(\hat{\mu}_r) \approx 0.067 \frac{\phi}{{r_m}^3} \frac{c(\hat{\mu}_r)}{{\hat{\mu}_r}^2} \left(1 - 2.94 \frac{{r_m}^6}{\phi} \frac{\hat{s}(\hat{\mu}_r)\hat{\mu}_r{}^6}{\hat{c}(\hat{\mu}_r)}\right) \tag{33}$$

Having derived the expression of $d\hat{\mu}_r/dt(\hat{\mu}_r)$ for simple kernel, the next step is to extend it to generalized kernels which can be done by replacing c and s terms with estimated values similar to the previous section as follows:

$$\frac{d\hat{\mu}_r}{dt}(\hat{\mu}_r) \approx 0.067 \frac{\phi}{{r_m}^3} \frac{c_{est}(\hat{\mu}_r)}{{\hat{\mu}_r}^2} \left(1 - 2.94 \frac{{r_m}^6}{\phi} \frac{s_{est}(\hat{\mu}_r)\hat{\mu}_r{}^6}{c_{est}(\hat{\mu}_r)}\right) \tag{34}$$

where s_{est} and c_{est} can be estimated by:

$$s_{est}(\hat{\mu}_r) = \frac{g(\mu_r)}{{\mu_r}^3} \tag{35}$$

$$c_{est}(\hat{\mu}_r) = k(\mu_r, \mu_r) \tag{36}$$

Moreover, Eq. 34 can also be rearranged based of the dimensionless group M as follows:

$$\frac{d\hat{\mu}_r}{dt}(\hat{\mu}_r) \approx 0.067 \frac{\phi}{{r_m}^3} \frac{c_{est}(\hat{\mu}_r)}{{\hat{\mu}_r}^2} \left(1 - 2.94 \frac{\hat{\mu}_r{}^6}{M^6}\right) \tag{37}$$

According to the derived expression, when both the breakage and coalescence are present in the system, the rate of the change in the average radius for a dimensionless volume density is proportional to the volume fraction of dispersed phase, the average value of the coalescence rate at that state, and inversely proportional to the square of distribution average radius. This rate is also influenced by the term $(1 - 2.94\hat{\mu}_r{}^6/M^6)$ which determines how remote the system is from equilibrium state. This term can also predict the direction that the distribution is likely to evolve as:

- When positive (equivalent to $\hat{\mu}_r > 0.8355M$), the distribution evolves toward larger droplet sizes.
- When negative (equivalent to $\hat{\mu}_r < 0.8355M$), the distribution evolves toward smaller droplet sizes.
- When zero (equivalent to $\hat{\mu}_r = 0.8355M$), the system is at equilibrium state.

Furthermore, the following similar dependencies are deducted for the systems with either pure breakage or coalescence as follows:

- For a system with pure coalescence, the rate of the change in the average radius for a dimensionless volume density is only proportional to the volume fraction of dispersed phase, and the average value of the coalescence rate at that state and inversely proportional to the square of distribution average radius.
- For a system with pure breakage, the rate of the change in the average radius for a dimensionless volume density is only proportional to both average breakage frequency at that state and distribution average radius.

Now, having the explicit expression for $d\hat{\mu}_r/dt(\hat{\mu}_r)$, the time scale for the system can be conveniently calculated according to Eq. 25.

3. Numerical analysis of the PBE

The orthogonal collocation method (Villadsen and Michelsen, 1978) is used to discretize the internal domain in an element-based form. The primary strategy for generating the grid is to use the least number of elements while keeping the order of the polynomials high enough to have proper error decaying properties. However, it is still helpful to specify a certain number of elements to make the technique more flexible. Collocation points are selected according to the roots of the Jacobi polynomials, and quadrature weights are calculated accordingly. The monotone piecewise cubic Hermite interpolation technique was used (Fritsch and Carlson, 1980) to map the grid points to collocation points (which is essential to calculate the integrals in the coalescence and breakage birth rates). The orthogonal collocation points (Gauss-Radau and Gauss-Lobatto) are not uniformly distributed over an element but more concentrated closer to the edges. As a result, in the case of applying the full spectral technique, the described interpolation technique would not be accurate enough. Additionally, a full spectral technique cannot numerically capture narrow DSDs. The element-based grid can be advantageous in addressing these issues.

For a steady-state problem, four elements are used and selected according to specific locations of the estimated equilibrium distribution. This issue is graphically demonstrated in Fig. 1. Accordingly, the first element is from zero to the tail of the distribution; the second element from the tail to the average radius of the distribution; the third element is from the average radius to the head of the distribution, and the last element is from the head of the distribution to the truncation point (200% of the head).

For transient PBM, a 5-element grid is generated considering two distributions, namely, initial distribution and estimated equilibrium distribution. The element boundaries are selected as:

- zero
- minimum of tails of both distributions;
- average radius of initial distribution;
- average radius of estimated equilibrium distribution;
- maximum of heads of both distributions;
- truncation point (200 % of the maximum of heads of both distributions)

equilibrium distribution can be either right, left, or overlapping with the initial distribution. Therefore, the locations of the boundary elements need to be specified by sorting these boundary points. Moreover, for severe cases where initial and equilibrium distributions are distant from each other, it is wise to add more than one element between the average radii of the two distributions or alternatively more collocation points for this region. Comparison of the DSD

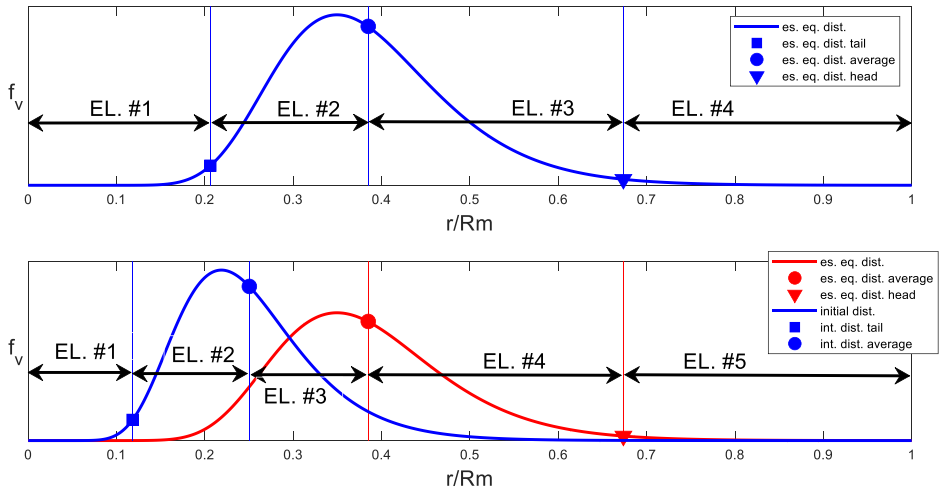

Fig. 1 – Elements used for numerical computation; top: steady-state PBE; bottom: transient PBE.

standard deviation (which gives an idea about the width of the distribution) with this range can also be an excellent criterion for determining the proper number of elements. In this work, for all the studied cases, only one element is used for this region. Overall, four different grid sizes were evaluated with number of collocation points per element equal to 5, 10, 15 and 20 in Section 4.3.

Discretization of the steady-state problem forms a nonlinear set of equations, which were solved iteratively (detail in the Supplementary material). For the transient case, the discretized system of ODEs was integrated using the adaptive Gear's backward differentiation scheme. The iteration and time integration tolerances were both set to 10^{-6}. The simulation time was also set as $3 \times t_{0.9}$ to calculate the equilibrium distribution.

4. Results and discussion

To evaluate the technique, two sets of kernels for liquid-liquid dispersions are used. The kernels are relevant to turbulent systems. The kernel relations together with their parameters are summarized in Table 1.

The breakage and coalescence models show dependencies to system physiochemical properties, namely, phases' densities and interfacial tension as well as hydrodynamic properties like turbulence energy dissipation rates.

Table 1 – Kernels used for case studies.

Kernels #1	coalescence rate	$k(r',r) = \omega(r',r)\psi_E(r',r) \quad \omega(r',r) = k_{c1}\pi 2^{\left(\frac{1}{3}\right)}\varepsilon^{\left(\frac{1}{3}\right)}(r'+r)^2(r'^{(2/3)}+r^{(2/3)})^{\left(\frac{1}{2}\right)} \quad \psi_E(r',r) = \exp\left(-k_{c2}2^{\left(-\frac{1}{6}\right)}\frac{\rho_c^{\left(\frac{1}{2}\right)}\varepsilon^{\left(\frac{1}{3}\right)}}{\tau^{\left(\frac{1}{2}\right)}}\left(\frac{1}{r'}+\frac{1}{r}\right)^{\left(-\frac{5}{6}\right)}\right)$	$k_{c1} = 0.001 \quad k_{c2} = 1$	collision efficiency (Prince and Blanch, 1990), coalescence efficiency (Chesters, 1991)
	breakage frequency	$g(r) = k_{b1}\frac{\varepsilon^{\left(\frac{1}{3}\right)}}{2^{\left(\frac{2}{3}\right)}}\left(\frac{\rho_d}{\rho_c}\right)^{\left(\frac{1}{2}\right)}\frac{1}{r^{\left(\frac{2}{3}\right)}} \quad \exp\left(-k_{b1}\frac{\tau}{2^{\left(\frac{5}{3}\right)}\rho_d\varepsilon^{\left(\frac{2}{3}\right)}}\frac{1}{r^{\left(\frac{5}{3}\right)}}\right)$	$k_{b1} = 1 \quad k_{b1} = 1$	(Vankova et al., 2007)
	daughter distribution	$\beta_r(r',r) = 7.2\frac{r^2}{r'^3}\exp\left(-4.5\frac{(2r^3-r'^3)^2}{r'^6}\right)$		(Coulaloglou and Tavlarides, 1977)
Kernels #2	coalescence rate	$k(r',r) = \omega(r',r)\psi_E(r',r) \quad \omega(r',r) = k_{c1}2^{\left(\frac{7}{3}\right)}\varepsilon^{\left(\frac{1}{3}\right)}(r'+r)^{\left(\frac{7}{3}\right)} \quad \psi_E(r',r) = \exp\left(-k_{c2}2^{\left(-\frac{1}{6}\right)}\frac{\rho_c^{\left(\frac{1}{2}\right)}\varepsilon^{\left(\frac{1}{3}\right)}}{\tau^{\left(\frac{1}{2}\right)}}\left(\frac{1}{r'}+\frac{1}{r}\right)^{\left(-\frac{5}{6}\right)}\right)$	$k_{c1} = 0.1 \quad k_{c2} = 1$	(Chesters, 1991)
	breakage frequency	$g(r) = 2^{\left(-\frac{2}{3}\right)}k_{b1}\frac{\varepsilon^{\left(\frac{1}{3}\right)}}{r^{\left(\frac{2}{3}\right)}}\left(erfc(w^{0.5}) + \frac{2}{\pi^{0.5}}w^{0.5}\exp(-w)\right) \quad w_e = 2^{\left(\frac{8}{3}\right)}\frac{\rho_c\varepsilon^{\left(\frac{2}{3}\right)}}{\tau}r^{\left(\frac{5}{3}\right)} \quad w = 1.5\frac{k_{b2}}{w_e}$	$k_{b1} = 1 \quad k_{b2} = 0.5$	(Eskin et al., 2017)
	daughter distribution	$\beta_r(r',r) = 90\frac{r^2}{r'^3}\left(\frac{r}{r'}\right)^6\left(1-\left(\frac{r}{r'}\right)^3\right)^2$		(Hsia and Tavlarides, 1983)

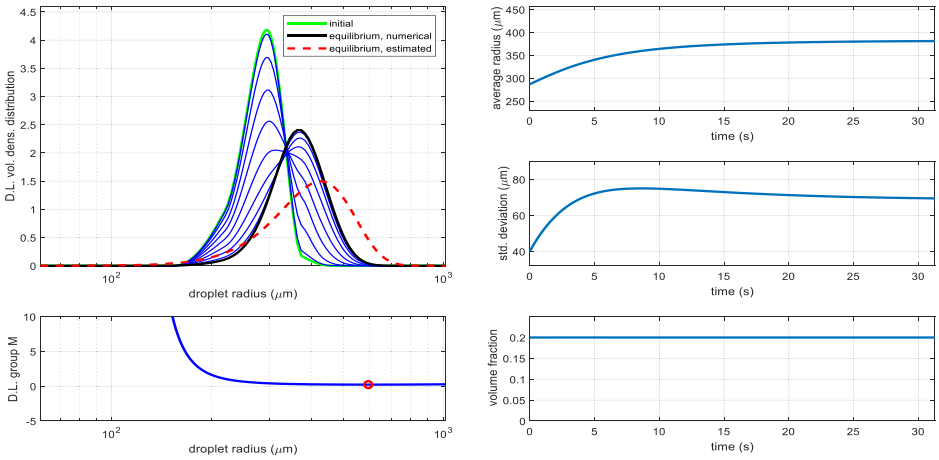

Fig. 2 – Comparison of estimated equilibrium distribution with numerical results for kernels #1, volume fraction = 0.2 and turbulence dissipation rate = 0.5 m^2s^{-3}.

Another influential parameter for the system behavior is dispersed phase volume fraction, which can significantly affect the system equilibrium and transient behavior. In this study, the two most influential parameters, namely, dispersed phase volume fraction as well as turbulence energy dissipation rate, are studied. The studied system is a typical water-in-oil emulsion, and the physiochemical parameters were kept constants for all the studied cases with numerical values as follows: dispersed phase density= 1000 kg/m^3, continuous phase density= 900 kg/m^3, interfacial surface tension: 30 mN/m.

The dynamic simulation results for the two extreme cases are depicted in the Figs. 2 and 3 for both sets of kernels. For all the simulations, the same initial distribution with an average point at 285 μm and standard deviation of 40 μm were used. The approximation technique is evaluated by comparing it with the results of the element-based orthogonal collocation technique with 20 collocation points per element (5-element fine grid for transient problem). It is worth noting that the estimated equilibrium distributions (dashed red curves) in the following figures are not the final result of the proposed technique but a starting point to perform more efficient computations for the PBE.

In Figs. 2 and 3, the evolution of the distribution is plotted from initial to equilibrium distribution and compared to the estimated equilibrium distribution. The estimated distributions almost always show tilting of the distribution peaks toward the left. It is worth noting that the estimated equilibrium distribution is inexact and deviates slightly from the simulated equilibrium distribution for Kernels #1 and #2. Nevertheless, in the case of a simple kernel, the estimated and simulated equilibrium distributions would be identical. This matter has been explained in more detail and used to verify the numerical technique in Section 4.3. Dimensionless

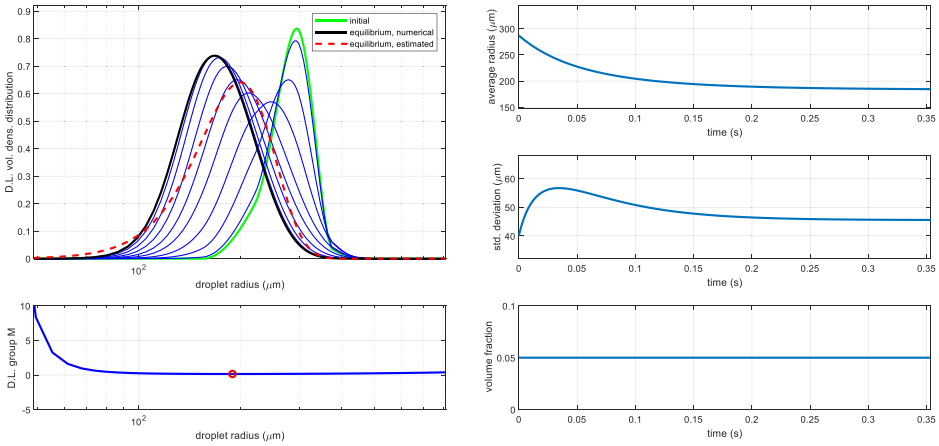

Fig. 3 – Comparison of estimated equilibrium distribution with numerical results for kernels #2, volume fraction = 0.05 and turbulence dissipation rate = 2 m^2s^{-3}.

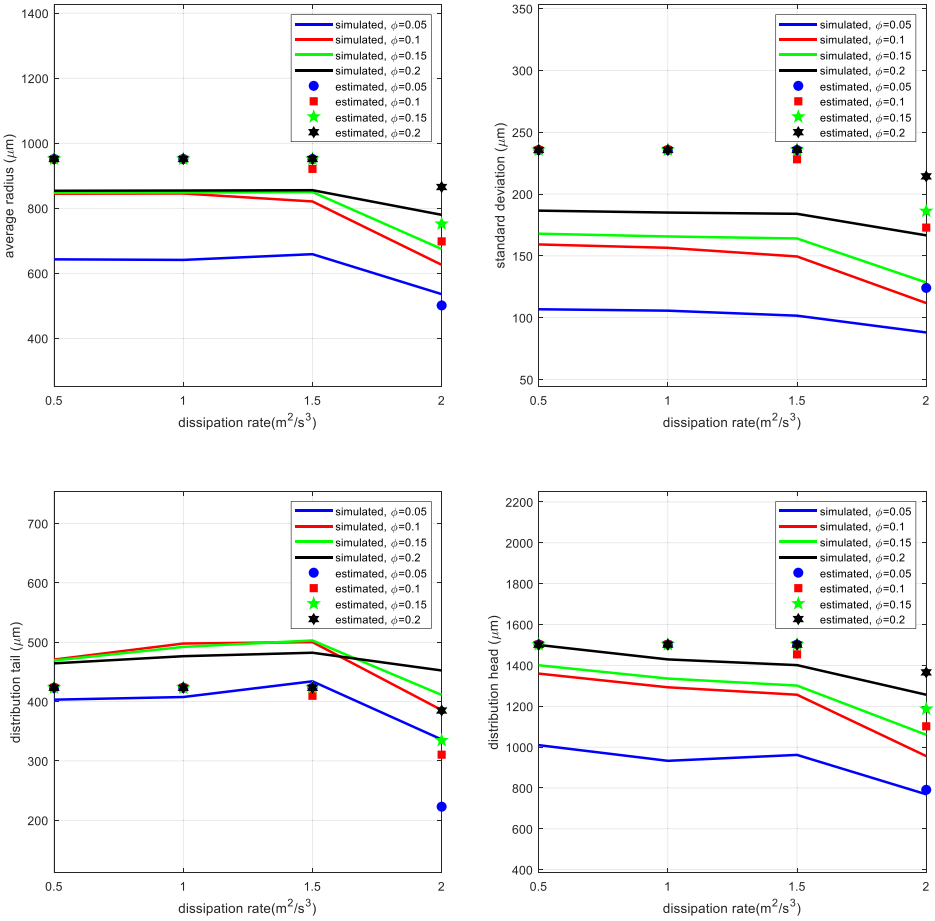

Fig. 4 – Comparison of estimated length scales with simulation results, kernels #1.

group M versus droplet size is also depicted in Figs. 2 and 3. This curve shows a minimum commonly close to the estimated average droplet radius.

4.1. *Approximated equilibrium length scales*

The approximated equilibrium length scales are depicted in Figs. 4 and 5 for kernels #1 and #2.

The technique provides less accurate estimations for extreme conditions with low volume fractions for the case of kernels #1. However, for the other more moderate conditions, the deviation is typically less than 20 % for heads, tails, and averages. Here, the tail is overpredicted while the head is underpredicted. Although it is not satisfactory to be used directly to analyze the system, this still suffices for generating element-based grids. Another important issue is the truncation point. Based on the mentioned results, a 100 % safety margin over the head seems a reasonable choice for truncation of the internal domain. Moreover, all the approximated length scales follow the same trend as that of the numerical simulation. The average droplet size for more moderate cases shows a deviation of around 12 %, while the approximation results for the standard deviation are not as satisfactory, having an average deviation of approximately 58 %.

Overall, the results for kernel #2 show much better agreement between the estimated and simulated length scales. Like the previous case, the estimated standard deviation shows the least agreement with an average deviation of 14 % ranging from 8 % for lower volume fractions to 25 % for higher volume fraction values. The average droplet is slightly overpredicted, with an average deviation of around 7 %. The distribution tail is well estimated with an average deviation of around 5 %. However, the deviation for the head ranges from 2 % for low volume fractions to about 20 % for high volume fractions. The estimated length scales

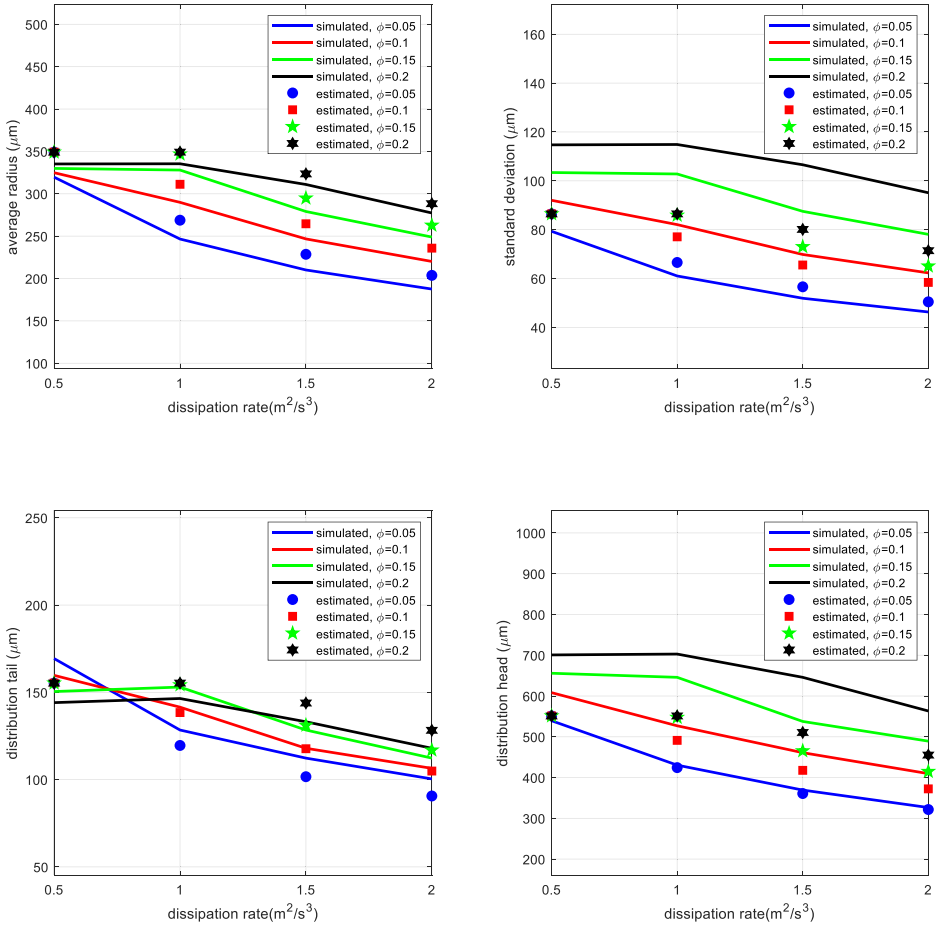

Fig. 5 – Comparison of estimated length scales with simulation results, kernels #2.

completely follow the trend of the simulated length scales. Same as Kernel #1, the results support the 100 % safety margin value over the estimated head for the truncation of the internal domain.

4.2. *Approximated transient time scale*

The estimated timescales based on the $t_{0.9}$ are compared with the simulation results in Fig. 6 for both sets of kernels.

According to Fig. 6, for kernel #1, the deviation for cases with initial and equilibrium distributions distant from each other is typically less than 30 %. However, the prediction accuracy can be influenced in cases with the initial and equilibrium distributions very close, with a deviation as high as 100 %. Similarly, for kernel #2, this deviation for most cases is less than 40%, while for severe cases, with close initial and equilibrium distributions can be as high as 150%. The mentioned issue makes direct usage of the estimated time scales limited. However, technique results can still be used for consequent cumbersome numerical computation by applying a safety margin. Practically, after a time equal to $3 \times t_{0.9}$, the system can be assumed in its equilibrium state. This value ($3 \times t_{0.9}$) provides an excellent choice to terminate the time integration for cases where the equilibrium distribution is desired.

4.3. *Evaluation of the numerical technique*

In this section, the element-based numerical grids are evaluated. The numerical scheme used for the transient PBE is verified versus the available analytical solution for the simple kernel (Benjamin and Madras, 2003) in Fig. 7. This figure has considered two different cases with various values for volume fraction and kernel constants. The grid with 20 collocation points per element perfectly agrees with the analytical solution. In contrast, similar cases with 10 collocation points indicate a slight deviation from the analytical solution.

Weighted residue methods (including orthogonal collocation technique), contrary to a method of classes (Kumar

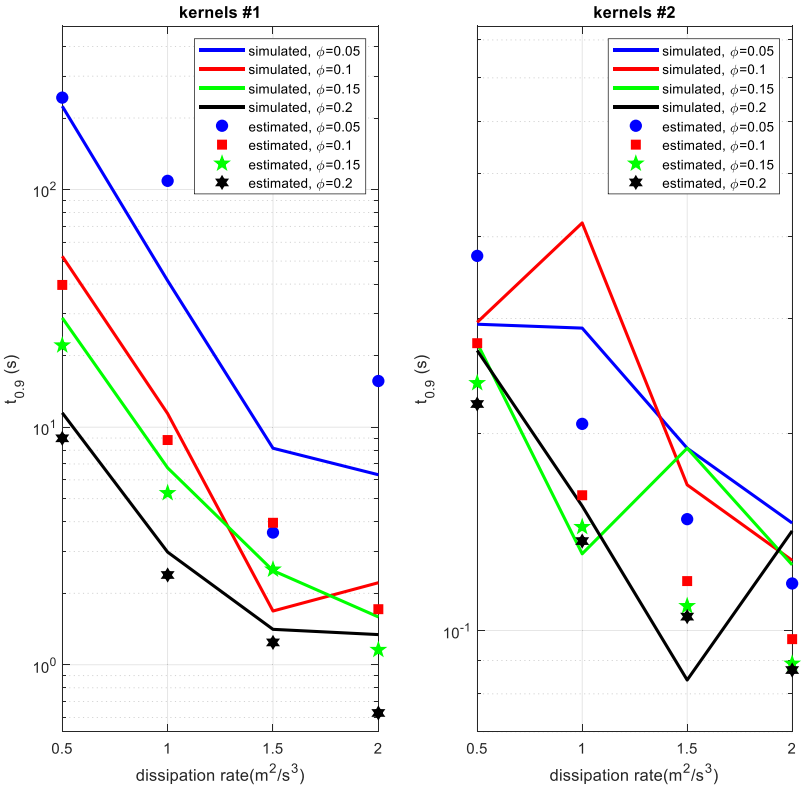

Fig. 6 – Comparison of estimated time scales ($t_{0.9}$) with simulation results.

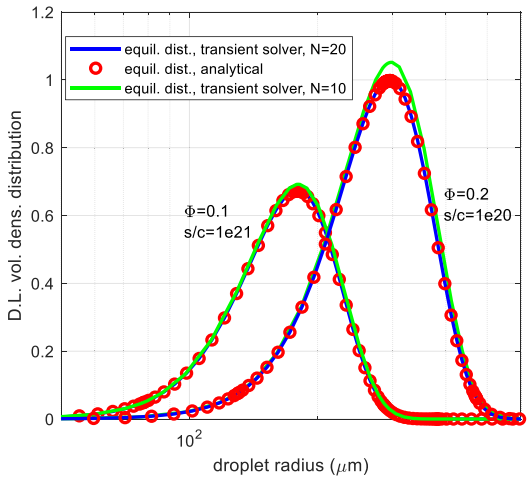

Fig. 7 – Comparison of the calculated equilibrium distribution using various grid sizes with the analytical solution.

and Ramkrishna, 1996a,b) and finite volume method (Filbet and Laurençot, 2004) are not a conservative, meaning that the moment properties like volume fraction are not conserved. For our current problem, the volume fraction is an excellent criterion to check the accuracy of the solution as it should be constant, and the deviation from it reveals the overall imbalance in the numerical solution. Hence, verifying the different grid sizes has been achieved using the deviation of the equilibrium volume fraction from its correct value. Both steady-state and transient solvers were evaluated for different cases using kernel #2 as well as the transient solver for the simple kernel. The results are presented in Table 2.

From Table 2, the numerical grid with 20 collocation points per element for the transient PBE can accurately predict the equilibrium distribution with a numerical imbalance close to a fraction of a percent. Similar grids with 15 collocation points can still provide an acceptable solution for a transient problem. However, by decreasing the number of collocation points to less than 10 per element, the accuracy of the solution drastically drops. The iterative scheme for steady-state PBE does not provide sufficient accuracy for the equilibrium distribution. Specifically, it seems that this iteration solution technique for PBE possesses some intrinsic errors that do not eliminate by refining the mesh. Hence, this

Table 2 – Percentage of the volume fraction deviation.

Studied cases		Collocation points per element			
		5	10	15	20
Kernel #2, transient solver	$\phi = 0.1, \varepsilon = 1$	12.03	1.73	0.33	0.08
	$\phi = 0.1, \varepsilon = 2$	5.10	1.06	0.15	0.02
	$\phi = 0.2, \varepsilon = 1$	20.53	2.59	0.47	0.04
	$\phi = 0.2, \varepsilon = 2$	17.71	1.71	0.22	0.07
Kernel #2, steady-state solver	$\phi = 0.1, \varepsilon = 1$	28.16	15.20	14.91	14.86
	$\phi = 0.1, \varepsilon = 2$	52.41	21.99	19.12	18.43
	$\phi = 0.2, \varepsilon = 1$	39.53	-13.79	-11.43	-11.49
	$\phi = 0.2, \varepsilon = 2$	31.62	17.13	16.47	15.43
Simple Kernel, transient solver	$\phi = 0.1, s/c = 10^{20}$	84.60	6.02	1.12	0.33
	$\phi = 0.1, s/c = 10^{21}$	55.87	3.55	0.66	0.48
	$\phi = 0.2, s/c = 10^{20}$	93.70	6.65	0.72	0.33
	$\phi = 0.2, s/c = 10^{21}$	60.43	3.71	2.23	0.85

Table 3 – Percentage of the decrease in the computation time.

Turbulence dissipation rate (m^2/s^3)	Volume fraction			
	0.05	0.10	0.15	0.20
0.5	67.8	43.5	45.9	57.9
1	56.1	61.3	59.2	65.0
1.5	65.2	64.8	59.6	63.4
2	62.8	68.1	63.7	59.9

technique is not recommended for calculating the equilibrium distribution. Alternatively, a transient solution from the initial distribution as the estimated equilibrium distribution is recommended. The mentioned approach can significantly decrease the computational time required for the solution of the steady-state PBE. The percentage of reduction in the computational time obtained by this technique is summarized in Table 3 for various studied cases using kernel #2. The values are calculated by comparing the computation times of the cases with the initial conditions the same as that in Fig. 3 and the estimated equilibrium distribution. The final simulation time was set as $3 \times t_{0.9}$ with $t_{0.9}$ calculated using the case with the initial condition depicted in Fig. 3. The same absolute final simulation time was also used for the counterpart cases with the initial condition as estimated equilibrium distribution.

Accordingly, this approach has decreased the required computational time by around 40–70%. It must be noted that the decrease in the computation time can be enormously influenced by the distance between the initial and equilibrium distributions. For cases with higher distances, one can expect better improvement in computation efficiency.

5. Conclusion

Based on extrapolating the available analytical solution for the spatially homogeneous PBE with simple breakage and coalescence kernels, a new approach was developed to estimate the equilibrium and transient properties of the problem in the form of the length and time scales of the system. Furthermore, this approach was generalized to any generalized form of breakage and coalescence relations.

All the approximated equilibrium distribution properties have a linear relation with respect to a dimensionless group. In other words, the equilibrium distribution of the system is mainly governed by this dimensionless group. This group shows dependency only on the breakage and coalescence kernels as well as the volume fraction of the dispersed phase.

Similarly, the derived relation for the transient time of the system only shows simple explicit relation concerning kernels and volume fraction and influenced by a term which determines how remote the system is from equilibrium state. This term can predict the direction that the distribution is likely to evolve.

The derived relations for time and length scales were compared with the numerical results of the orthogonal collocation method. The test cases were selected according to two available sets of kernels used for liquid-liquid dispersion. The most influential system parameters were studied, namely, turbulence dissipation rate and volume fraction. Overall, the approximation technique provides satisfactory preliminary information about the time and length scales of the system for the purpose of numerical grid generation and numerical computation.

The derived approximate equilibrium length scales of the system were used to generate element-based orthogonal collocation grids for both transient (5 elements) and steady-state (4 elements) PBE. Grids of different sizes were evaluated by comparing them to the available analytical solution as well as checking the numerical value for the volume fraction deviation.

The results suggest that number of collocation points between 10 and 20 can be selected by a trade-off between the desired accuracy and computation time. The iterative scheme for steady-state PBE does not provide sufficient accuracy. Alternatively, a transient solution from the initial distribution as the estimated equilibrium distribution is recommended. This approach has decreased the required computational time by around 40–70% for the studied cases.

The above evidence suggests that the technique has high potential to address the well-known computational efficiency and robustness challenges associated with the numerical solution of PBEs. In our future publications, we will address these issues for more complex systems.

Declaration of Competing Interest

The authors declare that they have no known competing financial interests or personal relationships that could have appeared to influence the work reported in this paper.

Acknowledgments

This work was carried out as a part of SUBPRO, a Research-Based Innovation Center within Subsea Production and Processing. The authors gratefully acknowledge the financial support from SUBPRO, which is financed by the Research Council of Norway, major industry partners, and NTNU.

Appendix A. Supporting information

Supplementary data associated with this article can be found in the online version at doi:10.1016/j.cherd.2022.10.044.

References

Attarakih, M.M., Bart, H.J., Faqir, N.M., 2002. An approximate optimal moving grid technique for the solution of discretized population balances in batch. Comput. Aided Chem. Eng. 823–828. https://doi.org/10.1016/S1570-7946(02)80165-1

Attarakih, M.M., Bart, H.J., Faqir, N.M., 2004. Numerical solution of the spatially distributed population balance equation describing the hydrodynamics of interacting liquid-liquid dispersions. Chem. Eng. Sci. 59, 2567–2592. https://doi.org/10.1016/j.ces.2004.03.005

Benjamin, B.J., Madras, G., 2003. Analytical solution for a population balance equation with aggregation and fragmentation. Chem. Eng. Sci. 58, 3049–3051. https://doi.org/10.1016/S0009-2509(03)00159-3

Briesen, H., 2009. Adaptive moving pivot technique for growth dominated population balance equations. Comput. Aided Chem. Eng. 26, 895–900. https://doi.org/10.1016/S1570-7946(09)70149-X

Chesters, A.A., 1991. The modelling of coalescence processes in fluid-liquid dispersions: a review of current understanding. Chem. Eng. Res. Des. 69, 259–270.

Costa, L.I., Storti, G., Lazzari, S., 2018. Solution of population balance equations by logarithmic shape preserving interpolation on finite elements. Comput. Chem. Eng. 119, 13–24. https://doi.org/10.1016/j.compchemeng.2018.08.008

Coulaloglou, C.A., Tavlarides, L.L., 1977. Description of interaction processes in agitated liquid-liquid dispersions. Chem. Eng. Sci. 32, 1289–1297. https://doi.org/10.1016/0009-2509(77)85023-9

Dorao, C.A., Jakobsen, H.A., 2006. A least squares method for the solution of population balance problems. Comput. Chem. Eng. 30, 535–547. https://doi.org/10.1016/j.compchemeng.2005.10.012

Duarte, B.P.M., Baptista, C.M.S.G., 2007. Using moving finite elements method to solve population balance equations comprising breakage terms. Comput. Aided Chem. Eng. 24, 255–260. https://doi.org/10.1016/S1570-7946(07)80066-6

Eskin, D., Taylor, S., Ma, S.M., Abdallah, W., 2017. Modeling droplet dispersion in a vertical turbulent tubing flow. Chem. Eng. Sci. 173, 12–20. https://doi.org/10.1016/j.ces.2017.07.023

Falola, A., Borissova, A., Wang, X.Z., 2013. Extended method of moment for general population balance models including size dependent growth rate, aggregation and breakage kernels. Comput. Chem. Eng. 56, 1–11. https://doi.org/10.1016/j.compchemeng.2013.04.017

Filbet, F., Laurençot, P., 2004. Numerical simulation of the Smoluchowski coagulation equation. SIAM J. Sci. Comput. 25, 2004–2028. https://doi.org/10.1137/S1064827503429132

Fritsch, F.N., Carlson, R.E., 1980. Monotone Piecewise cubic interpolation. SIAM J. Numer. Anal. 17, 238–246. https://doi.org/10.1137/0717021

Gelbard, F., Seinfeld, J.H., 1978. Numerical solution of the dynamic equation for particulate systems. J. Comput. Phys. 28, 357–375. https://doi.org/10.1016/0021-9991(78)90058-X

Hsia, M.A., Tavlarides, L.L., 1983. Simulation analysis of drop breakage, coalescence and micromixing in liquid-liquid stirred tanks. Chem. Eng. J. 26, 189–199. https://doi.org/10.1016/0300-9467(83)80014-8

Kumar, S., Ramkrishna, D., 1996a. On the solution of population balance equations by discretization - I. A fixed pivot technique. Chem. Eng. Sci. 51, 1311–1332. https://doi.org/10.1016/0009-2509(96)88489-2

Kumar, S., Ramkrishna, D., 1996b. On the solution of population balance equations by discretization - II. A moving pivot technique. Chem. Eng. Sci. 51, 1333–1342. https://doi.org/10.1016/0009-2509(95)00355-X

Lee, G., Yoon, E.S., Young-Il Lim, Jean Marc Le. Lann, Xuân-Mi Meyer, A., Joulia, X., 2001. Adaptive mesh method for the simulation of crystallization processes including agglomeration and breakage: the potassium sulfate system. Ind. Eng. Chem. Res. 40, 6228–6235. https://doi.org/10.1021/IE010443R

Mahoney, A.W., Ramkrishna, D., 2002. Efficient solution of population balance equations with discontinuities by finite elements. Chem. Eng. Sci. 57, 1107–1119. https://doi.org/10.1016/S0009-2509(01)00427-4

Mantzaris, N.V., Daoutidis, P., Srienc, F., 2001a. Numerical solution of multi-variable cell population balance models. II. Spectral methods. Comput. Chem. Eng. 25, 1441–1462. https://doi.org/10.1016/S0098-1354(01)00710-4

Mantzaris, N.V., Daoutidis, P., Srienc, F., 2001b. Numerical solution of multi-variable cell population balance models. III. Finite element methods. Comput. Chem. Eng. 25, 1463–1481. https://doi.org/10.1016/S0098-1354(01)00711-6

Nicmanis, M., Hounslow, M.J., 1996. A finite element analysis of the steady state population balance equation for particulate systems: aggregation and growth. Comput. Chem. Eng. 20, S261–S266. https://doi.org/10.1016/0098-1354(96)00054-3

Nicmanis, M., Hounslow, M.J., 1998. Finite-element methods for steady-state population balance equations. AIChE J. 44, 2258–2272. https://doi.org/10.1002/aic.690441015

Prince, M.J., Blanch, H.W., 1990. Bubble coalescence and break-up in air-sparged bubble columns. Aiche J. 36, 1485–1499. https://doi.org/10.1002/aic.690361004

Qamar, S.M., 2014. Application of the method of characteristics to population balance models considering growth and nucleation phenomena. Appl. Math. 5, 1853–1862. https://doi.org/10.4236/am.2014.513178

Ramkrishna, D., 2000. Population Balances: Theory and Applications to Particulate Systems in Engineering. Academic Presshttps://doi.org/10.1016/B978-0-12-576970-9.X5000-0

Rigopoulos, S., Jones, A.G., 2003. Finite-element scheme for solution of the dynamic population balance equation. AIChE J. 49, 1127–1139. https://doi.org/10.1002/aic.690490507

Sewerin, F., Rigopoulos, S., 2017. An explicit adaptive grid approach for the numerical solution of the population balance equation. Chem. Eng. Sci. 168, 250–270. https://doi.org/10.1016/j.ces.2017.01.054

Solsvik, J., Jakobsen, H.A., 2012. Effects of Jacobi polynomials on the numerical solution of the pellet equation using the orthogonal collocation, Galerkin, tau and least squares methods. Comput. Chem. Eng. 39, 1–21. https://doi.org/10.1016/j.compchemeng.2011.11.015

Solsvik, J., Jakobsen, H.A., 2013. Evaluation of weighted residual methods for the solution of a population balance model describing bubbly flows: the least-squares, Galerkin, Tau, and

orthogonal collocation methods. Ind. Eng. Chem. Res. 52 (45), 15988–16013. https://doi.org/10.1021/ie402033b

Vankova, N., Tcholakova, S., Denkov, N.D., Vulchev, V.D., Danner, T., 2007. Emulsification in turbulent flow. 2. Breakage rate constants. J. Colloid Interface Sci. 313, 612–629. https://doi.org/10.1016/J.JCIS.2007.04.064

Villadsen, J., Michelsen, M.L., 1978. Solution of Differential Equation Models by Polynomial Approximation. Prentice-Hall, Englewood Cliffs, New York.

Zhu, Z., Dorao, C.A., Jakobsen, H.A., 2008. A least-squares method with direct minimization for the solution of the breakage-coalescence population balance equation. Math. Comput. Simul. 79, 716–727. https://doi.org/10.1016/j.matcom.2008.05.001

Zhu, Z., Dorao, C.A., Lucas, D., Jakobsen, H.A., 2009. On the coupled solution of a combined population balance model using the least-squares spectral element method. Ind. Eng. Chem. Res. 48, 7994–8006. https://doi.org/10.1021/ie900088q

Supplementary material for chapter 3

1. Derivation of truncated dimensionless radius-based PBE for volume density

A population balance equation for a spatially homogeneous particulate system without inflow/outflow considering volume-based number density can be written as:

$$\frac{\partial f_{n,v}(v,t)}{\partial t} = \int_v^\infty 2g(v')\beta_v(v',v)f_{n,v}(v',t)\,dv' - g(v)f_{n,v}(v,t) + \int_0^{v/2} k(v', v - v')f_{n,v}(v',t)f_{n,v}(v-v',t)\,dv' - f_{n,v}(v,t)\int_0^\infty k(v',v)f_{n,v}(v',t)dv' \quad \text{(S1)}$$

where the terms on the right-hand side of the equation from left to right are breakage birth, breakage death, coalescence birth, coalescence death. v is dispersed phase droplet size, t is time, $f_{n,v}(v,t)$ is the volume-based number density for droplet size v at time t, $g(v)$ is the breakage frequency for droplet size v, $\beta_v(v',v)$ is the volume-based daughter distribution of droplet size v resultant from breakage of droplet size v', and $k(v',v)$ is the rate of coalescence between droplet sizes of v' and v. The factor 2 in the breakage birth term appeared as only binary breakage of droplets are considered in this study. It is possible to transform the PBE to radius-based formulation. To do that, the volume-based number density should be replaced by its equivalent radius-based number density. This can be done by equating the volume fraction equations according to both distribution definitions as follows:

$$\begin{cases} \phi = \int_0^\infty v f_{n,v}dv = \int_0^\infty v f_{n,r}dr \\ dv = 4\pi r^2 dr \end{cases} \quad \rightarrow \quad f_{n,v} = \frac{f_{n,r}}{4\pi r^2} \quad \text{(S2)}$$

Similarly, volume-based daughter distribution can be transformed to its equivalent radius-based form as:

$$\beta_v(v',v) = \frac{\beta_r(r',r)}{4\pi r^2} \quad \text{(S3)}$$

By replacing $f_{n,v}$, β_v and v , PBE for radius-based number density takes the following form:

$$\frac{\partial f_{n,r}(r,t)}{\partial t} = \int_r^\infty 2g(r')\beta_r(r',r)f_{n,r}(r',t)\,dr' - g(r)f_{n,r}(r,t) + \int_0^{r/\sqrt[3]{2}} k(r',r'')f_{n,r}(r',t)f_{n,r}(r'',t)\frac{r^2}{r''^2}dr' - f_{n,r}(r,t)\int_0^\infty k(r',r)f_{n,r}(r',t)dr' \quad \text{(S4)}$$

where r'' is the equivalent radius for a droplet size of $v - v'$ and is equal to $(r^3 - r'^3)^{1/3}$. The interested reader can also refer to [1] for more details about the derivation of this form of PBE. It is important to notice that in the above equation, $f_{n,r}$ and β_r are now defined in the new

radius-based frame of reference having different dimensionality from the previous variables. Similarly, the upper bound of the integral for the coalescence birth rate ($v/2$) is now replaced with equivalent droplet radius which gives the same droplet volume ($r/\sqrt[3]{2}$). The following features can now be derived from a radius-based number density distribution as follows:

$$N(t) = \int_0^\infty f_{n,r}(r',t)dr' \tag{S5}$$

$$\phi(t) = \int_0^\infty v f_{n,r}(r',t)dr' \tag{S6}$$

$$\mu_r(t) = \frac{1}{\phi(t)}\int_0^\infty r' v f_{n,r}(r',t)dr' \tag{S7}$$

$$\sigma_r(t) = \left(\frac{1}{\phi(t)}\int_0^\infty (r'-\mu_r(t))^2 v f_{n,r}(r',t)dr'\right)^{0.5} \tag{S8}$$

where N, ϕ, μ_r and σ_r are the total number of droplets per unit volume, volume fraction, average droplet radius, and droplet radius standard deviation, respectively. The next step is to convert number density distribution to volume density distribution ($f_{v,r} = v f_{n,r}$) to make working with DSD more numerically convenient. Therefore, PBE for radius-based volume density distribution can be written as follows:

$$\begin{aligned}\frac{\partial f_{v,r}(r,t)}{\partial t} &= \int_r^\infty 2g(r')\beta_r(r',r)f_{v,r}(r',t)\frac{r^3}{r'^3}dr' - g(r)f_{v,r}(r,t) + \\ &\frac{3}{4\pi}\int_0^{r/\sqrt[3]{2}} k(r',r'')f_{v,r}(r',t)f_{v,r}(r'',t)\frac{r^5}{r'^3 r''^5}dr' - \\ &\frac{3}{4\pi}f_{v,r}(r,t)\int_0^\infty k(r',r)f_{v,r}(r',t)\frac{1}{r'^3}dr'\end{aligned} \tag{S9}$$

Since the upper bound of the breakage birth term, as well as that of coalescence death rate, is infinity, we need to truncate the inner dimension of the PBE so that be able to analyze the problem numerically. By truncating the domain to a maximum droplet radius (r_m), the PBE is obtained as follows:

$$\begin{aligned}\frac{\partial f_{v,r}(r,t)}{\partial t} &= r^3\int_r^{r_m} 2g(r')\beta_r(r',r)f_{v,r}(r',t)\frac{r^3}{r'^3}dr' - g(r)f_{v,r}(r,t) + \\ &\frac{3}{4\pi}\int_0^{r/\sqrt[3]{2}} k(r',r'')f_{v,r}(r',t)f_{v,r}(r'',t)\frac{r^5}{r'^3 r''^5}dr' - \\ &\frac{3}{4\pi}f_{v,r}(r,t)\int_0^{r_m} k(r',r)f_{v,r}(r',t)\frac{1}{r'^3}dr'\end{aligned} \tag{S10}$$

By making all variables dimensionless ($\hat{r} = r/r_m, \hat{t} = t/t_c, \hat{f}_{v,r} = f_{v,r}r_m$), Eq. S10 yields as:

$$\frac{\partial \hat{f}_{v,r}(\hat{r},\hat{t})}{\partial \hat{t}} = (t_c r_m)\int_{\hat{r}}^{1} 2g(\hat{r}')\beta_r(\hat{r}',\hat{r})\hat{f}_{v,r}(\hat{r}',\hat{t})\frac{\hat{r}^3}{\hat{r}'^3}d\hat{r}' - t_c g(\hat{r})\hat{f}_{v,r}(\hat{r},\hat{t}) + \left(\frac{t_c}{v_m}\right)\int_{0}^{\hat{r}/\sqrt[3]{2}} k(\hat{r}',\hat{r}'')\hat{f}_{v,r}(\hat{r}',\hat{t})\hat{f}_{v,r}(\hat{r}'',\hat{t})\frac{\hat{r}^5}{\hat{r}'^3\hat{r}''^5}d\hat{r}' - \left(\frac{t_c}{v_m}\right)\hat{f}_{v,r}(\hat{r},\hat{t})\int_{0}^{1} k(\hat{r}',\hat{r})\hat{f}_{v,r}(\hat{r}',\hat{t})\frac{1}{\hat{r}'^3}d\hat{r}' \quad \text{(S11)}$$

where $v_m$is the droplet volume equivalent to a droplet with radius r_m and t_c is an arbitrary time scale for the system under the study. It must be noted that, in Eq. S11, the kernels (g, β_r and k) have still dimensions. Now, in the mentioned PBE framework, the distribution features can be conveniently computed by:

$$N(\hat{t}) = \frac{1}{v_m}\int_{0}^{1}\frac{\hat{f}_v(\hat{r},\hat{t})}{\hat{r}^3}d\hat{r} \quad \text{(S12)}$$

$$\phi(\hat{t}) = \int_{0}^{1}\hat{f}_v(\hat{r},\hat{t})d\hat{r} \quad \text{(S13)}$$

$$\hat{\mu}_r(\hat{t}) = \frac{\mu_r(\hat{t})}{r_m} = \frac{1}{\phi(\hat{t})}\int_{0}^{1}\hat{f}_v(\hat{r},\hat{t}).\hat{r}.d\hat{r} \quad \text{(S14)}$$

$$\hat{\sigma}_r(\hat{t}) = \frac{\sigma_r(\hat{t})}{r_m} = \left(\frac{1}{\phi(\hat{t})}\int_{0}^{1}(\hat{r}-\hat{\mu}_r)^2\hat{f}_v(\hat{r},\hat{t})d\hat{r}\right)^{0.5} \quad \text{(S15)}$$

where N, ϕ, $\hat{\mu}_r$ and $\hat{\sigma}_r$ are the total number of droplets per unit volume, volume fraction, dimensionless average droplet radius, and dimensionless droplet radius standard deviation, respectively.

2. Analytical solution for simple breakage and coalescence kernels

We consider PBE subject to a simple set of kernel functions as follows:

$$g(r) = sr^3 \quad \text{(S16)}$$

$$k(r',r) = c \quad \text{(S17)}$$

$$\beta_r(r',r) = 3\frac{r^2}{r'^3} \quad \text{(S18)}$$

where s and c are constant values. For steady-state, subject to the mentioned kernels, Eq. S11 can be rearranged to the following dimensionless form by replacing the kernels.

$$6\left[\frac{sr_m^6}{c}\right]\int_{\hat{r}}^{1}\hat{f}_{v,r}(\hat{r}',\hat{t})\frac{\hat{r}^5}{\hat{r}'^3}d\hat{r}' - \left[\frac{sr_m^6}{c}\right]\hat{r}^3\hat{f}_{v,r}(\hat{r},\hat{t}) +$$

$$\frac{3}{4\pi}\int_0^{\frac{\hat{r}}{\sqrt[3]{2}}}\hat{f}_{v,r}(\hat{r}',\hat{t})\hat{f}_v(\hat{r}'',\hat{t})\frac{\hat{r}^5}{\hat{r}'^3\hat{r}''^5}d\hat{r}' - \frac{3}{4\pi}\hat{f}_{v,r}(\hat{r},\hat{t})\int_0^1\hat{f}_v(\hat{r}',\hat{t})\frac{1}{\hat{r}'^3}d\hat{r}' = 0 \quad \text{(S19)}$$

The above equation reveals that the equilibrium distribution of a particulate system subject to these simple kernels can be characterized merely by one dimensionless group which is sr_m^6/c.

An analytical solution to this problem has been proposed by Benjamin and Madras [2] for volume-based formulation. The equivalent length-based version of the solution has been presented by Bhutani et. al [3], where they utilized it to validate their numerical simulation results. Benjamin and Madras [2] solved transient PBE for the mentioned system subject to an initial number density given by:

$$f_{n,r}(r,0) = 3\frac{m_0(0)^2}{m_3}r^2\exp\left(-\frac{m_0(0)}{m_3}r^3\right) \quad \text{(S20)}$$

Their analytical solution has the following simple exponential form:

$$f_{n,r}(r,t) = k_1(t)r^2\exp\left(-k_2(t)r^3\right) \quad \text{(S21)}$$

where k_1 and k_2 are given by:

$$k_1(t) = 3\hat{n}(t)^2\frac{m_0(0)^2}{m_3} \quad \text{(S22)}$$

$$k_2(t) = \hat{n}(t)\frac{m_0(0)}{m_3} \quad \text{(S23)}$$

where $m_0(0)$ is 0[th] order moment and equivalent to the total number of droplets at initial condition. m_3 is the 3[rd] order moment and related to the volume fraction of the dispersed phase by $m_3 = 3\phi/4\pi$. $\hat{n}$ is also defined as:

$$\hat{n}(t) = \hat{n}(\infty)\left[\frac{1+\hat{n}(\infty)\tanh\left(\hat{n}(\infty)\frac{m_0(0)ct}{2}\right)}{\hat{n}(\infty)+\tanh\left(\hat{n}(\infty)\frac{m_0(0)ct}{2}\right)}\right] \quad \text{(S24)}$$

$$\hat{n}(\infty) = \left(\frac{2sm_3}{c}\right)^{\frac{1}{2}}\left(\frac{1}{m_0(0)}\right) \quad \text{(S25)}$$

Similarly, by changing the number density to volume density and making all the variables dimensionless, Eq. S21 takes the following form.

$$\hat{f}_{v,r}(r,t) = \hat{k}_1(t)\hat{r}^5\exp\left(-\hat{k}_2(t)\hat{r}^3\right) \quad \text{(S26)}$$

where $\hat{k}_1$ and $\hat{k}_2$ are as follows:

$$\hat{k}_1(t) = 4\pi\hat{n}(t)^2 \frac{{m_0(0)}^2}{m_3} {r_m}^6 \tag{S27}$$

$$\hat{k}_2(t) = \hat{n}(t) \frac{m_0(0)}{m_3} {r_m}^3 \tag{S28}$$

By setting time in Eq. S27 and S28 to infinity, equilibrium distribution yields using $\hat{k}_1$ and $\hat{k}_2$ as follows:

$$\hat{k}_1(\infty) = 8\pi(\frac{s}{c}{r_m}^6) \tag{S29}$$

$$\hat{k}_2(\infty) = \left(\frac{8\pi}{3}\right)^{1/2} \left(\frac{1}{\phi}\frac{s}{c}{r_m}^6\right)^{\frac{1}{2}} \tag{S30}$$

2.1. Dimensionless average radius:

Transient dimensionless average droplet radius is obtained by integrating the transient dimensionless volume density distribution (Eq. S26) using average radius definition (Eq. S14) over the domain between $0 - \infty$. There is an analytical expression for this mentioned integral as below:

$$\hat{\mu}_r(t) = \frac{16\pi\,\Gamma^{-1}(1/3,0)}{27}\left(\frac{3}{4\pi}\right)^{4/3} \frac{\phi^{\frac{1}{3}}}{r_m \hat{n}(t)^{\frac{1}{3}} {m_0(0)}^{\frac{1}{3}}} \cong\ 0.7386 \frac{\phi^{\frac{1}{3}}}{r_m \hat{n}(t)^{\frac{1}{3}} {m_0(0)}^{\frac{1}{3}}} \tag{S31}$$

where Γ^{-1} is inverse gamma function. By replacing $\hat{n}(t)$ with $\hat{n}(\infty)$ from Eq. S25 together with some simplifications, the dimensionless average radius of the equilibrium distribution is obtained as:

$$\hat{\mu}_r(\infty) = \frac{4}{9}\left(\frac{3}{8\pi}\right)^{\frac{1}{6}} \Gamma^{-1}(1/3,0) \left(\frac{\phi}{\frac{s}{c}{r_m}^6}\right)^{\frac{1}{6}} \cong 0.8355 \left(\frac{\phi}{\frac{s}{c}{r_m}^6}\right)^{\frac{1}{6}} \tag{S32}$$

2.2. Dimensionless radius standard deviation

Transient dimensionless standard deviation is obtained by integrating transient dimensionless volume density distribution (Eq. S26) using Eq. S15 over the domain between $0 - \infty$ analytically as follows.

$$\hat{\sigma}_r(t) = \frac{\hat{k}_1(t)^{0.5}}{\phi^{0.5}}\left(\frac{1}{3}\frac{\hat{\mu}_r(t)^2}{\hat{k}_2(t)^{6/3}} - \frac{8\Gamma^{-1}(1/3,0)}{27}\frac{\hat{\mu}_r(t)}{\hat{k}_2(t)^{7/3}} + \frac{10\Gamma^{-1}(2/3,0)}{27}\frac{1}{\hat{k}_2(t)^{8/3}}\right)^{0.5} \quad \text{(S33)}$$

$$\hat{\sigma}_r(t) \cong \frac{\hat{k}_1(t)^{0.5}}{\phi^{0.5}}\left(0.3333\frac{\hat{\mu}_r(t)^2}{\hat{k}_2(t)^{6/3}} - 0.7938\frac{\hat{\mu}_r(t)}{\hat{k}_2(t)^{7/3}} + 0.5015\frac{1}{\hat{k}_2(t)^{8/3}}\right)^{0.5} \quad \text{(S34)}$$

By replacing $\hat{k}_1(t)$, $\hat{k}_2(t)$, and $\hat{\mu}_r(t)$ with $\hat{k}_1(\infty), \hat{k}_2(\infty)$, and $\hat{\mu}_r(\infty)$, respectively, the dimensionless radius standard deviation of the equilibrium distribution is obtained by some simplifications as:

$$\hat{\sigma}_r(\infty) = \frac{1}{9}\left(\frac{3}{8\pi}\right)^{\frac{1}{6}}\left(90\Gamma^{-1}\left(\frac{2}{3},0\right) - 16\Gamma^{-1}\left(\frac{1}{3},0\right)^2\right)^{0.5}\left(\frac{\phi}{\frac{5}{c}r_m{}^6}\right)^{\frac{1}{6}} \cong 0.2069\left(\frac{\phi}{\frac{5}{c}r_m{}^6}\right)^{\frac{1}{6}}$$

(S35)

2.3. Dimensionless peak radius

Transient dimensionless distribution peak is obtained by setting the first derivative of transient dimensionless volume density distribution (Eq. S26) to zero.

$$\hat{r}_{peak}(t) = \left(\frac{5}{3\hat{k}_2(t)}\right)^{1/3} \quad \text{(S36)}$$

Similarly, by replacing $\hat{k}_2(t)$ with $\hat{k}_2(\infty)$, the dimensionless peak radius of the equilibrium distribution is obtained as:

$$\hat{r}_{peak} = \left(\frac{25}{24\pi}\right)^{\frac{1}{6}}\left(\frac{\phi}{\frac{5}{c}r_m{}^6}\right)^{\frac{1}{6}} \cong 0.8319\left(\frac{\phi}{\frac{5}{c}r_m{}^6}\right)^{\frac{1}{6}} \quad \text{(S37)}$$

2.4. Dimensionless head and tail radius of distribution:

Head and tail of a transient distribution can be obtained by first selecting a value for x between 0-1 and then solving the equation $\phi_x = x\phi = \int_0^{\hat{r}_x} \hat{f}_{v,r}\, d\hat{r}$ for $\hat{r}_x$. Some further simplification of the eqution gives the following nonlinear equation.

$$\left(\hat{k}_2(t)\hat{r}_x^3 + 1\right)\exp\left(-\hat{k}_2(t)\hat{r}_x^3\right) - (1-x) = 0 \quad \text{(S38)}$$

3. Iterative solution scheme for steady-state PBE

Consider the following truncated dimensionless radius-based steady-state PBE for the volume density.

$$0 = (r_m)\int_{\hat{r}}^{1} 2g(\hat{r}')\beta_r(\hat{r}',\hat{r})\hat{f}_{v,r}(\hat{r}')\frac{\hat{r}^3}{\hat{r}'^3}d\hat{r}' - g(\hat{r})\hat{f}_{v,r}(\hat{r}) + \left(\frac{1}{v_m}\right)\int_0^{\hat{r}/\sqrt[3]{2}} k(\hat{r}',\hat{r}'')\hat{f}_{v,r}(\hat{r}')\hat{f}_{v,r}(\hat{r}'')\frac{\hat{r}^5}{\hat{r}'^3\hat{r}''^5}d\hat{r}' - \left(\frac{1}{v_m}\right)\hat{f}_{v,r}(\hat{r})\int_0^{1} k(\hat{r}',\hat{r})\hat{f}_{v,r}(\hat{r}')\frac{1}{\hat{r}'^3}d\hat{r}' \quad \text{(S39)}$$

Discretization of this equation results in a non-linear set of equations. Our proposed numerical scheme for that is an iterative scheme. In Eq. S39, there are two factorable $\hat{f}_{v,r}(\hat{r})$ terms in the breakage and coalescence death rates. By doing this factorization and solving for this term, the equation becomes:

$$\hat{f}_{v,r}(\hat{r}) = \frac{(r_m)\int_{\hat{r}}^{1} 2g(\hat{r}')\beta_r(\hat{r}',\hat{r})\hat{f}_{v,r}(\hat{r}')\frac{\hat{r}^3}{\hat{r}'^3}d\hat{r}' + \left(\frac{1}{v_m}\right)\int_0^{\hat{r}/\sqrt[3]{2}} k(\hat{r}',\hat{r}'')\hat{f}_{v,r}(\hat{r}')\hat{f}_{v,r}(\hat{r}'')\frac{\hat{r}^5}{\hat{r}'^3\hat{r}''^5}d\hat{r}'}{g(\hat{r}) + \left(\frac{1}{v_m}\right)\int_0^{1} k(\hat{r}',\hat{r})\hat{f}_{v,r}(\hat{r}')\frac{1}{\hat{r}'^3}d\hat{r}'} \quad \text{(S40)}$$

The iterative formula can now be derived by keeping the numerical value of the right-hand side terms in the previous iteration and updating the value for $\hat{f}_{v,r}(\hat{r})$ vector accordingly.

$$\hat{f}_{v,r}{}^{(i+1)}(\hat{r}) := \frac{(r_m)\int_{\hat{r}}^{1} 2g(\hat{r}')\beta_r(\hat{r}',\hat{r})\hat{f}_{v,r}{}^{(i)}(\hat{r}')\frac{\hat{r}^3}{\hat{r}'^3}d\hat{r}' + \left(\frac{1}{v_m}\right)\int_0^{\hat{r}/\sqrt[3]{2}} k(\hat{r}',\hat{r}'')\hat{f}_{v,r}{}^{(i)}(\hat{r}')\hat{f}_{v,r}{}^{(i)}(\hat{r}'')\frac{\hat{r}^5}{\hat{r}'^3\hat{r}''^5}d\hat{r}'}{g(\hat{r}) + \left(\frac{1}{v_m}\right)\int_0^{1} k(\hat{r}',\hat{r})\hat{f}_{v,r}{}^{(i)}(\hat{r}')\frac{1}{\hat{r}'^3}d\hat{r}'}$$

(S41)

where i is the iteration index. The initial guess can be selected as the estimated equilibrium distribution. The following choice provides fast and robust convergence for the scheme. The scheme requires only vector operation. Moreover, both over/under-relaxation techniques were tested. Nevertheless, the mentioned scheme is fast and robust enough that relaxation cannot add much to that. The iteration continues until the following convergence criteria (according to the 2-norm) is met as below:

$$\left\|\hat{f}_{v,r}{}^{k+1} - \hat{f}_{v,r}{}^{k}\right\|_2 \leq tol\left\|\hat{f}_{v,r}{}^{1} - \hat{f}_{v,r}{}^{0}\right\|_2 \quad \text{(S42)}$$

4. Iterative scheme to estimate the approximate equilibrium distribution

The following iterative approach (illustrated in Figure S1) is utilized to solve the non-linear set of equations (Eqs 13, 19, and 20) to obtain the values for $s_{est}(\infty)$, $c_{est}(\infty)$, and $\hat{\mu}_r(\infty)$.

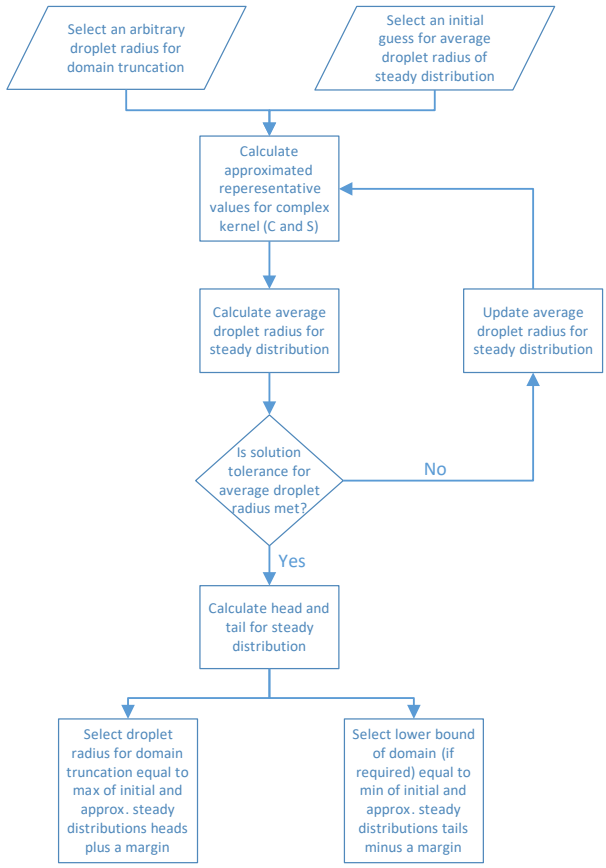

Figure S1: Iterative algorithm to estimate the equilibrium distribution of a complex kernel

The criterion for the convergence is:

$$|\hat{\mu}_r^{old}(\infty) - \hat{\mu}_r^{new}(\infty)| < tolerance \tag{S43}$$

The convergence tolerance is 10^{-6}.

5. Selected polynomials for the internal domain discretization

The internal domain (i.e., droplet size) was discretized using the spectral-element orthogonal collocation technique. Least number of elements of high order is used. This allows proper error decaying properties together with flexibility to handle both wide and narrow DSDs. The Collocation points are chosen based on the roots of the Jacobi polynomials of the order zero (i.e., Legendre polynomials), and quadrature weights are computed for integration accordingly.

References

[1] J. Solsvik, H.A. Jakobsen, The Foundation of the Population Balance Equation: A Review, J. Dispers. Sci. Technol. 36 (2015) 510–520. https://doi.org/10.1080/01932691.2014.909318.

[2] B.J. Benjamin, G. Madras, Analytical solution for a population balance equation with aggregation and fragmentation, Chem. Eng. Sci. 58 (2003) 3049–3051. https://doi.org/10.1016/S0009-2509(03)00159-3.

[3] G. Bhutani, P.R. Brito-Parada, J.J. Cilliers, Polydispersed flow modelling using population balances in an adaptive mesh finite element framework, Comput. Chem. Eng. 87 (2016) 208–225. https://doi.org/10.1016/J.COMPCHEMENG.2016.01.011.

Chapter 4

4. Batch gravity separation (paper II)

This chapter contains the paper-II which was published in "Chemical Engineering Research and Design". In this work, we have developed a population balance model tailored for batch gravity separation processes (the so-called 1D model of dispersion separation). The model encompasses various aspects, including droplets settling / rising due to the gravity force, binary and interfacial coalescence of droplets using a buoyancy-induced film drainage model, and the formation of a homogenous phase. We conducted a comparative analysis of different models for droplet slip velocity, ultimately selecting the one proposed by Kumar and Hartland. Another critical aspect of the model pertains to the mathematical description for the formation of the dense packed layer (DPL). In this study, we introduce a novel approach to enhance the prediction of the DPL formation by introducing an effective diffusion term, resulting in an advection-diffusion equation for the problem. To ensure physical values for the dispersed phase volume fraction within the system, we have proposed a closure model for the effective diffusion coefficient. The model parameters were fine-tuned using experimental data obtained from stabilized water-in-model-oil emulsions, gathered through the NMR technique. These experiments covered a wide range of initial water volume fractions, spanning from 20% to 60%.

Paper II- Moein Assar, Sebastien Charles Roger Simon, Geir Sørland, Brian Arthur Grimes, A theoretical and experimental investigation of batch oil-water gravity separation, Chemical engineering research and design, 194 (2023)136-150.

Available online at www.sciencedirect.com

Chemical Engineering Research and Design

journal homepage: www.elsevier.com/locate/cherd

A theoretical and experimental investigation of batch oil-water gravity separation

*Moein Assar, Sébastien Simon, Geir Humborstad Sørland, Brian Arthur Grimes**

Ugelstad Laboratory, Department of Chemical Engineering, Norwegian University of Science and Technology (NTNU), N-7491 Trondheim, Norway

ARTICLE INFO

Article history:
Received 3 October 2022
Received in revised form 3 April 2023
Accepted 12 April 2023
Available online 14 April 2023

Keywords:
Population balance model
Dense packed layer
Multiphase fluid
Particulate system
Gravity separator

ABSTRACT

Gravity separation of oil-water emulsions is an industrially crucial process. Mechanistic models for a batch separation process can immensely be beneficial by linking emulsion experimental characterization to optimal industrial equipment design. For this reason, a mathematical model for this process was developed, which considers droplets settling/rising due to buoyancy force, binary and interfacial coalescence of the droplets using a film drainage model, and formation of a homophase. Various models for the droplet slip velocity were compared, which exhibit similar predictions using the Kumar and Hartland model and Behzadi et al. model while different from the Zaki and Richardson model. Another crucial part of the model is the proper mathematical description for forming the dense-packed layer (DPL). This study proposes a new approach to improve the prediction for the DPL formation by introducing diffusion in the model as an advection-diffusion equation. Accordingly, a suitable closure model for effective diffusion coefficient was selected, ensuring physical volume fraction range (0–1) in the system. Finally, the proposed closure model was tuned using experimental data for a stabilized water in model oil emulsion. Experiments were performed by the NMR technique for a wide range of initial water volume fractions (20–60%). The model prediction agrees well with the experiments. In particular, simultaneous agreement with all cases having various initial volume fractions and droplet size distributions suggests that this model can be generalized and applied to a wide range of oil and water emulsions. Additionally, the developed model shows promise as it can ensure physical values for volume fractions.

1. Introduction

The separation of oil-water emulsions under the gravitational effect is widely applied in many industries such as food, chemical, petrochemical, and petroleum (Grimes, 2012). Particularly, gravitational separators are ubiquitous in the crude oil industry due to economic reasons and simplicity (Panjwani et al., 2015). The ever-increasing rate of produced water in the existing oil field and the production from heavier crude oil fields are two main aspects that have made this process even more critical. Commonly, emulsions formed in the petroleum industry can be widely diverse regarding behavior and stability. The mentioned fact is attributed to the high dependency on crude oil and water compositions (Oshinowo et al., 2016).

Reviewing the literature, there exists several experimental techniques to measure the dispersed phase volume fraction profiles for sedimentation and creaming processes. Bury et al. (1995) developed a technique based on conductivity measurements. They converted conductivities into volume

* Corresponding author.
E-mail address: brian.a.grimes@ntnu.no (B.A. Grimes).
https://doi.org/10.1016/j.cherd.2023.04.029

Nomenclature

A	gravity settler cross sectional area m^2
B	Hamaker constantNm^2
C	model parameter for effective diffusion coefficient m
C_d	drag coefficient
$C_{d,\infty}$	drag coefficient for a single droplet in an infinitely dilute dispersion
D_e	effective diffusion coefficient m^2s^{-1}
$f_{n,r}$	radius-based number density distribution $m^{-3}m^{-1}$
$f_{v,r}$	radius-based volume density distribution m^{-1}
$\hat{f}_{v,r}$	dimensionless radius-based volume density distribution
$f_{v,r,0}$	initial radius-based volume density distribution m^{-1}
$\hat{f}_{v,r,0}$	initial dimensionless radius-based volume density distribution
$f_{n,v}$	volume-based number density distribution $m^{-3}m^{-3}$
F	volume-fraction hindrance effect coefficient
g	gravitational acceleration ms^{-2}
H	gravity settler height m
H_i	dispersion phase height m
$\hat{H}_i$	dimensionless dispersion phase height
k_B	Boltzmann constant JK^{-1}
k_c	binary coalescence rate m^3s^{-1}
$\hat{k}_c$	dimensionless binary coalescence rate
k_{CE}	empirical tuning parameter for the binary coalescence efficiency
k_{CR}	empirical tuning parameter for the collision rate
k_{IC}	empirical tuning parameter for the interfacial coalescence time
m	model parameter for effective diffusion coefficient
n	model parameter for effective diffusion coefficient
n_{ic}	interfacial convective flux s^{-1}
Pe	droplet Peclet number
Pe_{bc}	droplet pair Peclet number used for binary coalescence
Q_d	volumetric flow rate of the dispersed phase across the interface m^3s^{-1}
r	droplet radius m
$\hat{r}$	dimensionless droplet radius
r_m	largest droplet radius considered for numerical analysis m
$R_{b,n,r}$	coalescence birth rate for radius-based number density $m^{-3}m^{-1}s^{-1}$
$R_{b,n,v}$	coalescence birth rate for volume-based number density $m^{-3}m^{-3}s^{-1}$
$R_{b,v,r}$	coalescence birth rate for radius-based volume density $m^{-1}s^{-1}$
$\hat{R}_{b,v,r}$	dimensionless coalescence birth rate for radius-based volume density
$R_{d,n,r}$	coalescence death rate for radius-based number density $m^{-3}m^{-1}s^{-1}$
$R_{d,n,v}$	coalescence death rate for volume-based number density $m^{-3}m^{-3}s^{-1}$
$R_{d,v,r}$	coalescence death rate for radius-based volume density $m^{-1}s^{-1}$
$\hat{R}_{d,v,r}$	dimensionless coalescence death rate for radius-based volume density
Re	droplet Reynolds number
t	time s
$\hat{t}$	dimensionless time
t_{bc}	binary film drainage and rupture (coalescence) time s
t_{ic}	interfacial film drainage and rupture (coalescence) time s
T	absolute temperature K
u_c	continuous phase velocity ms^{-1}
u_d	dispersed phases settling/rising velocity ms^{-1}
$\hat{u}_d$	dispersed phases dimensionless settling/rising velocity
u_{ic}	equivalent droplet interfacial velocity for a coalescing droplet ms^{-1}
$\hat{u}_{ic}$	equivalent dimensionless droplet interfacial velocity for a coalescing droplet
u_s	slip velocity between continuous and dispersed phases ms^{-1}
u_0	characteristic velocity ms^{-1}
v	droplet volume m^3
v_m	largest droplet volume considered for numerical analysis m^3
V_h	volume of the separated phase m^3
z	spatial coordinate variable m
$\hat{z}$	dimensionless spatial coordinate variable
γ	interfacial tension Nm^{-1}
μ_c	continuous phase viscosity $Nm^{-2}s$
μ_r	average droplet radius m
$\hat{\mu}_r$	dimensionless average droplet radius
ρ_c	continuous phase density kgm^{-3}
ρ_d	dispersed phase density kgm^{-3}
ϕ_d	disperse phase volume fraction
ϕ_m	maximum dispersed phase volume fraction (model parameter for effective diffusion coefficient)
ψ_c	binary droplet coalescence efficiency
ω_c	binary droplet collision rate m^3s^{-1}

fraction values of the dispersed phase in terms of dispersion dielectric theory and showed that the conductivity method is sensitive to small changes in the volume fraction of dispersed phase observed at room temperature. Another powerful technique is based on ultrasonic spectrometry, where the frequency dependence of the ultrasonic attenuation coefficient is measured for an emulsion followed by interpreting the resulting spectra via an ultrasonic scattering theory (Chanamai et al., 1999). Abeynaike et al. (2012) used an optical technique taking advantage of optical contrast between the biodiesel and glycerol and studied sedimentation / creaming of dispersions. Deb et al. (2022) compared two techniques, namely turbidimetry and Raman Spectroscopy, for monitoring a creaming process. They stated that turbidimetry is able to accurately measure the dispersed phase volume fraction off-line while Raman spectroscopy has the potential for in situ monitoring of a creaming system.

Another possible way to characterize emulsions is via a batch gravity separation experiment and monitor the experiments employing the low field nuclear magnetic resonance technique (LF NMR) (Sjöblom et al., 2021). Thereby,

one can quantify various parameters like droplet size distribution (DSD) and dispersed phase volume fraction profiles at different times and in a non-intrusive manner. Here, a predictive model derived from the first principles can help correlate the experimental observations in terms of separation behavior to fundamental understanding about the binary or interfacial coalescence as well as the polydisperse settling/rising of the droplets in the system. In other words, these models allow the characterization of colloidal systems for specific cases through tuning the model parameters. Subsequently, these tuned models can be utilized in the optimal design of oil-water separation equipment.

The batch gravity separation of oil-water dispersions (including creaming and sedimentation processes based on the continuous and dispersed phases) can generally be governed by several mechanisms. Buoyancy-driven transport results in spatial and temporal variations in the density distribution of dispersed droplets. At the same time, pairs of droplets can collide and coalesce, resulting in larger droplets that can sediment/cream faster. A homophase can also be formed (top of column for creaming and bottom for sedimentation). Droplets reaching the liquid-liquid interface can coalesce and integrate with the homophase resulting in its growth and the contraction of the dispersion layer. The rate at which this coalescence takes place can determine the existence of a dense-packed layer (DPL), a packed bed of dispersed phase droplets with a high volume fraction (Panjwani et al., 2015). This layer is formed if the overall rate of interfacial coalescence is lower than that of sedimentation. In this layer, the volume fraction can be extensively increased due to polydispersity and the droplet's tendency to deform under the squeezing force exerted by the weight of the overhead droplets.

Despite the apparent simplicity of the gravity separation process, a fully accommodating model is not available mainly because of the various assumptions and levels of complexity involved in building such models described as follows. Despite these variations, population balance modeling is an indispensable part of such models to consider polydispersity in the system. Wang and Davis (1995) considered simultaneous sedimentation and coalescence according to differential sedimentation of droplets. The assumption of dilute dispersion allowed them to neglect the volume fraction hindrance effect for the settling velocity. They also assumed no resistance to interfacial coalescence. Their model tracks the liquid-liquid interface explicitly via an overall mass balance. Concurrently, the shrinking dispersion layer is implicitly accounted for in their model. Cunha et al. (2008) developed their population balance model according to stokes settling velocity and binary coalescence based on simultaneous differential sedimentation and Brownian motion. They assumed an interfacial coalescence velocity proportional to the height of the dense-packed layer and independent of the droplet size. This was to account for the compression force exerted by the weight of the DPL. They incorporated three tuning parameters for sedimentation velocity as well as binary and interfacial coalescence rates to fit the model to their crude oil-water experiments. In their model, they considered a diffusive term; however, they did not report any function form, numerical value, or physical justification for this term. Their model also lacks consideration for the homophase's growth and contraction of the dispersion layer. Grimes (2012) developed his model according to hindered settling velocity model proposed by Richardson and Zaki (1954) and simultaneous binary and interfacial coalescence according to a film drainage model. He used a temporal-spatial transformation to tackle the moving boundary problem that emerged due to the homophase growth. In a second paper (Grimes et al., 2012), he validated the model versus experimental data. There are more recent attempts to further improve the model. (Antonio García and Fernando Betancourt, 2019) developed their model by adopting different coalescence rates. For the sedimentation zone, they adopted the coalescence model by Rogers and Davis (1990), which is based on differential sedimentation force between droplets. For the DPL, they used the rate proposed by Ruiz and Padilla (1996), which accounts for both droplet size and the compression force from the weight of the DPL. They employed the Kumar and Hartland equation (Kumar and Hartland, 1985) for the droplet slip velocity, which considers both the volume fraction hindrance effect and the non-stokes flow regimes. Additionally, their model contains a correction procedure by turning off the coalescence birth term in case of unphysical values for the volume fractions higher than unity. In their later attempt, they also extended this model to a continuous separator (Antonio García et al., 2022).

The major pitfall with the available modeling approach is the inability of the models to adequately describe the formation and growth of the DPL. This shortcoming originally stems from the oversimplification concerning the droplet velocities. In this modeling approach, an empirical terminal velocity model for the droplets is usually used instead of directly solving the continuity and momentum equations for continuous and dispersed phases. This simplification can result in unphysical volume fraction predictions, even outside the physical bound of 0–1. As described, various modeling and numerical strategies were adopted by different researchers to address this challenge. Another approach in the modeling is combining the population balance equation and CFD (PBE-CFD) using available CFD software packages. This will allow the simultaneous solution of the continuity and motion equations for a polydispersed system. Panjwani et al. (2015) used this approach to study the formation of the DPL for a continuous separator. They mentioned in their study that direct modeling of the DPL can be practically restrictive due to the immense span of time and length scales associated with different underlying physics. Oshinowo et al. (2016), in their PBE-CFD model for batch separation, used a multi-fluid Eulerian multiphase approach. They compared their model results versus experimental data obtained by the ultrasonic technique. In their later work (Oshinowo and Vilagines, 2020), they extended their model to simulate a 3-phase separator. From the studied literature, the main challenges with the CFD-PBE approach are the inadequacy of the prediction for the DPL and, at the same time, complexity and expensive computation, which can limit its application for ordinary engineering tasks such as model tuning, and optimization.

In the current study, we aim to improve and extend the previous model by Grimes (2012). The focus of this work would be primarily on improving the prediction for the DPL formation. The main motivation for the current modeling effort is the early works done by Shih et al. (1987, 1986) where they showed that a one-dimensional hydrodynamic model for the sedimentation of the fine particles could be simplified in the form of a diffusion-type equation. In the current work, we propose an advection-diffusion model for batch

sedimentation of oil-water emulsion with a suitable closure model for effective diffusion coefficient. The parameters for this closure model are estimated according to the experiments performed by the LF NMR technique for batch sedimentation of a stabilized model oil. It is worth mentioning that the coalescence models are presented in this work only to keep the generality of the model and these phenomena will be experimentally studied in future works.

2. Mathematical analysis

Theoretically, the gravity separation process for an oil-water dispersion consists of hindered settling/rising of the droplets as well as coalescence of the droplets. Eventually, as the droplets reach the oil-water interface, a homophase can be created and grow due to the interfacial coalescence. The latter phenomenon gives rise to a water phase formation on the bottom for a sedimentation system or an oil phase formation on the top for a creaming system. Suppose the rate of sedimentation is higher than the rate of interfacial coalescence. In that case, one can expect the formation of a DPL on top/bottom of the liquid-liquid interface that initially grows in thickness as more droplets move toward the interface; eventually, this layer can start to shrink as the droplets coalesce into the homophase.

2.1. Dispersion layer model

We consider an initially uniform coalescing dispersion that is under the influence of gravity. Here, the presented model is general and applicable to sedimentation and creaming systems. The only difference is the coordinate origin and the axis direction, which should be along with the settling or rising movement, as depicted in Fig. 1. For a sedimentation system, the origin of the coordinate system is at the top, and the z-axis extends from top to bottom in the direction of droplet sedimentation. For a creaming system, the origin is at the bottom, and the positive z-direction is selected from the bottom to the top.

The mass balance equation for the dispersed phase by considering the advection and diffusion terms takes the following form:

$$\frac{\partial f_{n,r}(r,z,t)}{\partial t} = -\frac{\partial}{\partial z}[u_d(r,z,t)f_{n,r}(r,z,t)] + \frac{\partial}{\partial z}\left(D_e(r,z,t)\frac{\partial f_{n,r}(r,z,t)}{\partial z}\right) + R_{b,n,r} - R_{d,n,r} \quad (1)$$

where $f_{n,r}$ is the radius-based number density distribution for a specific droplet size at a particular column location and time. u_d is the pertinent droplet rising/settling velocity. D_e is the effective diffusion coefficient. $R_{b,n,r}$ and $R_{d,n,r}$ are radius-based birth and death rates consistent with the number density distribution resulting from the binary droplet coalescence, respectively. r, z, t are droplet radius, vertical location in the separation column, and elapsed time from the start of the process, respectively. It must be noted that the diffusion term is added to the model to consider the effect of compressive stress in the DPL based on the insight from the work of Shih et al. (1987, 1986). This matter will be further expanded and discussed in Section 2.4. The radius-based coalescence birth and death rates in Eq. (1) are as follows:

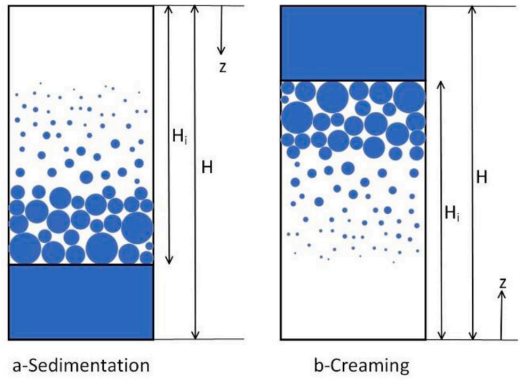

Fig. 1 – Schematic of batch gravity separator, a-sedimentation, b-creaming.

$$R_{b,n,r} = \int_0^{r/\sqrt[3]{2}} k_c(r', r'', z, t) f_{n,r}(r', z, t) f_{n,r}(r'', z, t) \frac{r^2}{r'^2} dr' \quad (2)$$

$$R_{d,n,r} = f_{n,r}(r, z, t) \int_0^{\infty} k_c(r', r'', z, t) f_{n,r}(r', z, t)\, dr' \quad (3)$$

where k_c is the coalescence rate between droplets of sizes υ and υ'. The interested reader can also refer to the supplementary material for more details about the derivation of this form of PBE. Now, we take another step and change the dependent variable from the number density distribution to the volume density distribution. It is worth noting that in the latter definition, the dependent variable has a more limited range of numerical values. As a result, one can expect lower round-off error issues in the numerical analysis of the problem. Also, the visualization of the results is strengthened. The Volume density distribution is simply defined as below:

$$f_{v,r}(r,z,t) = f_{n,r}(r,z,t) \times \frac{4\pi}{3} r^3 \quad (4)$$

With the above transformation, the governing equation takes the following form.

$$\frac{\partial f_{v,r}(r,z,t)}{\partial t} = -\frac{\partial}{\partial z}[u_d(r,z,t)f_{v,r}(r,z,t)] + \frac{\partial}{\partial z}\left(D_e(r,z,t)\frac{\partial f_{v,r}(r,z,t)}{\partial z}\right) + R_{b,v,r} - R_{d,v,r} \quad (5)$$

$$R_{b,v,r} = \left(\frac{3}{4\pi}\right) r^3 \int_0^{\frac{r}{\sqrt[3]{2}}} \frac{k_c(r', r'', z, t) f_{v,r}(r', z, t) f_{v,r}(r'', z, t)}{r'^3 (r^3 - r'^3)} \frac{r^2}{r''^2} dr' \quad (6)$$

$$R_{d,v,r} = \left(\frac{3}{4\pi}\right) f_{v,r}(r, z, t) \int_0^{\infty} k_c(r', r'', z, t) \frac{f_{v,r}(r', z, t)}{r'^3} dr' \quad (7)$$

Following the mentioned definition, the volume fraction and average droplet size can be calculated now utilizing the below integrals:

$$\phi_d(z,t) = \int_0^{\infty} f_{v,r}(r,z,t)\, dr \quad (8)$$

$$\mu_r(z,t) = \frac{1}{\phi_d(z,t)} \int_0^{\infty} r f_{v,r}(r,z,t)\, dr \quad (9)$$

where ϕ_d and μ_r are dispersed phase volume fraction and average droplet radius, respectively.

In the derived model, the droplet size coordinate expands from zero to infinity. Thus, the coordinate should be truncated at a suitable value (r_m) to promote the numerical analysis of the problem. The choice of the mentioned value is critical for generating valid numerical results. A feasible approach for properly selecting the truncation point for the internal coordinate is developed and used to choose this value conservatively for both coalescing and non-coalescing systems in the supplementary material. The above advection-diffusion equation is subject to the below boundary conditions:

- At $z = 0$ (top or bottom), overall flux is equal to zero
- At $z = H_i$ (interface), overall flux should be calculated according to the interfacial coalescence

The above boundary conditions ensure that the model is thoroughly conservative. These boundary conditions can be mathematically expressed as:

$$u_d(r, z, t) f_{v,r}(r, z, t) - D_e(r, z, t) \frac{\partial f_{v,r}(r, z, t)}{\partial z} = 0 \text{ at } z = 0, \ \forall t|_{0 < t \le \infty} \ \& \ r|_{0 \le r \le \infty} \quad (10)$$

$$u_d(r, z, t) f_{v,r}(r, z, t) - D_e(r, z, t) \frac{\partial f_{v,r}(r, z, t)}{\partial z} = u_{ic}(r, t) f_{v,r}(r, z, t) \text{ at } z = H_i, \ \forall t|_{0 < t \le \infty} \ \& \ r|_{0 \le r \le \infty} \quad (11)$$

where u_{ic} is the velocity at which the droplet leaves the dispersed phase by coalescing into the homophase and will be further expanded in Section 2.2. The initial condition for an initially uniform system is as below:

$$f_{v,r}(r, z, t) = f_{v,r,0}(r) \text{ at } t = 0, \ \forall z|_{0 < z < H_i} \ \& \ r|_{0 \le r \le \infty} \quad (12)$$

2.2. Moving interface model

As described previously, as the dispersed phase gets separated, a new homophase is formed at the bottom/top of the batch separator column. The convective flux for a specific droplet size at the interface can be written as below:

$$n_{ic}(r, H_i, t) = u_{ic}(r, t) f_{v,r}(r, H_i, t) \quad (13)$$

where u_{ic} is the velocity at which the droplet leaves the dispersed phase by coalescing into the homophase. This velocity can be calculated as below:

$$u_{ic}(r, t) = \frac{4r}{3t_{ic}(r, t)} \quad (14)$$

The interested reader can refer to the supplementary material section for details regarding the derivation of Eq. (14). Here, t_{ic} is the interfacial coalescence time for a droplet of size r from getting in contact with the dispersion-homophase interface until fully integrated with the homophase. This term will be further expanded using a parallel film drainage model in Section 2.5. Now, using the following term (Eq. (14)), the total volumetric flow rate of the dispersed phase over the interface can be calculated as:

$$Q_d = A \int_0^\infty u_{ic}(r, t) f_{v,r}(r, H_i, t) dr \quad (15)$$

where A is the cross-section of the column. Now, this term can be exploited to calculate the dynamic change in the location of the interface. For that, one can equate the volume change rate for the homophase with this term as below.

$$\frac{dV_h(t)}{dt} = Q_d \quad (16)$$

where V_h is the total volume of the separated homophase and can be written as:

$$V_h = A(H - H_i) \quad (17)$$

By substitution, the final equation for the dynamic change in the interface location yields as:

$$\frac{dH_i(t)}{dt} = -\int_0^\infty u_{ic}(r, t) f_{v,r}(r, H_i, t) dr \quad (18)$$

The initial condition for Eq. (18) can be written as below.

$$H_i(t) = H \text{ at } t = 0 \quad (19)$$

2.3. Droplet rising/settling velocity

Droplets settle or rise according to the buoyancy force for a dispersion system under the influence of gravity. Bearing that the colloidal droplets move slowly, practically, it is a safe assumption to ignore the inertia terms in the momentum equation (Shih et al., 1986). Based on this assumption, the velocity difference between the continuous and dispersed phases ($u_d - u_c$) becomes equal to the slip velocity, which has the functionality of the droplet size as well as dispersed phase volume fraction as below:

$$u_d(r, z, t) - u_c(z, t) = u_s(r, \phi_d) \quad (20)$$

Simultaneously, while droplets are moving, the volumetric change should be replaced by the continuous phase. The continuity equation expresses this matter as below:

$$(1 - \phi_d) u_c(z, t) + \int_0^\infty f_{v,r}(r, z, t) u_d(r, z, t) dr = 0 \quad (21)$$

Slip velocity can be further formulated by considering buoyancy, weight, and drag forces as:

$$u_s(r, \phi_d) = \sqrt{\frac{8gr}{3C_d} \frac{|\rho_d - \rho_c|}{\rho_c}} \quad (22)$$

where g is the gravitational acceleration, ρ_c and ρ_d are continuous and dispersed phase densities, and C_d is the drag coefficient. Behzadi et al. (2004) defined the drag coefficient as the product of the drag coefficient for a single droplet/bubble in an infinitely dilute dispersion ($C_{d,\infty}$) and the volume hindrance effect coefficient (F).

$$C_d(r, \phi_d) = C_{d,\infty}(r) F(\phi_d) \quad (23)$$

They proposed an empirical correlation for the latter functionality for both droplets and bubbles for a wide range of volume fractions (up to 75%). Accordingly, they proposed the following equation for this coefficient:

$$F(\phi_d) = \exp(3.64\phi_d) + \phi_d^{0.864} \quad (24)$$

Alternatively, the hindrance effect coefficient can be calculated based on the equation by Richardson and Zaki (1954) as below:

$$F(\phi_d) = \frac{1}{(1 - \phi_d)^n} \quad (25)$$

The drag coefficient for a single droplet in an infinitely dilute dispersion ($C_{d,\infty}$) can be calculated using the well-known Schiller–Naumann correlation (Shiller and Naumann, 1935) which applies to Reynolds numbers less than 1000.

$$C_{d,\infty}(r) = \frac{24}{\mathrm{Re}(r)} (1 + 0.15\,\mathrm{Re}(r)^{0.687}) \quad (26)$$

Here, the Reynolds number is defined as:

$$\mathrm{Re}(r) = \frac{2\rho_c u_s r}{\mu_c} \tag{27}$$

where μ_c is the continuous phase dynamic viscosity. It is worth noting that in case of the creeping flow regime ($\mathrm{Re} \ll 1$), the slip velocity can be explicitly expressed by the stokes terminal velocity as below:

$$u_s(r, \phi_d) = \frac{2gr^2}{9\mu_c F(\phi_d)} |\rho_d - \rho_c| \tag{28}$$

Another useful empirical equation to calculate the slip velocity is proposed by Kumar and Hartland (1985). It is particularly advantageous as it is valid over a wide range of volume fractions and Reynolds numbers ($\phi_d = 0.01 - 0.76$ and $\mathrm{Re} = 0.16 - 3169$).

$$0.53{u_s}^2 + \frac{12\mu_c}{r\rho_c}u_s + \frac{2rg(\rho_c - \rho_d)(1-\phi_d)}{3\rho_c(1 + 4.56{\phi_d}^{0.73})} = 0 \tag{29}$$

The slip velocity can be directly calculated by solving the above quadratic polynomial. Now having the slip velocity's numerical value, one can use the momentum and continuity equation (Eqs. (20) and (21)) to calculate the continuous and all the dispersed phase droplets' velocities. Zimmels (1983) has proposed a numerical approach for the mentioned problem. However, this model could not describe our experimental observations, specifically the sharp sedimentation fronts formed during the sedimentation. Thus, we adopted another approach in which the movement effect of the continuous phase in the opposite direction is compensated by multiplying the slip velocity by the continuous phase volume fraction to yield the dispersed phase droplet velocity. According to this assumption, the system is treated similar to a monodispersed system.

$$u_d(r, z, t) = (1 - \phi_d(z, t))u_s(r, \phi_d) \tag{30}$$

2.4. Effective diffusion

Shih et al. (1987, 1986) showed that hyperbolic governing equations for a one-dimensional sedimentation system could be transformed into a diffusion-type equation by ignoring the acceleration terms (owing to the low velocity of the droplets). This approach offers a more straightforward numerical treatment for the governing equations. According to this insight, we added a diffusive term to the governing equation for the dispersion phase. In this section, we propose a closure model for this effective diffusion coefficient initially introduced into the equation. This effective diffusion coefficient is basically the ratio of elasticity to a drag term in the packed region (Shih et al., 1986). For the DPL, elasticity is determined by the compressive stress modulus which has a strong functionality of the volume fraction (Shih et al., 1986). The drag term has the functionalities of physicochemical properties like phase density difference, droplet velocity, as well as volume fraction. The other phenomenon that needs to be addressed by this closure model is the maximum volume fraction in the DPL due to the physical restriction. Rather than selecting one for this value, we introduce the maximum volume fraction allowed in the system (ϕ_m) similar to other researchers work on the emulsion viscosity (Ishii and Zuber, 1979; Krieger and Dougherty, 1959; Mills, 1985). The mentioned parameter allows better tuning according to the experimental data. For a monodispersed system with rigid spheres, packing is $\pi/6 = 0.5236$ (Antonio García and Fernando Betancourt, 2019); however, as a consequence of droplet deformation and polydispersity in liquid-liquid dispersion systems, this value can be higher (typically 0.7–0.9). Additionally, the closure model should satisfy the below two constraints:

- Zero effective diffusion at zero volume fraction
- Infinite effective diffusion at maximum volume fraction

The first constraint is deducted from the fact that in infinitely dilute dispersions, the compressive stress modules and thus the effective diffusion coefficient is zero. The latter constraint is vital as the physical restriction due to high volume fraction can be mathematically described by infinite diffusion. Under these circumstances, all excess droplets at a region with a volume fraction close to ϕ_m will immediately diffuse back to the surrounding regions with a lower volume fraction. This way, the balance equation is forced to conserve the volume fraction between 0-ϕ_m since the effective diffusion goes asymptotically toward infinity as the volume fraction approaches the maximum volume fraction in the system.

In this study, we consider the droplet velocity and volume fraction functionalities as the main parameters for this effective diffusion coefficient. The following function meets the constraints described above, provided that the exponent n and m are positive.

$$D_e(r, z, t) = Cu_d(r, \phi_d)\left(\frac{(\phi_d(z, t)/\phi_m)^n}{(1 - \phi_d(z, t)/\phi_m)^m}\right) \tag{31}$$

where C is the model constant for a specific system and has the dimension of length. n and m are dimensionless exponents for the model. It is worth mentioning that droplet velocity appeared in the equation by assuming that the Stokes flow regime prevails in the DPL.

2.5. Coalescence model

Similar to the work of Grimes (2012), a parallel film drainage model is utilized in the current work. Here, only the equations for the coalescence rates are presented, and the interested reader is referred to mentioned paper for more details about underlying assumptions and derivations. Accordingly, the binary coalescence rate is defined as the product of collision frequency (ω_c) and coalescence efficiency (ψ_c).

$$k_c(r, r', z, t) = \omega_c(r, r', z, t)\psi_c(r, r', z, t) \tag{32}$$

The radius-based equation for collision frequency takes the following form.

$$\omega_c(r, r', z, t) = k_{CR}\frac{k_B T}{6\mu_c}\frac{(r + r')^2}{rr'}[1 + Pe_{bc}(r, r', z, t) + 4.496 (Pe_{bc}(r, r', z, t))^{1/3}] \tag{33}$$

where k_B is the Boltzmann constant, T is absolute temperature, and k_{CR} is the model tuning parameter. Droplet pair Peclet number (Pe_{bc}) is defined as below:

$$Pe_{bc}(r, r', z, t) = \frac{4\pi}{3}\frac{(\rho_d - \rho_c)g}{k_B T}F(\phi_d)rr'|r^2 - r'^2| \tag{34}$$

The radius-based coalescence efficiency can be calculated using the following equation.

$$\psi_c(r, r', z, t) = \exp\left(-\frac{1}{k_{CE}} t_{bc}(r, r', z, t)\right) \tag{35}$$

where k_{CE} is the model tuning parameter and t_{bc} is the binary coalescence time expressed by the following equation.

$$t_{bc}(r, r', z, t) = 1.046 \frac{\mu_c(\rho_d - \rho_c)g}{\gamma^{\frac{3}{2}} B^{\frac{1}{2}}} \left[\frac{rr'}{r + r'}\right]^{9/2} \tag{36}$$

where γ is interfacial tension and B is the Hamaker constant.

According to Eq. (14), the interfacial coalescence time function (t_{ic}) can be determined using the following formula to calculate the interfacial coalescence velocity.

$$t_{ic}(r, z, t) = \frac{1.046}{k_{IC}} \frac{\mu_c(\rho_d - \rho_c)g}{\gamma^{\frac{3}{2}} B^{\frac{1}{2}}} r^{9/2} \tag{37}$$

where k_{IC} is the model tuning parameter. In the presented model, only the buoyancy force is included as the squeezing force to calculate the coalescence efficiency. However, it is still possible to derive similar coalescence rates by considering the compressive force in the DPL. Nevertheless, it is not the focus of the current work and will be considered in a future work.

2.6. Dimensionless formulation and treating the moving boundary

The dimensionless form of the governing equations is adopted to analyze the problem numerically. This dimensionless formulation allows immobilization of the moving boundary at the interface, which can be computed on a fixed numerical grid. Thus, all the variables are made dimensionless through the characteristic scales using the following definitions: characteristic length scale as the height of the column (H), characteristic droplet size scale as the maximum droplet size in which the internal domain is truncated (v_m, r_m), the characteristic time scale is calculated by dividing the height of column (H) by a characteristic velocity (u_0) which is the stokes velocity for an initial average droplet size. Using the mentioned scales, all the independent variables can be made dimensionless as follows.

$$\hat{t} = \frac{u_0}{H} t \tag{38}$$

$$\hat{z} = \frac{z}{H_i(t)} = \frac{z}{H\hat{H}_i} \tag{39}$$

$$\hat{r} = \frac{r}{r_m} \tag{40}$$

The dependent variables are made dimensionless using the below definitions.

$$\hat{H}_i(\hat{t}) = \frac{H_i(t)}{H} \tag{41}$$

$$\hat{f}_{v,r}(\hat{r}, \hat{z}, \hat{t}) = f_{v,r}(r, z, t) r_m \tag{42}$$

$$\hat{u}_d(\hat{r}, \hat{z}, \hat{t}) = \frac{u_d(r, z, t)}{u_0} \tag{43}$$

$$Pe(\hat{r}, \hat{z}, \hat{t}) = \frac{u_0 H}{D_e(r, z, t)} \tag{44}$$

$$\hat{k}_c(\hat{r}', \hat{r}'', \hat{z}, \hat{t}) = \frac{H k_c(r', r'', z, t)}{u_0 v_m} \tag{45}$$

$$\hat{u}_{ic}(\hat{r}, \hat{t}) = \frac{u_{ic}(r, t)}{u_0} \tag{46}$$

It must be noted that the new dimensionless independent variable $\hat{z}$ now has the dependency of both time t and spatial coordinate z. As a result, the time derivative $\partial/\partial t$ should be written as a directional derivative in the new dimensionless frame of reference (Grimes, 2012); therefore, it reads as:

$$\frac{\partial f_{v,r}}{\partial t} = \left(\frac{\partial \hat{t}}{\partial t}\right)\left(\frac{\partial \hat{f}_{v,r}}{\partial \hat{t}}\right)\left(\frac{\partial f_{v,r}}{\partial \hat{f}_{v,r}}\right) + \left(\frac{\partial \hat{z}}{\partial t}\right)\left(\frac{\partial \hat{f}_{v,r}}{\partial \hat{z}}\right)\left(\frac{\partial f_{v,r}}{\partial \hat{f}_{v,r}}\right) \tag{47}$$

The partial derivatives in Eq. (47) can be expanded further using the chain rule of differentiation. By doing that and further simplifications, the following equation is obtained.

$$\frac{\partial f_{v,r}}{\partial t} = \left(\frac{u_0}{r_m H}\right)\frac{\partial \hat{f}_{v,r}}{\partial \hat{t}} - \left(\frac{u_0}{r_m H}\right)\left(\frac{\hat{z}}{\hat{H}_i}\right)\left(\frac{\partial \hat{H}_i}{\partial \hat{t}}\right)\frac{\partial \hat{f}_{v,r}}{\partial \hat{z}} \tag{48}$$

Similarly, the convective and diffusive terms can be obtained in the new spatially curvilinear coordinate using the chain rule of differentiation as:

$$\frac{\partial}{\partial z}(u_d f_{v,r}) = \left(\frac{u_0}{r_m H \hat{H}_i}\right)\frac{\partial}{\partial \hat{z}}(\hat{u}_d \hat{f}_{v,r}) \tag{49}$$

$$\frac{\partial f_{v,r}}{\partial z} = \left(\frac{1}{r_m H \hat{H}_i}\right)\frac{\partial \hat{f}_{v,r}}{\partial \hat{z}} \tag{50}$$

$$\frac{\partial}{\partial z}\left(D\frac{\partial f_{v,r}}{\partial z}\right) = \left(\frac{u_0}{r_m H \hat{H}_i^2}\right)\frac{\partial}{\partial \hat{z}}\left(\frac{1}{Pe}\frac{\partial \hat{f}_{v,r}}{\partial \hat{z}}\right) \tag{51}$$

The described approach immobilizes the moving boundary, thereby making the z-coordinate (0-H_i(t)) into the new dimensionless coordinate (0–1). Consequently, the equation can now be more conveniently treated numerically as the numerical grid for the spatial dimension is now fixed relative to the position of the interface, H_i. The final equation can be obtained by substituting the derived terms into Eq. (5) as:

$$\begin{aligned}\frac{\partial \hat{f}_{v,r}(\hat{r}, \hat{z}, \hat{t})}{\partial \hat{t}} = {} & \left(\frac{\hat{z}}{\hat{H}_i(\hat{t})}\right)\left(\frac{\partial \hat{H}_i(\hat{t})}{\partial \hat{t}}\right)\frac{\partial \hat{f}_{v,r}(\hat{r}, \hat{z}, \hat{t})}{\partial \hat{z}} \\ & - \left(\frac{1}{\hat{H}_i(\hat{t})}\right)\frac{\partial}{\partial \hat{z}}(\hat{u}_d(\hat{r}, \hat{z}, \hat{t})\hat{f}_{v,r}(\hat{r}, \hat{z}, \hat{t})) + \left(\frac{1}{\hat{H}_i^2(\hat{t})}\right)\frac{\partial}{\partial \hat{z}} \\ & \left(\frac{1}{Pe(\hat{r}, \hat{z}, \hat{t})}\frac{\partial \hat{f}_{v,r}(\hat{r}, \hat{z}, \hat{t})}{\partial \hat{z}}\right) + \hat{R}_{b,v,r} - \hat{R}_{d,v,r}\end{aligned} \tag{52}$$

where dimensionless birth and death rates are:

$$\hat{R}_{b,v,r} = \hat{r}^3 \int_0^{\frac{\hat{r}}{\sqrt[3]{2}}} \frac{\hat{k}_c(\hat{r}', \hat{r}'', \hat{z}, \hat{t})\hat{f}_{v,r}(\hat{r}', \hat{z}, \hat{t})\hat{f}_{v,r}(\hat{r}'', \hat{z}, \hat{t})}{\hat{r}'^3(\hat{r}^3 - \hat{r}'^3)} \frac{\hat{r}^2}{\hat{r}''^2} d\hat{r}' \tag{53}$$

$$\hat{R}_{d,v,r} = \hat{f}_{v,r}(\hat{r}, \hat{z}, \hat{t}) \int_0^1 \hat{k}_c(\hat{r}', \hat{r}'', \hat{z}, \hat{t}) \frac{\hat{f}_{v,r}(\hat{r}', \hat{z}, \hat{t})}{\hat{r}'^3} d\hat{r}' \tag{54}$$

Similarly, the equation for the moving interface turns into the following form.

$$\frac{d\hat{H}_i(\hat{t})}{d\hat{t}} = -\int_0^1 \hat{u}_{ic}(\hat{r}, \hat{t})\hat{f}_{v,r}(\hat{r}, 1, \hat{t}) d\hat{r} \tag{55}$$

Eqs. (52) and (55) should be solved subject to the following boundary and initial conditions:

$$\hat{u}_d(\hat{r},\hat{z},\hat{t})\hat{f}_{v,r}(\hat{r},\hat{z},\hat{t}) - \frac{1}{\hat{H}_i(\hat{t})Pe(\hat{r},\hat{z},\hat{t})}\frac{\partial \hat{f}_{v,r}(\hat{r},\hat{z},\hat{t})}{\partial \hat{z}} = 0 \; at \; \hat{z} = 0, \; \forall \; \hat{t}\,|_{0<\hat{t}\leq\infty} \; \& \; \hat{r}\,|_{0\leq\hat{r}\leq 1} \quad (56)$$

$$\hat{u}_d(\hat{r},\hat{z},\hat{t})\hat{f}_{v,r}(\hat{r},\hat{z},\hat{t}) - \frac{1}{\hat{H}_i(\hat{t})Pe(\hat{r},\hat{z},\hat{t})}\frac{\partial \hat{f}_{v,r}(\hat{r},\hat{z},\hat{t})}{\partial \hat{z}} = \hat{u}_{ic}(\hat{r},\hat{t})\hat{f}_{v,r}(\hat{r},\hat{z},\hat{t}) \; at \; \hat{z} = 1, \; \forall \; \hat{t}\,|_{0<\hat{t}\leq\infty} \; \& \; \hat{r}\,|_{0\leq\hat{r}\leq 1} \quad (57)$$

$$\hat{f}_{v,r}(\hat{r},\hat{z},\hat{t}) = \hat{f}_{v,r,0}(\hat{r}) \; at \; \hat{t} = 0, \; \forall \; \hat{z}\,|_{0<\hat{z}<1} \; \& \; \hat{r}\,|_{0\leq\hat{r}\leq 1} \quad (58)$$

$$\hat{H}_i(\hat{t}) = 1 \; at \; \hat{t} = 0 \quad (59)$$

In the new dimensionless form, the volume density and dimensionless average droplet size can be calculated as follows.

$$\phi_d(\hat{z},\hat{t}) = \int_0^1 \hat{f}_{v,r}(\hat{r},\hat{z},\hat{t})\,d\hat{r} \quad (60)$$

$$\hat{\mu}_r(\hat{z},\hat{t}) = \frac{1}{\phi_d(\hat{z},\hat{t})}\int_0^1 \hat{r}\hat{f}_{v,r}(\hat{r},\hat{z},\hat{t})\,d\hat{r} \quad (61)$$

3. Numerical analysis

The orthogonal collocation technique (Villadsen and Michelsen, 1978) was used in an element-based form to discretize the internal domain (droplet size). Four and five elements were selected for the non-coalescing and coalescing cases, respectively. The same number of collocation points were adopted for boundary and central elements. The details of the grid generation and the truncation of the internal domain can be found in the supplementary material.

The finite volume method (FVM) with equidistance cells was applied for the spatial direction. MUSCL technique (Anderson et al., 2020) was utilized to discretize the advection terms (including the 1st term at the right-hand side of Eq. (52) that appeared due to the transformation) in order to avoid unphysical oscillatory results due to the strong advection terms. This technique is based on linear profile reconstruction together with slope limiting and subsequent application of the upwind scheme. The described method provides 1st order accuracy for extrema and 2nd order elsewhere. Central differencing was applied to compute the diffusive term. The detail of the FVM technique used is available in the supplementary material.

The discretized governing equation for the dispersion layer (Eq. (52)) by the abovementioned techniques forms a system of ordinary differential equations (ODEs) which were time-integrated together with the transient equation for the moving interface (Eq. (55)). The adaptive Gear's backward differentiation scheme (Gear, 1971) was used to solve the mentioned systems of ODEs.

4. Experimental section

4.1. Chemicals

The following chemicals were used to prepare emulsions: The aqueous phase was composed of 0.1 M of sodium chloride (for analysis, Merck) dissolved in water obtained from a Milli-Q system (Millipore). The model oil phase was prepared by dissolving 800 ppm of Span 80 (Sorbitan monooleate, Fluka) in a solvent composed of 80% wt. Primol 352 (Brenntag Nordic A/S) and 20% wt. decane (Sigma-Aldrich, ReagentPlus ≥99%). The solvent composition was adjusted to obtain viscosity which is high enough to separate the signals for the oil and aqueous phase by NMR. The viscosities and the densities of the oil and aqueous phases are given in Table 1.

4.2. Emulsion preparation

The aqueous phase and then the oil phase (total volume: 30 mL) were introduced into a 60 mL tube. Then the mixture was stirred at 1500 rpm for 3 min using a 4 blades-propeller. Approximately 4.0 mL of the emulsion was then pipetted and introduced into an NMR tube.

4.3. NMR measurements

The measurements were done with a 21 MHz NMR apparatus from Anvendt Teknologi AS (Trondheim, Norway). The sedimentation column was a flat bottom tube with a diameter of 17 mm. The temperature of the sample was maintained at 25 °C by an air-controlled system. The NMR was linked to a PC and controlled via in-house programs developed by Anvendt Teknologi AS. The following physical parameters were obtained:

- Position-dependent water concentration profiles (brine profiles) using a sequence based on previous publications (Hjartnes et al., 2019; Simon et al., 2011; Sjöblom et al., 2021; Sørland, 2014). First the water phase signal was separated from the oil signal using their difference in longitudinal relaxation times (T1). Consequently, a stimulated echo (STE) sequence was applied prior to the profile acquisition, and the z-storage delay in the STE was set to 2.5 s. The profiles were measured every 30 s for 1 h.
- Droplet size distribution (DSD). The sequence starts by only recording the water signal, as explained above. Then, the droplet size distribution is determined by applying the Pulsed Field Gradient (PFG) NMR technique. In this approach, the average surface-to-volume ratio (S/V) of droplets is determined from the apparent restricted diffusion coefficient of water inside droplets measured at a given observation time, while the distribution is assessed from the T2 relaxation time of water as previously described (Sjöblom et al., 2021; Van Der Tuuk Opedal et al., 2009). It must be noticed that Van Der Tuuk Opedal et al. (2009) have compared the DSD distribution obtained by NMR and by another technique (microscopy), and they found a good correlation between the two DSD distributions. However, as the droplets are larger than in previous works (diameter higher than 20 µm), long observation times are required, which may lead to artifacts from the movement of the droplets themselves. Consequently, the average S/V ratio

Table 1 – Viscosity and features of the oil and aqueous phases used to prepare emulsions.

Solvent	Viscosity @ 25 °C (Pa·s) *	Density @ 25 °C (kg/m3) **
NaCl 0.1 M	Not measured	1001.3
Primol 352/decane 80/20 wt%	21.1×10^{-3}	830.9

*: Measured with a Physica MCR 301.
**: Measured with a densitymeter Anton Paar DMA 5000 M.

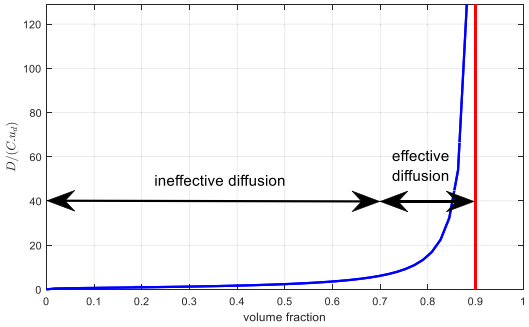

Fig. 2 – Fitted effective diffusion coefficient.

was measured at two different observation times and extrapolated to 0 observation time.

5. Results and discussion

5.1. *Effective diffusion model parameter estimation*

The parameters in the proposed effective diffusion model were estimated by comparing the model predictions with the experimental data for the water in stabilized model oil emulsion described in Section 4. Every experiment (DSD and brine profile measurements) has been performed twice and the results are reproducible. Three initial volume fractions for the emulsions were studied, namely 20%, 40%, and 60%. The model parameters were estimated by simultaneous minimization of the average absolute relative deviation (AARD) for all the data sets as the objective function using MATLAB unconstrained nonlinear optimization functionality (*fminunc*). The deviation was defined as the difference between the measured volume fraction at a spatial location and time, and the model prediction for the whole studied cases. The empirical equation proposed by Kumar and Hartland (Kumar and Hartland, 1985) was used as the slip velocity model (Eq. (29)). This issue is discussed in more detail in Section 5.2. In this study, since the three DSDs depict very similar properties in terms of polydispersity, the maximum volume fraction parameter (ϕ_m) was selected as 0.9, supported by the experimental data. However, as mentioned in Section 2.4, this parameter depends on two main factors, namely, polydispersity (how wide the distribution is and can be expressed by the standard deviation of the DSD) and deformation (which depends on the compressive force in the DPL) and, further modeling of this parameter would be an interesting future study, which might need more experimental cases with more variations in the DSDs. The estimated values for the effective diffusion model parameters are: $C = 5.1 \times 10^{-4} m$, $n = 0.23$, and $m = 1.29$. The volume fraction functionality of effective diffusion coefficient is depicted in Fig. 2.

In Fig. 2, the y-axis shows the relative significance of the diffusion to the advection. Accordingly, we can identify two main regions:

- dispersed phase volume fraction between 0% and 70% with strong advection term and insignificant diffusion term, which can be practically neglected.
- dispersed phase volume fraction between 70% and 90%, in which the diffusion term becomes increasingly more dominant in the governing equation as the volume fraction increases.

As the volume fraction approaches the maximum volume fraction specified in the model (ϕ_m), the diffusion flux asymptotically approaches infinity in the system. The described issue ensures that the dispersed phase volume fraction remains in the physical range (0-ϕ_m). This occurs as the droplets in high-volume fraction regions rapidly diffuse to the surrounding areas with low-volume fractions.

5.2. *Comparison of the slip velocity models*

The three different presented models for the slip velocities in Section 2.3 are compared in Fig. 3 for the case of 40% initial water volume fraction.

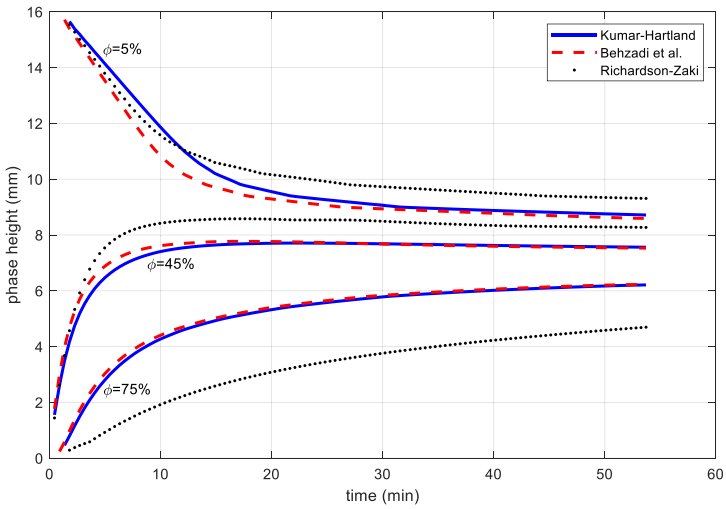

Fig. 3 – Comparison of results of different slip velocity models for water iso-volume fraction curves (initial volume fraction=40%).

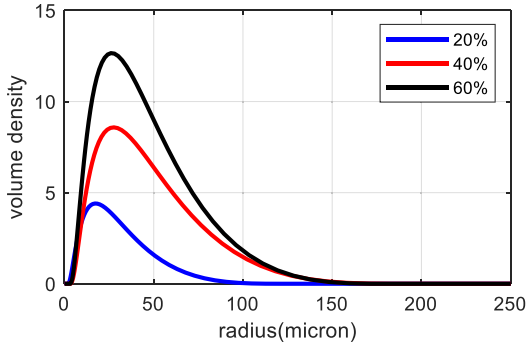

Fig. 4 – Initial DSDs (dimensionless radius-based volume density distribution) for different water volume fractions.

Fig. 3 illustrates the spatial location of iso-volume fractions of 5%, 45%, and 75%. The Kumar and Hartland model (Kumar and Hartland, 1985) and Behzadi et al. model (Behzadi et al., 2004) yield relatively matching predictions except for the iso-volume fractions of 5% at the initial time. Nevertheless, the Richardson-Zaki (Richardson and Zaki, 1954) model significantly differs from the other two. Additionally, our attempt to tune the effective diffusivity model parameters while using this slip velocity model could not provide satisfactory results. It is also notable that our result regarding less accurate predictions using the Richardson-Zaki model has also been reported by other researchers (Panjwani et al., 2015). Finally, the Kumar-Hartland model is chosen as the slip velocity model.

5.3. *Comparison of the model and experiment for the non-coalescing system*

This section compares the experimental data to the model predictions for a non-coalescing system with three different volume fractions, 20%, 40%, and 60%. The pertinent droplet size distributions for different initial volume fractions are depicted in Fig. 4. It must be noticed that only minor variations of the DSD could be observed over a period of 45 min after the emulsion preparation which indicates that coalescence is negligible. It must be emphasized again that for all the cases with different initial volume fractions, the same effective diffusion model parameters were used as described in Section 5.1. In Figs. 5–7, the volume fraction profiles and iso-volume fraction curves are shown for various initial volume fractions. The readers can also refer to the supplementary material for a similar comparison using the volume fraction colormaps.

It is worth mentioning that the first 0–1 mm from the bottom of the column is not depicted for the experimental data. It is due to the glass effect that does not allow accurate measurements using the NMR technique for this region.

Overall, good agreement is observed. The main deviation between the experiments and the model results is related to the destabilization period, typically elapsed time between 10 and 20 min when the advection term of the system mainly governs the dynamics. The model does not predict the same level of sharpness for sedimentation fronts. This is more evident in the volume fraction profiles at earlier times and at the top of the column (Figs. 5–7). This deviation can mainly be explained by the fact that the empirical slip velocity models employed are primarily developed based on studying the monodispersed systems. On the contrary, the model provides more accurate predictions for the volume fraction profiles closer to the end of the sedimentation when the advection terms disappear, and the effective diffusion governs the system.

As also mentioned, the same effective diffusion coefficient model was used for all three cases with different initial volume fractions and DSDs. This indicates that the effective diffusion coefficient does not depend strongly on the DSD. Additionally, the effect of physicochemical properties is lumped in the coefficient C in Eq. (31). From the available models for the elastic modulus (to which effective diffusion is directly proportional) for water-oil emulsions (Mason et al., 1997; Mougel et al., 2006; Princen and Kiss, 1986), we expect that the coefficient C is directly proportional to the interfacial tension. Moreover, from the formula for the drag term (to

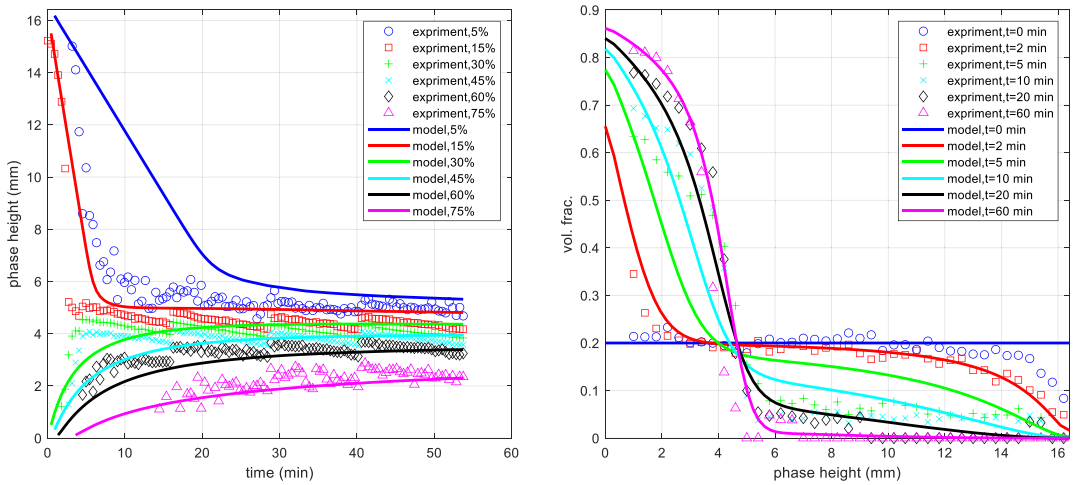

Fig. 5 – Comparison of experiment and model (initial volume fraction=20%), left: various water iso-volume-fraction curves, right: water volume fraction profiles at different elapsed times.

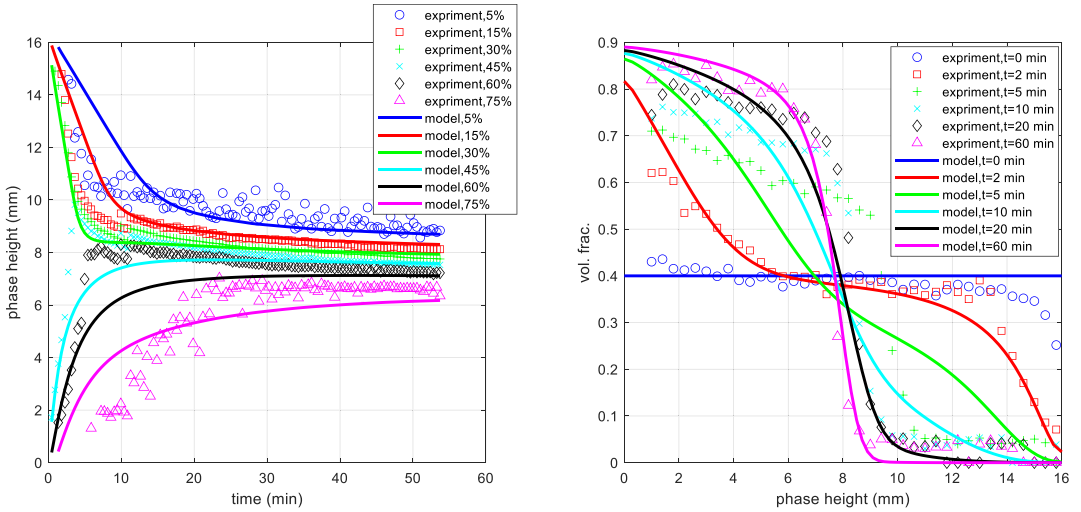

Fig. 6 – Comparison of experiment and model (initial volume fraction=40%), left: various water iso-volume-fraction curves, right: water volume fraction profiles at different elapsed times.

which effective diffusion is inversely proportional) presented by Shih et al. (1986), the C coefficient should also be inversely proportional to the phase density difference and gravitational acceleration. Accordingly, the following proportionality can be deducted for the coefficient C:

$$C \propto \frac{\gamma}{g\,|\rho_d - \rho_c|} \tag{62}$$

Due to measurement range limitation of the tensiometer apparatus (PAT1M from SINTERFACE Technologies), it was not possible to measure interfacial tension value for 800 ppm concentration of Span 80. However, this value should be less than 4.2 mN/m (related to 200 ppm of Span 80 concentration after 1.5 h of adsorption). This limitation did not allow us to corollate the coefficient C according to Eq. (62). However, considering the measurement limitation, we expect a proportionality coefficient less than 203 due to the limitation of the instrument.

5.4. *Case study – a coalescing system*

To evaluate the model results for the system consisting of coalescence, a case study is performed for a water-in-oil system with 40% initial water volume fraction. The model inputs are summarized in Table 2.

The time-space colormaps for volume fraction and the average droplet size are depicted in Fig. 8. At the bottom volume fraction colormap, the formation of the homophase can be observed, which grows at a higher rate until around 3 min; Afterward, it steadily grows at a lower rate. On top of the homophase layer, the formation of the DPL can also be seen. This layer starts to form from the beginning of the

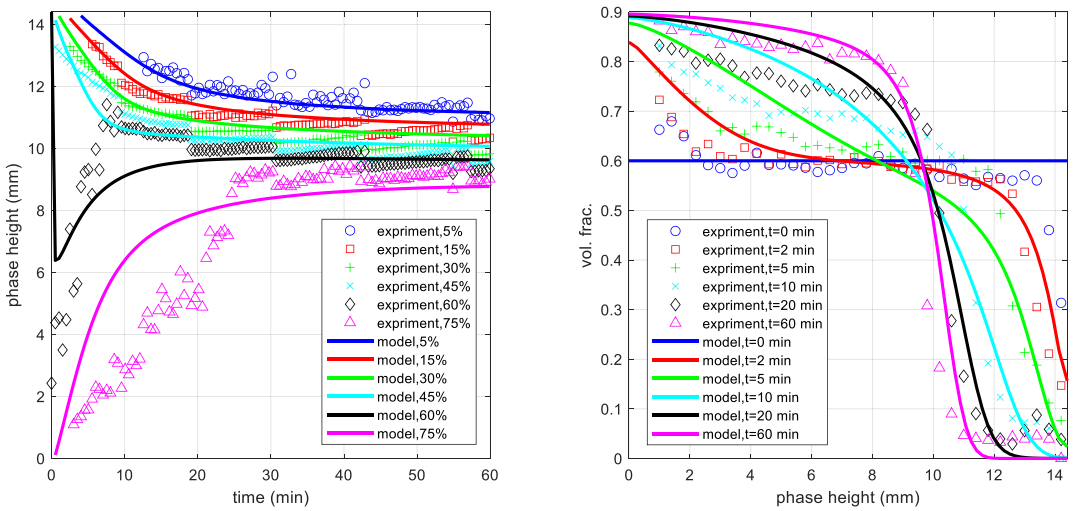

Fig. 7 – Comparison of experiment and model (initial volume fraction=60%), left: various water iso-volume-fraction curves, right: water volume fraction profiles at different elapsed times.

Table 2 – model inputs for the coalescing system case-study.

	Aquous phase	Oil phase
Density (kg/m^3)	1000	850
Viscosity (Pa·s)		20×10^{-3}
Initial vol. Frac.	0.40	
Temperature (K)	300	
Retarded Hamaker constant (N/m^2)	4×10^{-36}	
Interfacial tension (N/m)	15×10^{-3}	
Column height (m)	1.5×10^{-3}	
k_{CR}	1	
k_{CE}	1	
k_{IC}	1	

process; However, the volume friction builds up to the max volume fraction specified for the system, 0.9, at around 4 min. After that, the DPL is fully formed in approximately at a time around 15 min, with its thickness becoming maximum. Then, it shrinks as more water droplets coalesce in the homophase. From the average droplet size colormap for this studied case, the coalescence rate is somewhat faster than the sedimentation rate. As a result, the average droplet size increases from 15 μm to around 40 μm in the first 3 min of the process. Then, due to larger droplet sizes, faster sedimentation rates are observed in the system. Additionally, the increase in the droplet sizes increases the interfacial coalescence time, thus resulting in a slower growth rate of the homophase after 3 min

The volume fraction and average droplet size profiles for different times are shown in Fig. 9. On the right side of Fig. 9, the formation of the homophase can be observed in which the profiles are shifted toward the left. In addition, a drastic increase in both volume fraction and average droplet size can be seen at the bottom of the column as time passes. Here, the volume fraction increases until it reaches a value close to the max volume fraction,0.9. As the volume fraction reaches this point, it remains and does not go higher.

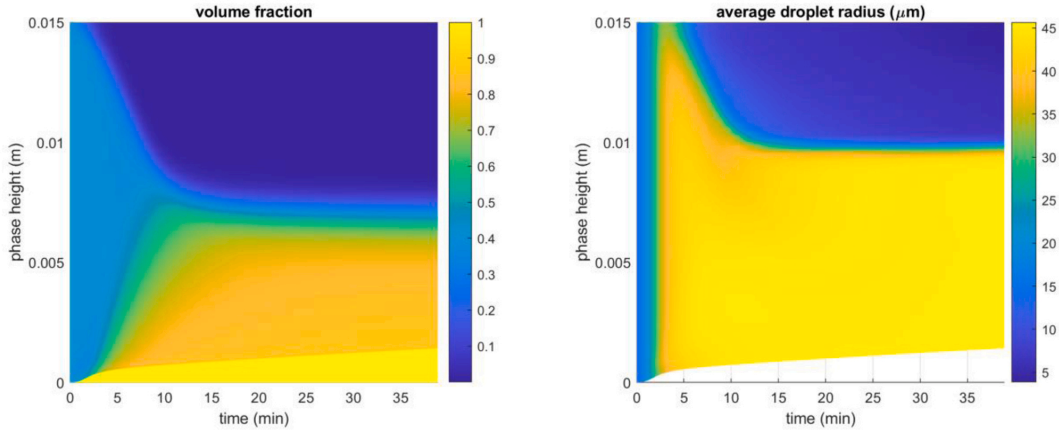

Fig. 8 – Model results colormaps for a coalescing emulsion, initial volume fraction= 40%, right: volume fraction, left: average droplet size.

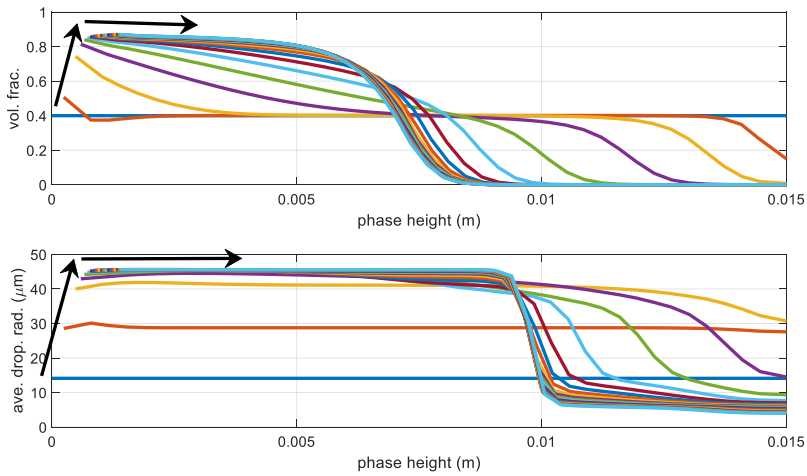

Fig. 9 – Profiles, coalescing emulsion, initial volume fraction= 40%, top: water volume fraction, bottom: average droplet radius.

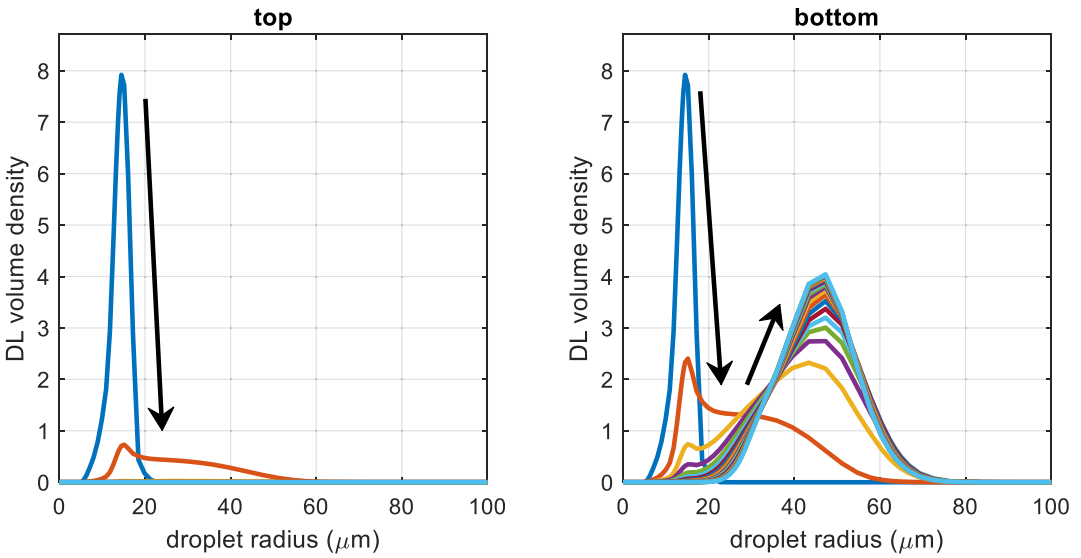

Fig. 10 – Model results for dimensionless volume density distribution, coalescing system, initial volume fraction= 40%, right: top of column, left: bottom of column.

The dimensionless volume density distributions are depicted in Fig. 10 for the top and bottom of the column. At the top of the column, the DSD is rapidly decreasing to zero due to the gravity sedimentation of the droplets to the lower sections of the column. On the contrary, there is a shift toward larger droplet sizes for the bottom of the column. This is a coinciding result of sedimentation and the binary droplet coalescence due to the high-volume fraction in this region.

6. Conclusion

An empirical approach is developed to model the dense-packed layer usually formed in a batch gravity separator. This approach is based on introducing an effective diffusion to the model based on the insight from Shih et al. (1987, 1986). Accordingly, a closure model was proposed for the effective diffusion coefficient with functionalities of the droplet slip velocity and the volume fraction. The selected function for the effective diffusion coefficient asymptotically approaches toward infinity when the volume fraction approaches the maximum allowable volume fraction (as the model parameter). As a result of this high diffusion coefficient, all the excess droplets diffuse back to the surrounding regions with a lower volume fraction. The mentioned issue guarantees that the system's volume fraction is always in the physical range between the zero and maximum allowable volume fraction specified in the model. The described approach was integrated into a general model for the batch gravity separation process. The developed model considers gravity settling/rising of droplets as well as binary and interfacial coalescence using a parallel film drainage model. For slip velocity, three different models were tested and compared and finally, the model by Kumar and Hartland was selected. Furthermore, the model tracks the interface between the dispersion layer and homophase as the homophase grows and the dispersion layer shrinks. This matter results in a moving boundary problem, which was tackled via a spatial-temporal transformation.

Finally, the proposed closure model for the effective diffusion coefficient was tuned using experimental data for a stabilized water in model oil emulsion. Experiments were performed by NMR technique for three volume fractions in the range of 20–60%. The model prediction agrees well with the experiments. Particularly, simultaneous agreement with all cases possessing various initial volume fractions and DSDs suggests that this model can be generalized and applied to a wide range of oil and water emulsions systems. Additionally, the developed model shows promise as it can describe a wide range of initial volume fractions and simultaneously ensure physical values for predicted volume fractions.

For future works we will focus on the below items:

- Applying the model to a coalescing system. That would allow us to tune the interfacial and binary coalescence rates according to a film drainage model with a more realistic assumption by considering the compressive stress force in the DPL as the squeezing force between droplets.
- Comparison between model predictions and experiments for other systems exhibiting different properties. That would allow us to link the effective diffusion coefficient and maximum volume fraction parameter to system physical properties.
- Upscaling of the parameters determined from small-scale experiments.
- Finally, the batch gravity model in this work will be further developed to model the continuous oil/water gravity separators.

Declaration of Competing Interest

The authors declare that they have no known competing financial interests or personal relationships that could have appeared to influence the work reported in this paper.

Acknowledgments

This work was carried out as a part of SFI SUBPRO, a Research-Based Innovation Centre within Subsea Production and Processing. The authors gratefully acknowledge the financial support from SFI SUBPRO, which is financed by the Research Council of Norway (237893), major industry partners, and NTNU. The authors would also like to sincerely acknowledge Total energies Co. for providing the opportunity to use and publish the experimental data.

Appendix A. Supporting information

Supplementary data associated with this article can be found in the online version at doi:10.1016/j.cherd.2023.04.029.

References

Abeynaike, A., Sederman, A.J., Khan, Y., Johns, M.L., Davidson, J.F., Mackley, M.R., 2012. The experimental measurement and modelling of sedimentation and creaming for glycerol/biodiesel droplet dispersions. Chem. Eng. Sci. 79, 125–137. https://doi.org/10.1016/J.CES.2012.05.036

Antonio García, A., Berres, S., Mas-Hernández, E., 2022. A new mathematical model of continuous gravitational separation with coalescence of liquid-liquid emulsions. Chem. Eng. Res. Des. 182, 37–50. https://doi.org/10.1016/J.CHERD.2022.03.044

Antonio García, A., Fernando Betancourt, C., 2019. Conservative mathematical model and numerical simulation of batch gravity settling with coalescence of liquid-liquid dispersions. Chem. Eng. Sci. 207, 1214–1229. https://doi.org/10.1016/J.CES.2019.07.034

Behzadi, A., Issa, R.I., Rusche, H., 2004. Modelling of dispersed bubble and droplet tow at high phase fractions. Chem. Eng. Sci. 59, 759–770. https://doi.org/10.1016/j.ces.2003.11.018

Bury, M., Gerhards, J., Erni, W., Stamm, A., 1995. Application of a new method based on conductivity measurements to determine the creaming stability of o/w emulsions. Int. J. Pharm. 124, 183–194. https://doi.org/10.1016/0378-5173(95)00075-T

Chanamai, R., Herrmann, N., McClements, D.J., 1999. Influence of Thermal Overlap Effects on the Ultrasonic Attenuation Spectra of Polydisperse Oil-in-Water Emulsions. Langmuir 15, 3418–3423. https://doi.org/10.1021/LA981195F

Cunha, R.E.P., Fortuny, M., Dariva, C., Santos, A.F., 2008. Mathematical modeling of the destabilization of crude oil emulsions using population balance equation. Ind. Eng. Chem. Res. 47, 7094–7103. https://doi.org/10.1021/IE800391V/ASSET/IMAGES/LARGE/IE-2008-00391V_0011.JPEG

Anderson, Dale, Tannehill, John C., Pletcher, Richard H., Ramakanth Munipalli, V.S., 2020. Computational Fluid Mechanics and Heat Transfer. CRC Press,.

Deb, T.K., Lebaz, N., Ozdemir, M.S., Govoreanu, R., Mhamdi, A., Sin, G., Sheibat-Othman, N., 2022. Monitoring and Modeling of Creaming in Oil-in-Water Emulsions. Ind. Eng. Chem. Res. 61, 4638–4647. https://doi.org/10.1021/ACS.IECR.1C04722/ASSET/IMAGES/MEDIUM/IE1C04722_0011.GIF

Gear, C.W., 1971. Numerical Initial Value Problems in Ordinary. Differential Equations, 1st ed..,. Prentice Hall,.

Grimes, B.A., 2012, Population Balance Model for Batch Gravity Separation of Crude Oil and Water Emulsions. Part I: Model Formulation. http://dx.doi.org/10.1080/01932691.2011.57494633, 578–590. https://doi.org/10.1080/01932691.2011.574946.

Grimes, B.A., Dorao, C.A., Opedal, N.V.D.T., Kralova, I., Sørland, G.H., Sjöblom, J., 2012. Separation data. J. Dispers. Sci. Technol. 33, 591–598. https://doi.org/10.1080/01932691.2011.574950

Hjartnes, T.N., Sørland, G.H., Simon, S., Sjöblom, J., 2019. Demulsification of Crude Oil Emulsions Tracked by Pulsed Field Gradient (PFG) Nuclear Magnetic Resonance (NMR). Part I: Chemical Demulsification. Ind. Eng. Chem. Res. 58, 2310–2323. https://doi.org/10.1021/ACS.IECR.8B05165/ASSET/IMAGES/MEDIUM/IE-2018-05165K_M002.GIF

Ishii, M., Zuber, N., 1979. Drag coefficient and relative velocity in bubbly, droplet or particulate flows. AIChE J. 25, 843–855. https://doi.org/10.1002/AIC.690250513

Krieger, I.M., Dougherty, T.J., 1959. A Mechanism for non-Newtonian flow in suspensions of rigid spheres. Trans. Soc. Rheol. 3, 137–148.

Kumar, A., Hartland, S., 1985. Gravity settling in liquid/liquid dispersions. Can. J. Chem. Eng. 63, 368–376. https://doi.org/10.1002/CJCE.5450630303

Mason, T.G., Lacasse, M.D., Grest, G.S., Levine, D., Bibette, J., Weitz, D.A., 1997. Osmotic pressure and viscoelastic shear moduli of concentrated emulsions. Phys. Rev. E 56, 3150. https://doi.org/10.1103/PhysRevE.56.3150

Mills, P., 1985. Non-Newtonian behaviour of flocculated suspensions. J. Phys. Lett. 46, 301–309. https://doi.org/10.1051/JPHYSLET:01985004607030100

Mougel, J., Alvarez, O., Baravian, C., Caton, F., Marchal, P., Stébé, M.J., Choplin, L., 2006. Aging of an unstable w/o gel emulsion with a nonionic surfactant. Rheol. Acta 45, 555–560. https://doi.org/10.1007/S00397-006-0089-Z/FIGURES/5

Oshinowo, L.M., Quintero, C.G., Vilagines, R.D., 2016, CFD and Population Balance Modeling of Crude Oil Emulsions in Batch Gravity Separation—Comparison to Ultrasound Experiments. http://dx.doi.org/10.1080/01932691.2015.1054508 37, 665–675. https://doi.org/10.1080/01932691.2015.1054508.

Oshinowo, L.M., Vilagines, R.D., 2020. Modeling of oil–water separation efficiency in three-phase separators: Effect of emulsion rheology and droplet size distribution. Chem. Eng. Res. Des. 159, 278–290. https://doi.org/10.1016/J.CHERD.2020.02.022

Panjwani, B., Amiri, A., Mo, S., Fossen, M., Linga, H., Pauchard, V., 2015. Dense Packed Layer Modeling in Oil-Water Dispersions: Model Description. Exp. Verif., Code Demonstr. https://doi.org/10.1080/01932691.2014.1003221

Princen, H.M., Kiss, A.D., 1986. Rheology of foams and highly concentrated emulsions: III. Static shear modulus. J. Colloid Interface Sci. 112, 427–437. https://doi.org/10.1016/0021-9797(86)90111-6

Richardson, J.F., Zaki, W.N., 1954. The sedimentation of a suspension of uniform spheres under conditions of viscous flow. Chem. Eng. Sci. 3, 65–73. https://doi.org/10.1016/0009-2509(54)85015-9

Rogers, J.R., Davis, R.H., 1990. Modeling of collision and coalescence of droplets during microgravity processing of Zn-Bi immiscible alloys. 1990. Metall. Trans. A 211 (21), 59–68. https://doi.org/10.1007/BF02656424

Ruiz, M.C., Padilla, R., 1996. Separation of liquid-liquid dispersions in a deep-layer gravity settler: Part II. Mathematical modeling of the settler. Hydrometallurgy 42, 281–291. https://doi.org/10.1016/0304-386X(95)00096-Y

Shih, Y.T., Gidaspow, D., Wasan, D.T., 1987. Hydrodynamics of sedimentation of multisized particles. Powder Technol. 50, 201–215. https://doi.org/10.1016/0032-5910(87)80065-7

Shih, Y.T., Gidaspow, D., Wasan, D.T., 1986. Sedimentation of fine particles in nonaqueous media: Part I — experimental Part II — modeling. Colloids Surf. 21, 393–429. https://doi.org/10.1016/0166-6622(86)80106-8

Shiller, L., Naumann, A., 1935. A Drag Coefficient Correlation. Z. Des. Ver. Dtsch. Ing. 77, 318–320.

Simon, S., Pierrard, X., Sjöblom, J., Sørland, G.H., 2011. Separation profile of model water-in-oil emulsions followed by nuclear magnetic resonance (NMR) measurements: Application range and comparison with a multiple-light scattering based

apparatus. J. Colloid Interface Sci. 356, 352–361. https://doi.org/10.1016/J.JCIS.2011.01.012
Sjöblom, J., Mhatre, S., Simon, S., Skartlien, R., Sørland, G., 2021. Emulsions in external electric fields. Adv. Colloid Interface Sci. 294, 102455. https://doi.org/10.1016/J.CIS.2021.102455
Sørland, G.H., 2014. Dynamic Pulsed-Field-Gradient NMR. Springe Ser. Chem. Phys. 110, i–xiii. https://doi.org/10.1007/978-3-662-44500-6/COVER
Van Der Tuuk Opedal, N., Sørland, G., Sjöblom, J., 2009. Methods for Droplet Size Distribution Determination of Water-in-oil Emulsions using Low-Field NMR The Open-Access Journal for the Basic Principles of Diffusion Theory. Exp. Appl. 9, 1–29.
Villadsen, J., Michelsen, M.L., 1978. Solution of differential equation models by polynomial approximation. Englewood Cliffs, New York. Prentice-Hall,.
Wang, H., Davis, R.H., 1995. Simultaneous sedimentation and coalescence of a dilute dispersion of small drops. J. Fluid Mech. 295, 247–261. https://doi.org/10.1017/S0022112095001959
Zimmels, Y., 1983. Theory of hindered sedimentation of polydisperse mixtures. AIChE J. 29, 669–676. https://doi.org/10.1002/AIC.690290423

Supplementary Material for chapter 4

1. Radius-based population balance equation for dispersed layer

This section will consider deriving the radius-based formulation for the dispersion layer. We consider an initially uniform coalescing dispersion that is under the influence of gravity, as depicted in Figure 1. The mass balance equation for the dispersed phase by considering the advection and diffusion terms takes the following form:

$$\frac{\partial f_{n,v}(v,z,t)}{\partial t} = -\frac{\partial}{\partial z}\left[u_d(v,z,t) f_{n,v}(v,z,t)\right] + \frac{\partial}{\partial z}\left(D_e(v,z,t)\frac{\partial f_{n,v}(v,z,t)}{\partial z}\right) + R_{b,n,v} - R_{d,n,v} \quad \text{(S1)}$$

where $f_{n,v}$ is the volume-based number density distribution for a specific droplet size at a particular column location and time. u_d is the pertinent droplet rising/settling velocity. D_e is the effective diffusion coefficient. $R_{b,n,v}$ and $R_{d,n,v}$ are volume-based birth and death rates consistent with the number density distribution resulting from the binary droplet coalescence, respectively. v, z, t are droplet volume, vertical location in the separation column, and elapsed time from the start of the process, respectively. The coalescence birth and death rates in Eq. S1 are as follows:

$$R_{b,n,v}(v,z,t) = \int_0^{v/2} k_c(v', v-v', z, t) f_{n,v}(v', z, t) f_{n,v}(v-v', z, t)\, dv' \quad \text{(S2)}$$

$$R_{d,n,v}(v,z,t) = f_{n,v}(v,z,t) \int_0^{\infty} k_c(v, v', z, t) f_{n,v}(v', z, t) dv' \quad \text{(S3)}$$

where k_c is the coalescence rate between droplets of sizes v and v'. It is possible to transform Eq. S1 to its equivalent radius-based form using the definitions of the two number density distributions and by equating the related equations for dispersed phase volume fraction.

$$\begin{cases} \phi_d = \int_0^{\infty} v f_{n,v} dv = \int_0^{\infty} v f_{n,r} dr \\ dv = 4\pi r^2 dr \end{cases} \quad \rightarrow \quad f_{n,v} = \frac{f_{n,r}}{4\pi r^2} \quad \text{(S4)}$$

By substituting the new density distribution function, governing equation for the dispersion layer takes the following form.

$$\frac{\partial f_{n,r}(r,z,t)}{\partial t} = -\frac{\partial}{\partial z}\left[u_d(r,z,t) f_{n,r}(r,z,t)\right] + \frac{\partial}{\partial z}\left(D_e(r,z,t)\frac{\partial f_{n,r}(r,z,t)}{\partial z}\right) + R_{b,n,r} - R_{d,n,r} \quad \text{(S5)}$$

where the radius-based birth and death rates are defined as:

$$R_{b,n,r} = \int_0^{r/\sqrt[3]{2}} k_c(r', r'', z, t) f_{n,r}(r', z, t) f_{n,r}(r'', z, t) \frac{r^2}{r''^2} dr' \quad \text{(S6)}$$

$$R_{d,n,r} = f_{n,r}(r, z, t) \int_0^{\infty} k_c(r', r'', z, t) f_{n,r}(r', z, t) dr' \quad \text{(S7)}$$

The interested reader can also refer to [1] for more details about the derivation of this form of PBE.

2. Derivation of interfacial coalescence velocity

Consider an oil-water interface with known volume fraction distribution as below:

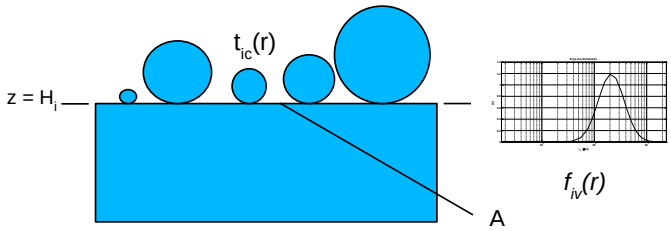

Figure S1: Oil-water interface.

The volumetric flux of drops with size r passing through the interfacial area (i.e., coalescing) over time can be calculated as below:

$$n_{ic}(r) = \frac{\left[\frac{4\pi}{3} r^3 f_{in}(r)\right]}{[\pi r^2 f_{in}(r)]\, t_{ic}(r)} f_{iv}(r) = \frac{4r}{3\, t_{ic}(r)} f_{iv}(r) \quad \text{(S8)}$$

where $f_{in}(r)$ is the number density at the interface, $f_{iv}(r)$ is the volume density at the interface, which is basically the fraction of the total volume of droplets per droplet radius of a given size r. It must be noted that the term $\frac{4\pi}{3} r^3 f_{in}(r)$ represents the total volume of droplets of size r per total volume and droplet radius. The term $\pi r^2 f_{in}(r)$ is the total area of droplets with size r per total volume and droplet radius. $t_{ic}(r)$ is the time taken for a droplet of size r to pass through the interface (i.e., coalescence time). By definition of a convective flux as the product of velocity and volume density variable (written below)

$$n_{ic}(r) = u_{ic} f_{iv}(r) \quad \text{(S9)}$$

, the interfacial velocity is obtained as below:

$$u_{ic}(r) = \frac{4r}{3\, t_{ic}(r)} \quad \text{(S10)}$$

Now the overall dispersed phase flux at the interface can be calculated as below:

$$N_{ic} = \int_0^{\infty} n_{ic}(r)\, dr \qquad \text{(S11)}$$

3. Internal domain discretization

The internal domain (droplet size) was discretized using the spectral-element orthogonal collocation technique. Least number of elements of high order is used. This allows proper error decaying properties together with flexibility to handle both wide and narrow DSDs. The Collocation points are chosen based on the roots of the Jacobi polynomials, and quadrature weights are computed for integration accordingly. Additionally, it is critical to remap the grid points to the collocation points in order to compute the integral for the coalescence birth rate numerically. For this purpose, the monotone piecewise cubic Hermite interpolation [2] technique was employed.

For a non-coalescing case, where the DSD does not extend toward larger droplet sizes, four elements are utilized with the element boundaries chosen based on specific points of the initial distribution. Figure S2 graphically shows this matter. Accordingly, the first element is from zero to the tail of the distribution; the second element from the tail to the average radius of the distribution; the third element is from the average radius to the head of the distribution, and the fourth element is from the head of the distribution to the truncation point. The truncation point is selected by adding a 10% margin over the distribution head.

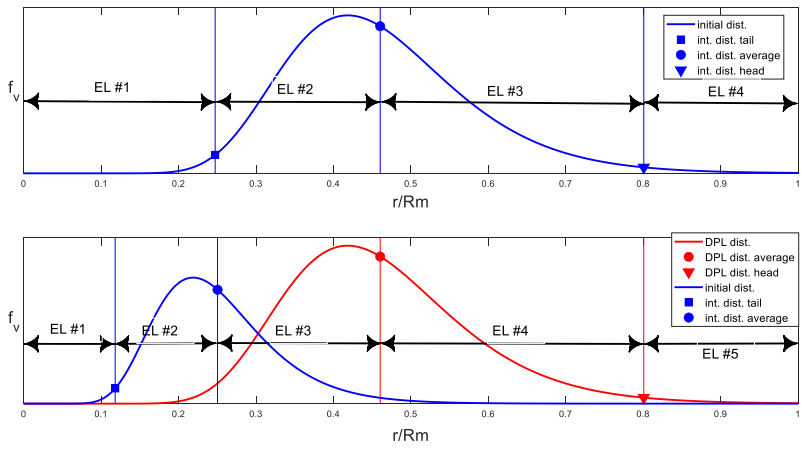

Figure S2: Elements used for internal domain discretization; top: non-coalescing case; bottom: coalescing case.

For a case with coalescence, we considered two distributions to generate the grid, namely, the initial distribution and the worst-case DPL distribution. The DPL distribution can be calculated by solving a spatially homogenous population balance equation using the related-system coalescence model by considering the DPL volume fraction for a transient time equal to the primary problem simulation time. These assumptions are conservative and can guarantee that all DSDs in the system would be located on the left side of this distribution. Then, the whole domain is discretized using five elements. The element boundaries are:

- Element #1: from zero to tail of the initial distribution;
- Element #2: from tail of initial distribution to average radius of initial distribution;
- Element #3: from average radius of initial distribution to average radius of DPL distribution;
- Element #4: from average radius of DPL distribution to head of the DPL distribution;
- Element #5: from head of the DPL distribution to the truncation point (110% of head of the DPL distribution)

In this work, two different grid sizes were evaluated as follows.

- Corse grid: 10 collocation points per element
- Fine grid: 20 collocation points per element

These two grids were used to verify the accuracy of the numerical technique for the discretization of the internal domain. Finally, the fine grid was adopted for all the evaluated cases.

4. Spatial discretization

Vertical coordinate along the column height is discretized using the finite volume technique through an equidistance grid. Advection terms in the equation were treated using the MUSCL technique, which linearly reconstructs the convective flux and droplet velocity profiles over the cell length. Reconstructed convective fluxes, together with the droplet velocities for the left and right sides of each cell boundary can be calculated as follows.

$$n^{L}_{c,j+1/2} = n_{c,j} + \frac{1}{2} minmod(n_{c,j} - n_{c,j-1}, n_{c,j+1} - n_{j}) \quad \text{(S12)}$$

$$n^{R}_{c,j+1/2} = n_{c,j+1} - \frac{1}{2} minmod(n_{c,j+1} - n_{c,j}, n_{c,j+2} - n_{c,j+1}) \quad \text{(S13)}$$

$$u^L_{j+1/2} = u_j + \frac{1}{2} minmod(u_j - u_{j-1}, u_{j+1} - u_j) \quad \text{(S14)}$$

$$u^R_{j+1/2} = u_{j+1} - \frac{1}{2} minmod(u_{j+1} - u_j, u_{j+2} - u_{j+1}) \quad \text{(S15)}$$

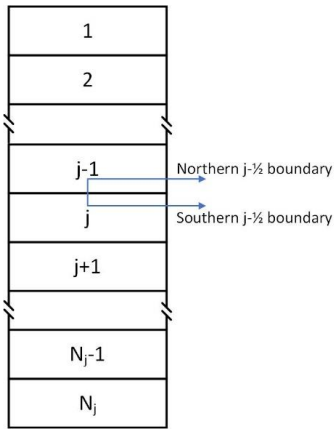

Figure S3: Equidistance finite volume technique used for spatial discretization.

In Eqs. S12-S15, *minmod* is the minimum mode selector function. It is an essential part of the scheme to limit the slope and preserve the total variation diminishing (TVD) property which is crucial to avoid unphysical oscillations. This function is defined as below:

$$minmod(a, b) = sign(a) max\,(0, min\,[|a|, sign(a)b]) \quad \text{(S16)}$$

Now, having the reconstructed convective fluxes as well as the velocities on both sides of each boundary, we can use an upwind scheme to calculate the flux over the boundary as below:

$$n_{c,j+1/2} = \begin{cases} n^R_{c,j+\frac{1}{2}} & if\ \ u^R_{j+\frac{1}{2}} > 0\ \ and\ \ u^L_{j+\frac{1}{2}} > 0 \\ n^L_{c,j+\frac{1}{2}} & if\ \ u^R_{j+\frac{1}{2}} < 0\ \ and\ \ u^L_{j+\frac{1}{2}} < 0 \\ 0 \quad if\ \ \left(u^R_{j+\frac{1}{2}}\right)\left(u^L_{j+\frac{1}{2}}\right) \le 0 \end{cases} \quad \text{(S17)}$$

The described finite volume discretization provides 1st order accuracy for extrema and 2nd order elsewhere. This scheme is applied to all the internal cells. For the interface boundary, the overall flux is set equal to the calculated flux according to the interfacial coalescence. At $z = 0$ (top or bottom), overall flux is set to zero. The fluxes for the rest of the faces of the boundary cells are taken care of by a standard upwind scheme. For diffusive fluxes, central difference fluxes are used.

The central difference employed for diffusion terms, ensures second-order accuracy across all cells. The technique used for advection terms, which involves linear profile reconstruction, also achieves second-order accuracy. However, when an extremum (maximum or minimum point) is present between two cells, the slope limiter maintains a zero slope, effectively reverting to an upwind scheme with first-order accuracy. Consequently, the finite volume discretization described yields first-order accuracy for extrema and second-order accuracy elsewhere.

5. Verification of the numerical scheme

In this section, we evaluate the accuracy of the numerical technique in terms of the adequacy of grid fineness. For that purpose, the iso-volume fraction curves are compared for different grid sizes. In Figure S4, the spatial location of three specific water iso-volume-fraction curves (5%, 45%, 75%) are plotted versus the elapsed time. The considered case for this purpose is non-coalescing sedimentation of water in oil emulsion with a 40% initial water volume fraction. The related physicochemical properties are presented in Table 1. In Figure S4-a, three different grids of sizes 20, 40, and 80 for the spatial domain are compared with a fine internal grid. In Figure S4-b, the internal grid size is evaluated by comparing coarse and fine grids considering a spatial grid size of 40.

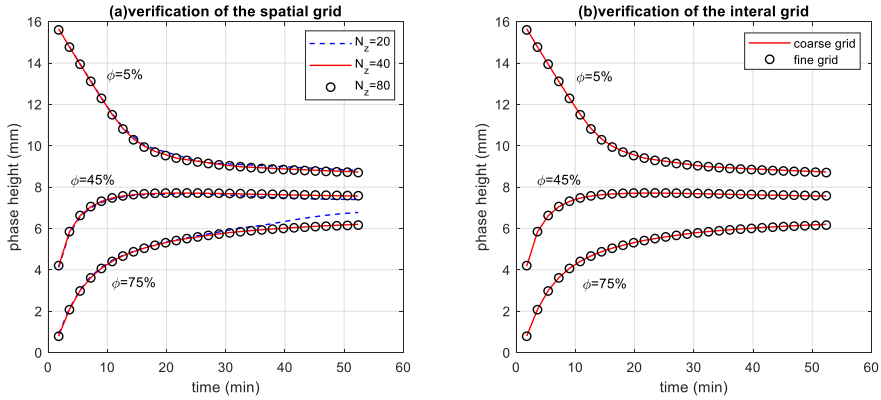

Figure S4: Verification of the numerical grid, a- spatial domain, b- internal domain.

According to Figure S4, the coarse internal grid is adequate for the problem; the mentioned fact is related to the scheme's property where the truncation error exponentially decays by increasing the number of collocation points used for each element. However, for a case with coalescence, the mentioned error property for the scheme might be influenced by the fact that

the distribution is shifting toward larger droplet sizes. Thus, the fine internal grid is used for systems with coalescence, while the non-coalescing systems were treated using the coarse internal grid.

The scheme converges to the same values regarding the spatial grid by increasing the grid size. More specifically, no significant difference is observed between grid sizes 40 and 80. For that reason, grid size 40 was selected for all the computations.

6. Numerical Imbalance

To check the accuracy of the computation, the imbalance in the system was also calculated. Based on this approach, the total amount of the dispersed phase volume in both the dispersion layer and homophase was computed at the system's final state and compared to its initial value. The following formula was used to calculate the fraction of the numerical imbalance in the system.

$$NI(t_f) = \frac{A\int_0^{H_i(t_f)}\int_0^{\infty} f_{v,r}(r,z,t_f)drdz + A(H-H_i(t_f)) - AH\phi_d(0)}{AH\phi_d(0)} \quad \text{(S18)}$$

In dimensionless form, Eq. S18, becomes:

$$NI(\hat{t}_f) = \frac{\bar{H}_i(\hat{t}_f)\int_0^1\int_0^1 \hat{f}_{v,r}(\hat{r},\hat{z},\hat{t}_f)d\hat{r}d\hat{z} + \left(1-\bar{H}_i(\hat{t}_f)\right) - \phi_d(0)}{\phi_d(0)} \quad \text{(S19)}$$

For the non-coalescing cases studied, this value was correlated to the relative tolerance specified for the time integration in the order of 10^{-6}. This is in view of the fact that the finite volume technique used provides conservative discretization (the numerical imbalance generated by this technique is in the order of the machine precision), and the numerical imbalance in the system is mainly imposed by the internal domain discretization and the time integration in the system. Here, the internal discretization is performed to calculate the volume fraction, which is primarily required for the model to compute advection or diffusive fluxes. In contrast, the numerical imbalance was worse for the coalescing case studied. This is primarily because of the error imposed by the non-conservative scheme (spectral-element orthogonal collocation). It was also observed that the numerical imbalances here were significantly affected by the fineness of the internal grid. The values of 1.8×10^{-2} and 2.6×10^{-4} were obtained for coarse and fine grids, respectively.

7. Volume fraction colormaps

The model prediction and the experimental data are also compared for the studied system (water in oil emulsion) using the water volume fraction colormap. Figs. S5, S6, and S7 illustrate the cases with initial volume fractions equal 20%, 40%, and 60%, respectively.

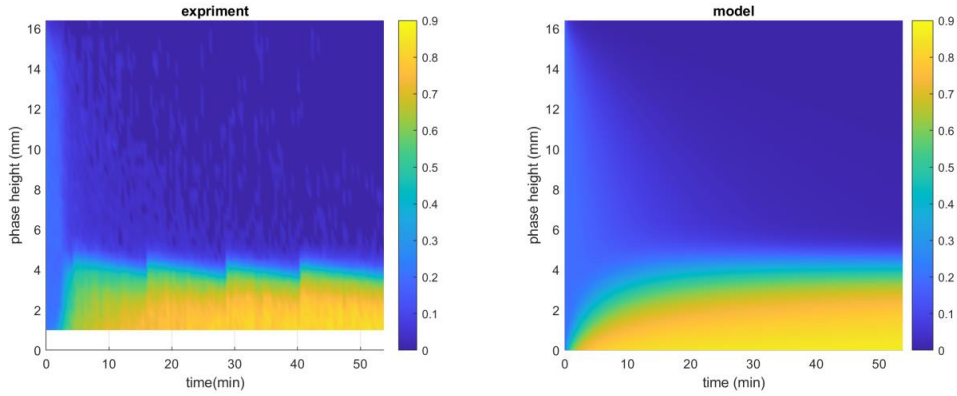

Figure S5: Comparison of the water volume fraction colormaps (initial volume fraction=20%), a- expriment, b- model.

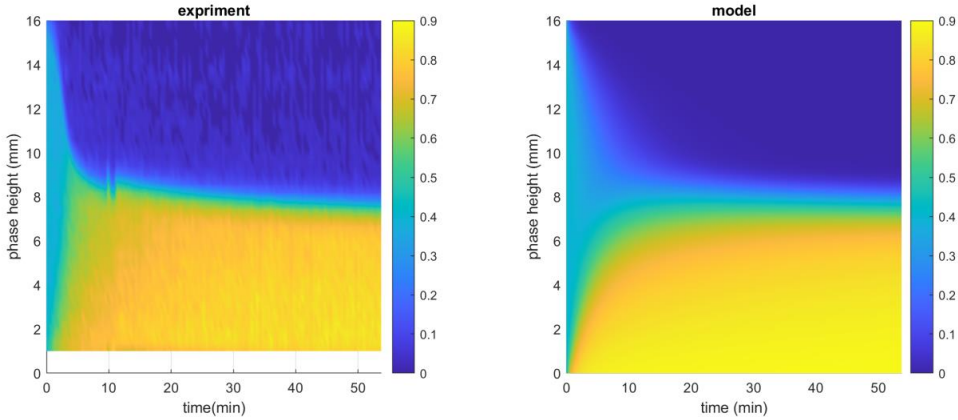

Figure S6: Comparison of the water volume fraction colormaps (initial volume fraction=40%), a- expriment, b- model.

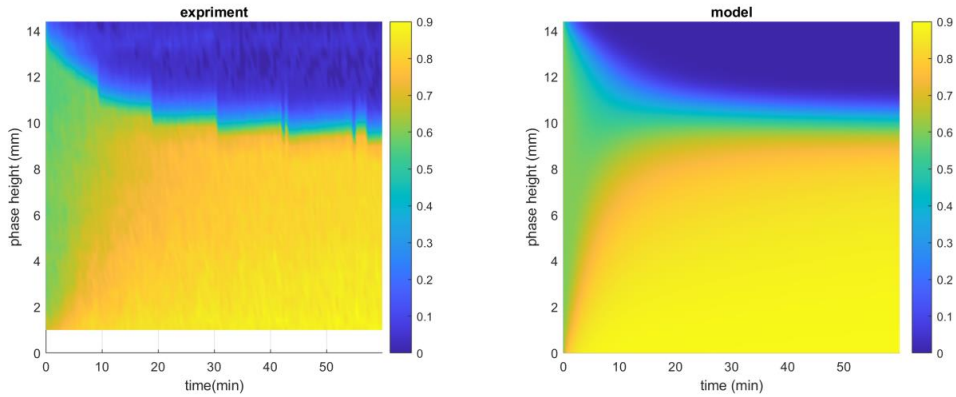

Figure S7: Comparison of the water volume fraction colormaps (initial volume fraction=60%), a- experiment, b- model.

The discontinuities that appear in the experimental data are related to the resolution of the NMR. The NMR has a resolution in height of 0.4 mm.

8. Microscopic images of the emulsions

The microscopic images of the water-in-oil emulsions for different initial volume fractions two minutes after preparation are depicted in Figure S8. These images correspond to the dimensionless radius-based volume density distributions shown in Figure 4.

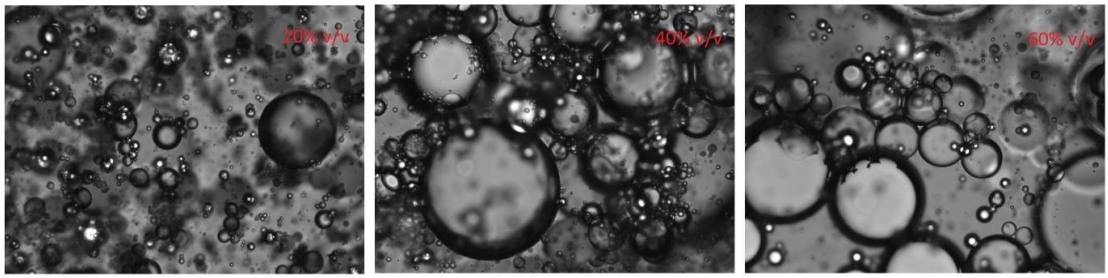

Figure S8: microscopic images of initial emulsions 2 minutes after their preparation, 20%, 40% and 60% water volume fraction from left to right, Scale of the images: 641×479 µm.

Reference

[1] J. Solsvik, H.A. Jakobsen, The Foundation of the Population Balance Equation: A Review, J. Dispers. Sci. Technol. 36 (2015) 510–520. https://doi.org/10.1080/01932691.2014.909318.

[2] F.N. Fritsch, R.E. Carlson, Monotone Piecewise Cubic Interpolation, SIAM J. Numer. Anal. 17 (1980) 238–246. https://doi.org/10.1137/0717021.

Chapter 5

5. Continuous gravity separation (paper III)

This chapter contains the paper-III, which is still in the preparation process, and we intend to submit it to "Chemical Engineering Science". In this study, we have developed a comprehensive model for a 3-phase separator. The model is divided into two parts: the inlet section and the separation section. These two sections are separated by a calming baffle.

The inlet section model incorporates partial oil-water separation as well as spatially homogeneous PBMs that account for turbulent droplet breakage, turbulent droplet coalescence, inflow, and outflow within this section. The turbulent energy dissipation rate is calculated using an averaging strategy, considering the dynamic head of the inlet pipe stream, and allowing for tuning parameters based on the inlet device type.

The separation section model encompasses hydrodynamic and dispersion models. The hydrodynamic model accounts for the transported fluid between the dispersion layers, which influences the velocity profiles. The dispersion models consist of turbulent-induced breakage and coalescence, as well as buoyancy-induced coalescence. This flexibility allows for the model's application in various scenarios, including normal operation conditions and transient conditions such as start-up and shut-down scenarios. The dispersion models essentially constitute two-dimensional advection-diffusion PBMs. Following our previous work on the batch sedimentation, we have incorporated the slip velocity model from Kumar and Hartland, along with the effective diffusion term to account for the formation of the DPL.

Another innovation in this work is the term we have derived for the droplet interfacial coalescence time, which is based on the difference between the gravitational and buoyant forces within a dense pack layer. This allows for establishing a connection between the thickness of the DPL and the rate of interfacial coalescence.

Furthermore, transient level dynamics have been integrated into the model through a spatial-temporal transformation, enabling the study of control schemes and transient upset conditions. To support this, we have developed two distinct solvers to address both steady-state and transient conditions.

In collaboration with another project, we utilized experimental data obtained from a multi-pipe separator to validate the model. The experimental data includes the influence of various parameters, including inlet water-cut and flow rate, on the water separation efficiencies. Consequently, in the current manuscript, we have compared the results of the model with tuning parameters set to unity with the experimental data.

Paper III- Moein Assar, Hamidreza Asaadian, Milan Stanko, Brian Arthur Grimes, A theoretical and experimental investigation of continuous oil-water gravity separation, manuscript in preparation.

Chapter 6

6. Application of geometrically transformed spectral methods for multiphase flow (paper IV)

This chapter consists of the paper-IV published in "Mathematics and Computers in Simulation". The study focuses on the spectral discretization (i.e., the orthogonal collocation technique) of two-dimensional circular geometries, by utilizing a geometrical mapping approach. The technique maintains the error decay characteristics associated with the spectral techniques, often referred to as "order of infinity", when applied to circular geometries. This enables spatial discretization with coarse grids while preserving the accuracy of the numerical solution. The developed technique also addresses the challenge linked to polar discretization which is defining the boundary conditions at the center. Additionally, the squelched mapping technique introduced in this study extends the spectral discretization capabilities to irregular circular segment geometries frequently encountered in multiphase flow scenarios within pipes and separators. Several aspects of these methods, including their error features, condition number, and computational efficiency, are examined. Different implementation issues are presented, including vectorization strategies as well as strategies for tackling the differential-algebraic system of equations. Consequently, user-friendly and computationally efficient numerical procedures have been formulated for solving PDEs within circular geometries, accommodating various boundary conditions for both steady-state and transient problems. Ultimately, this technique is successfully utilized in solving the simplified Navier-Stokes equations for two and three-phase multiphase gravity flows in sloped pipes.

Paper IV- Moein Assar, Brian Arthur Grimes, Geometrically transformed spectral methods to solve partial differential equations in circular geometries, application for multi-phase flow, Mathematics and Computers in Simulation, 215 (2024) 456-475.

Available online at www.sciencedirect.com
ScienceDirect
Mathematics and Computers in Simulation 215 (2024) 456–475
MATHEMATICS AND COMPUTERS IN SIMULATION
www.elsevier.com/locate/matcom

Original articles

Geometrically transformed spectral methods to solve partial differential equations in circular geometries, application for multi-phase flow

Moein Assar, Brian Arthur Grimes*

Ugelstad Laboratory, Department of Chemical Engineering, Norwegian University of Science and Technology (NTNU), N-7491 Trondheim, Norway

Received 14 January 2023; received in revised form 18 July 2023; accepted 11 August 2023
Available online 19 August 2023

Abstract

Circular geometries are ubiquitously encountered in science and technology, and the polar coordinate provides the natural way to analyze them; However, its application is limited to symmetric cases, and it cannot be applied to segments that are formed in multiphase flow problems in pipes. To address that, spectral discretization of circular geometries via orthogonal collocation technique is developed using geometrical mapping. Two analytical mappings between the circle and square geometries, namely, elliptical and horizontally squelched mappings, are employed. Accordingly, numerical algorithms are developed for solving PDEs in circular geometries with different boundary conditions for both steady state and transient problems. Various implementation issues are thoroughly discussed, including vectorization and strategies to avoid solving the differential–algebraic system of equations. Moreover, several case studies for symmetric and asymmetric Poisson equations with different boundary conditions are performed to evaluate several aspects of these techniques, such as error properties, condition number, and computational time. For both steady state and transient solvers, it was revealed that the computation time scales quadratically with respect to the grid size for both mapping and polar discretization techniques. However, due to the presence of the second mixed derivative, mapping techniques are more computationally costly. Finally, the squelched mapping was successfully employed to discretize the two, and three-phase gravity flows in sloped pipes.

Keywords: Spectral methods; Orthogonal collocation; Mapping; Circular geometries; Geometrical transformation

1. Introduction

We live in a world of irregularities where perfect geometrical shapes are either exceptions or human artifacts. However, circular shapes are extensively encountered in many miscellaneous industrial applications. The mentioned issue is primarily related to engineering considerations and offered features like volume to the area ratio and ease of manufacturing. Since the introduction of polar coordinates in the 17th century, it has become the most suitable mathematical approach for driving and solving governing equations for circular shapes. Despite all the convenience

* Corresponding author.
E-mail address: brian.a.grimes@ntnu.no (B.A. Grimes).

https://doi.org/10.1016/j.matcom.2023.08.019

this coordinate system can provide, its application is usually restricted to specific cases. One example is the problems with radial homogeneity (full circle or ring), in which the problem becomes 1D, having the radial dimensions as the only independent variable. Another case that can be tackled in such a manner is a sector of the circle (area enclosed by two radii and an arc), where the problem should be treated as a 2D problem considering the radial and angular directions. Apart from that, polar coordinate cannot be applied to other cases, such as a whole circle lacking radial homogeneity (due to the difficulty defining the boundary condition at the center, or a circle segment (an area between a chord and an arc). Nonetheless, these problems are still faced in multiphase fluid modeling. An example of these problems is the turbulent flow of oil–water emulsion in a horizontal circular pipe [3,10]. This problem is basically described by a spatially distributed advection–diffusion equation where the dispersed phase is under the influence of gravity resulting in a radial-symmetry violation. An example of the circle segments is the liquid levels formed in stratified multiphase flow in a circular pipe [18] as well as in continuous oil–water circular gravity separators [12–14].

One possible way to tackle the described problems is via the so-called spectral techniques in which the value of the dependent variable at a grid point is globally related to all other nodes' dependent variables in that dimension (as opposed to the local techniques like finite volume, finite element, and low-order finite difference techniques). These global techniques offer exponential decay of the truncation error as the numerical grid refines. This property is advantageous as high accuracy can be achieved with relatively coarse grids. The mentioned issue can be specifically beneficial for multi-phase flow problems in which a population balance equation [17] can mathematically describe the polydispersity of the droplet sizes. In such a problem, the droplet size distribution at any spatial location is described by an internal dimension of droplet sizes. Numerical discretization of this problem results in an extensive system of equations as a result of the high dimensionality, which is usually referred to as the curse of dimensionalities. Therefore, applying these spectral techniques to discretize both internal and external dimensions of this problem can significantly improve the computational efficiency.

One widespread spectral (or pseudo-spectral) technique is the orthogonal collocation technique [20]. It belongs to the family of weighted residue techniques. Its popularity is principally due to the ease of mathematics and simplicity of the implementation stemming from adopting the Dirac delta function, which can bypass the additional integration step required for other weighted residue techniques [16]. An example of this popularity is the wide application in reactor design due to its simplicity and numerical efficiency. Remarkably, the availability of numerical programs and libraries has rectified the need to implement the related algorithms (which can be complex and restrictive), leading to its growing acceptance. Among the available open-source programs, "colloc" program [1] for MATLAB by J.W. Eaton and OCC numerical library [21,22] by L.C. Young developed in Fortran with interfaces for Python, Matlab/Octave, Fortran 90+, C++, and Excel are notable.

Despite the broad interests, some pitfalls still limit this technique's application: (i) discontinuity in the problem's physics and (ii) applying it to irregular geometries. The discontinuity issue can be addressed by using the method in an element-based form, which can remedy the oscillation phenomena tightly linked with the Gibbs phenomena. Regardless, this scheme can still suffer from discontinuities with an unspecified location, like shock waves formed in some problems.

Additionally, many efforts have been made to extend these techniques to irregular geometries while maintaining the exponential convergence property. Examples are the domain decomposition method which divides the problem domain into regular subdomains [15,19], and the domain embedding method [2,7,11], in which the problem domain is considered as a part of a regular domain (i.e., rectangle). There are other newer efforts to overcome this challenge. Good examples are the Chebyshev tau matrix method [8] by Kong and Wu and the state of the art technique by Guimaraes et al. [6] based on the parameterization of the Jordan curve defining the domain. Despite the generality these techniques can provide, their application can be limited due to complex implementation procedures as well as a possible decline in computational efficiency [6,11].

Another alternative to approach this challenge is via an analytical geometrical transformation. Here, for unique geometries with an available analytical map (and also inverse map) to a regular geometry, one can geometrically transform the irregular geometry to a regular geometry such as unit square. Accordingly, the governing equations in the irregular geometry should be transformed to its new form in the new regular geometry; then, the spectral grid can be generated and applied to this new transformed governing equation. Finally, the solution can be mapped back to the irregular geometry.

In this work, based on the mentioned idea, we aim to develop a simple to implement and simultaneously numerically efficient technique for solving partial differential equations (PDEs) in circular geometries. Accordingly,

two analytical maps are evaluated and compared to the polar discretization. In addition, efficient numerical procedures for steady-state and transient problems are presented and discussed. Several aspects of the technique, such as error properties, condition number, and computational time are studied through case studies for symmetric and asymmetric Poisson equations with different boundary conditions.

2. Mathematical technique description

2.1. Analytical mappings

As also previously described, the technique involves utilizing a geometrical map between a unit circle (radius=1, center at the coordinate origin) and a square ($[-1,1]\times[-1,1]$) utilizing an analytical mapping (as well as its analytical inverse mapping). It is worth mentioning that this technique can also be used for other geometries that can be conformally transformed to a circle, such as an ellipse. Several such mappings have gained application in imagery science, such as in artistic works. A good summary of these mappings is presented by Fong [4,5]. The interested reader can refer to the complementary material section for a graphical comparison between some of these mappings.

Several aspects should be considered to select an appropriate mapping for our current application, which is solving PDEs. Firstly, since the sharp gradients are usually formed in the vicinity of the circle's boundary, the maps with a higher density of grid points at this region (with still adequately uniform grid density for the interior of the domain) will logically, render better results. The other factor is the simplicity of the mathematics; that is, the maps with simpler mathematical expressions will provide a more straightforward transformed PDE resulting in a more efficient numerical scheme. Based on the mentioned criteria, squelched (Eqs. (1)–(2)) and elliptical (Eqs. (3)–(4)) mappings are good candidates as the mapping formulas are relatively neat and grid points are properly distributed over the domain.

$$\begin{cases} x_s = T_x\,(x_c, y_c) = x_c/\sqrt{1-y_c^2} \\ y_s = T_y\,(x_c, y_c) = y_c \end{cases} \tag{1}$$

$$\begin{cases} x_c = T_x^{-1}\,(x_c, y_c) = x_s\sqrt{1-y_s^2} \\ y_c = T_y^{-1}\,(x_c, y_c) = y_s \end{cases} \tag{2}$$

$$\begin{cases} x_s = T_x\,(x_c, y_c) = \frac{1}{2}\sqrt{2+x_c^2-y_c^2+2\sqrt{2}x_s} - \frac{1}{2}\sqrt{2+x_c^2-y_c^2-2\sqrt{2}x_s} \\ y_s = T_y\,(x_c, y_c) = \frac{1}{2}\sqrt{2-x_c^2+y_c^2+2\sqrt{2}y_s} - \frac{1}{2}\sqrt{2-x_c^2+y_c^2-2\sqrt{2}y_s} \end{cases} \tag{3}$$

$$\begin{cases} x_c = T_x^{-1}\,(x_c, y_c) = x_s\sqrt{1-\frac{y_s^2}{2}} \\ y_c = T_y^{-1}\,(x_c, y_c) = y_s\sqrt{1-\frac{x_s^2}{2}} \end{cases} \tag{4}$$

where subscripts s and c indicate the grid points on the square and circle geometries, respectively. The mappings are compared in Fig. 1 by mapping a 2D orthogonal collocation grid in a square shape using the roots of the Legendre orthogonal polynomial.

2.2. Transformation of the PDE

The presented mappings in Section 2.1 are not conformal; therefore, the form of the equation is not preserved. This necessitates the transformation of the governing equation. For this purpose, we assume the general transformation from the unit circle (radius=1, center at the coordinate origin) to the square ($[-1,1]\times[-1,1]$) as below:

$$x_s = T_x(x_c, y_c) \tag{5}$$

$$y_s = T_y(x_c, y_c) \tag{6}$$

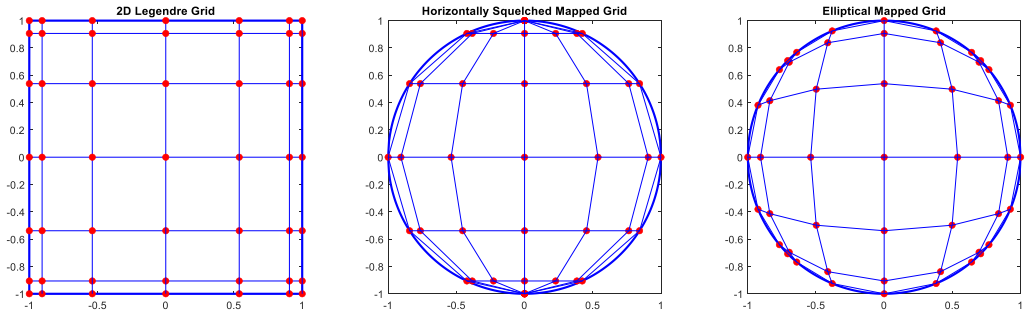

Fig. 1. Comparison of different square-circle mappings; the square grid is an orthogonal collocation grid using the roots of the Legendre polynomial; the grid size is 7 × 7.

The goal is to transform the governing equations into the square geometry. The mentioned task can be done using the chain rule of differentiation which yields the following terms for the dependent variable θ in the direction of the x-axis:

$$\frac{\partial \theta}{\partial x_c} = \frac{\partial T_x}{\partial x_c}\frac{\partial \theta}{\partial x_s} + \frac{\partial T_y}{\partial x_c}\frac{\partial \theta}{\partial y_s} \tag{7}$$

$$\frac{\partial^2 \theta}{\partial x_c^2} = \left(\frac{\partial T_x}{\partial x_c}\right)^2 \frac{\partial^2 \theta}{\partial {x_s}^2} + 2\left(\frac{\partial T_x}{\partial x_c}\right)\left(\frac{\partial T_y}{\partial x_c}\right)\frac{\partial^2 \theta}{\partial x_s \partial y_s} + \left(\frac{\partial^2 T_x}{\partial {x_c}^2}\right)\left(\frac{\partial \theta}{\partial x_s}\right) + \left(\frac{\partial T_y}{\partial x_c}\right)^2 \frac{\partial^2 \theta}{\partial {y_s}^2} + \left(\frac{\partial^2 T_y}{\partial {x_c}^2}\right)\left(\frac{\partial \theta}{\partial y_s}\right) \tag{8}$$

Similarly, spatial derivatives in the y-axis direction becomes:

$$\frac{\partial \theta}{\partial y_c} = \frac{\partial T_x}{\partial y_c}\frac{\partial \theta}{\partial x_s} + \frac{\partial T_y}{\partial y_c}\frac{\partial \theta}{\partial y_s} \tag{9}$$

$$\frac{\partial^2 \theta}{\partial y_c^2} = \left(\frac{\partial T_x}{\partial y_c}\right)^2 \frac{\partial^2 \theta}{\partial {x_s}^2} + 2\left(\frac{\partial T_x}{\partial y_c}\right)\left(\frac{\partial T_y}{\partial y_c}\right)\frac{\partial^2 \theta}{\partial x_s \partial y_s} + \left(\frac{\partial^2 T_x}{\partial {y_c}^2}\right)\left(\frac{\partial \theta}{\partial x_s}\right) + \left(\frac{\partial T_y}{\partial y_c}\right)^2 \frac{\partial^2 \theta}{\partial {y_s}^2} + \left(\frac{\partial^2 T_y}{\partial {y_c}^2}\right)\left(\frac{\partial \theta}{\partial y_s}\right) \tag{10}$$

For more illustration, consider the below dimensionless symmetric diffusion model having a source term in a circle.

$$\frac{\partial \theta}{\partial t} = \frac{1}{r}\frac{\partial}{\partial r}\left(rk\frac{\partial \theta}{\partial r}\right) + \frac{1}{r^2}\frac{\partial}{\partial \phi}\left(k\frac{\partial \theta}{\partial \phi}\right) + S \tag{11}$$

where k is diffusion coefficient and S is the source term. In the case of radial symmetry in this system, the following boundary condition holds:

$$\frac{\partial \theta}{\partial r}(0) = 0 \tag{12}$$

Assuming that the model constant k is spatially invariant, the second term on the right-hand side of Eq. (11) becomes zero. This PDE, subject to a Dirichlet boundary condition at the surface ($\theta(1) = 0$), has a straightforward equilibrium closed-form solution as below.

$$\theta = \frac{S}{4k}\left(1 - r^2\right) \tag{13}$$

Considering a Robin boundary condition for the described system ($k\frac{\partial \theta}{\partial r}(1) + h\theta(1) = 0$), the equation has another simple analytical solution as follows:

$$\theta = \frac{S}{4k}\left(1 + \frac{2k}{h} - r^2\right) \tag{14}$$

where h is the convection coefficient. The following equation can equally describe the PDE (Eq. (11)) in the Cartesian coordinate.

$$\frac{\partial \theta}{\partial t} = \frac{\partial}{\partial x_c}\left(k\frac{\partial \theta}{\partial x_c}\right) + \frac{\partial}{\partial y_c}\left(k\frac{\partial \theta}{\partial y_c}\right) + S \tag{15}$$

Now by substituting the differential terms (Eqs. (8) and (10)) into Eq. (15), the transformed governing equation in the square geometry takes the following form.

$$\frac{\partial \theta}{\partial t} = k\left[a\left(x_c, y_c\right)\frac{\partial^2 \theta}{\partial {x_s}^2} + b\left(x_c, y_c\right)\frac{\partial^2 \theta}{\partial x_s \partial y_s} + c\left(x_c, y_c\right)\frac{\partial^2 \theta}{\partial {y_s}^2} + d\left(x_c, y_c\right)\frac{\partial \theta}{\partial x_s} + e\left(x_c, y_c\right)\frac{\partial \theta}{\partial y_s}\right] + S \tag{16}$$

In this illustrative case, we consider k as constant merely to make the mathematics more straightforward. However, the technique holds generality and can be similarly applied to more complex problems. The geometrical mapping coefficients defined in Eq. (16) have only functionality of the spatial coordinate in the circular geometry and are as below.

$$a\left(x_c, y_c\right) = \left(\frac{\partial T_x}{\partial x_c}\right)^2 + \left(\frac{\partial T_x}{\partial y_c}\right)^2 \tag{17}$$

$$b\left(x_c, y_c\right) = 2\left[\left(\frac{\partial T_x}{\partial x_c}\right)\left(\frac{\partial T_y}{\partial x_c}\right) + \left(\frac{\partial T_x}{\partial y_c}\right)\left(\frac{\partial T_y}{\partial y_c}\right)\right] \tag{18}$$

$$c\left(x_c, y_c\right) = \left[\left(\frac{\partial T_y}{\partial x_c}\right)^2 + \left(\frac{\partial T_y}{\partial y_c}\right)^2\right] \tag{19}$$

$$d\left(x_c, y_c\right) = \left[\left(\frac{\partial^2 T_x}{\partial {x_c}^2}\right) + \left(\frac{\partial^2 T_x}{\partial {y_c}^2}\right)\right] \tag{20}$$

$$e\left(x_c, y_c\right) = \left[\left(\frac{\partial^2 T_y}{\partial {x_c}^2}\right) + \left(\frac{\partial^2 T_y}{\partial {y_c}^2}\right)\right] \tag{21}$$

Since the mappings are analytical, the mentioned spatial coefficients can be analytically derived. The derived analytical expressions for both elliptical and horizontally squelched mapping are presented in the supplementary material section.

2.3. Transformation of the boundary conditions

There are no derivatives in the definition of the Dirichlet boundary condition; as a matter of fact, these boundary conditions can be directly used together with the transformed equation (i.e. Eq. (16)). However, Robin's boundary condition should be transformed as below.

$$\left.\frac{\partial \theta}{\partial x_c}\right|_{r=1}\left.\frac{\partial x_c}{\partial r}\right|_{r=1} + \left.\frac{\partial \theta}{\partial y_c}\right|_{r=1}\left.\frac{\partial y_c}{\partial r}\right|_{r=1} + \left.\frac{h}{k}\theta\right|_{r=1} = 0 \tag{22}$$

In Eq. (22), the geometrical derivatives in the r-direction can be derived using the relation between cartesian and polar coordinates ($x_c = rcos\left(\phi\right)$, $y_c = rsin\left(\phi\right)$). Therefore, these derivatives for a unit circle read as:

$$\frac{\partial x_c}{\partial r} = cos\left(\phi\right) = x_c \tag{23}$$

$$\frac{\partial y_c}{\partial r} = sin\left(\phi\right) = y_c \tag{24}$$

By substituting Eqs. (23)–(24) in Eq. (22), the boundary condition at the circle boundary is obtained as:

$$x_c\left.\frac{\partial \theta}{\partial x_c}\right|_{r=1} + y_c\left.\frac{\partial \theta}{\partial y_c}\right|_{r=1} + \left.\frac{h}{k}\theta\right|_{r=1} = 0 \tag{25}$$

By replacing the dependent variable derivatives in circle geometry using Eqs. (7) and (9), the final form of boundary condition in the square geometry after some simplifications becomes:

$$f\left(x_c, y_c\right)\left.\frac{\partial \theta}{\partial x_s}\right|_{r=1} + g\left(x_c, y_c\right)\left.\frac{\partial \theta}{\partial y_s}\right|_{r=1} + \left.\frac{h}{k}\theta\right|_{r=1} = 0 \tag{26}$$

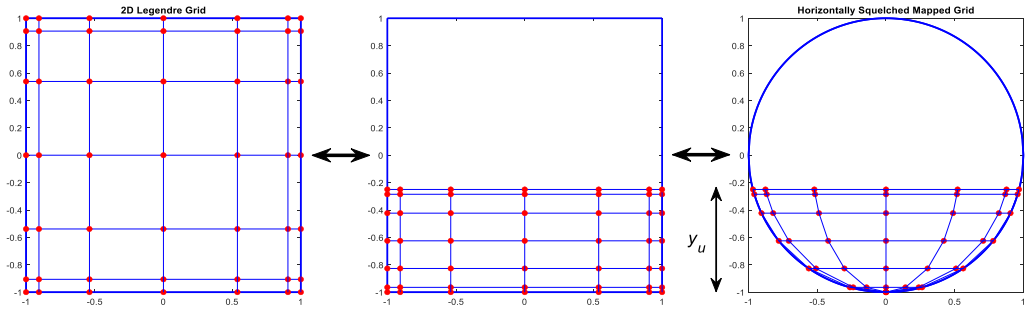

Fig. 2. Truncated horizontally-squelched grid; the square grid is an orthogonal collocation grid using the roots of the Legendre polynomial; the grid size is 7×7.

where the coefficients have only functionality of the spatial coordinate in the circular geometry and are as below.

$$f(x_c, y_c) = \left[x_c \frac{\partial T_x}{\partial x_c} + y_c \frac{\partial T_x}{\partial y_c} \right] \tag{27}$$

$$g(x_c, y_c) = \left[x_c \frac{\partial T_y}{\partial x_c} + y_c \frac{\partial T_y}{\partial y_c} \right] \tag{28}$$

It is worth remarking that the Neumann boundary condition is obtained in the same way as Eq. (26), except without the last term.

2.4. Geometrical transformation of circular segments

Horizontal squelched mapping has an outstanding property that the y-axis is invariant in the transformation. Based on this feature, the geometry shaped for liquid level (e.g., stratified multiphase flow in pipe and 2-phase or 3-phase crude oil separators) can be directly obtained in the case of y-axis truncation between -1 and 1. Yet, in this truncated transformation, a rectangle rather than a square is formed, which needs to be conformally transformed to a square. In other words, using horizontal squelched mapping, liquid levels can be initially transformed into a rectangle, which should subsequently be transformed into a square. The mentioned approach is shown in Fig. 2. Additionally, the Robin boundary condition at the truncated horizontal line can be written as below:

$$\left. \frac{\partial \theta}{\partial y_c} \right|_{y_c = y_u} + \left. \frac{h}{k} \theta \right|_{y_c = y_u} = 0 \tag{29}$$

By substituting the derivatives using Eq. (9), Eq. (29) turns into the following Equation.

$$\left. \frac{\partial T_x}{\partial y_c} \frac{\partial \theta}{\partial x_s} \right|_{y_c = y_u} + \left. \frac{\partial T_y}{\partial y_c} \frac{\partial \theta}{\partial y_s} \right|_{y_c = y_u} + \left. \frac{h}{k} \theta \right|_{y_c = y_u} = 0 \tag{30}$$

where the geometrical derivatives can be found for horizontal squelch mapping presented in supplementary material.

It is worth noting that the described multi-phase flow problems encountered with a circular segment are usually 3D with an axis perpendicular to a circular segment cross-section. Nevertheless, the technique presented here for a 2D plane can be simply extended to these 3D problems as the axial dimension is immediately orthogonal to the circular segment surface.

3. Numerical procedures

The orthogonal collocation method [20] is used to discretize the PDEs. Thanks to the available open-source programs described previously, the weight matrices for differentiation can be easily generated. In this study, the

differentiation weight matrices are generated according to the roots of Legendre orthogonal polynomials (Legendre–Gauss–Lobatto grid), which are symmetric within the range [−1,1]. Accordingly, the vector of the nodal grids can be generated and defined for x_s and y_s directions ($\mathbf{x_s} \in \mathbb{R}^{N_x}$ and $\mathbf{y_s} \in \mathbb{R}^{N_y}$) as below:

$$[\mathbf{x_s}]_i = x_{s,i} \quad for\ i = 1, \ldots, N_x \tag{31}$$

$$[\mathbf{y_s}]_i = y_{s,i} \quad for\ i = 1, \ldots, N_y \tag{32}$$

Using these two vectors, a 2D mesh can now be easily generated on the square geometry ($\mathbf{X_s}, \mathbf{Y_s} \in \mathbb{R}^{N_x \times N_y}$) as follows:

$$[\mathbf{X_s}]_{i,j} = x_{s,i} \tag{33}$$

$$[\mathbf{Y_s}]_{i,j} = y_{s,j} \tag{34}$$

Now, using the inverse mapping, a corresponding 2D mesh can be generated on the circular geometry ($\mathbf{X_c}, \mathbf{Y_c} \in \mathbb{R}^{N_x \times N_y}$) as follows:

$$[\mathbf{X_c}]_{i,j} = x_{c,i,j} \tag{35}$$

$$[\mathbf{Y_c}]_{i,j} = y_{c,i,j} \tag{36}$$

The matrices of the spatial derivatives of the unknown dependent variable (i.e. θ) over the 2D grid can now be approximated by applying the differentiation weight matrices as below:

$$\left[\frac{\partial \boldsymbol{\theta}}{\partial \mathbf{x_s}}\right] \approx \mathbf{A_x}\boldsymbol{\theta} \tag{37}$$

$$\left[\frac{\partial \boldsymbol{\theta}}{\partial \mathbf{y_s}}\right] \approx \mathbf{A_y}\boldsymbol{\theta}^T \tag{38}$$

$$\left[\frac{\partial^2 \boldsymbol{\theta}}{\partial \mathbf{x_s^2}}\right] \approx \mathbf{B_x}\boldsymbol{\theta} \tag{39}$$

$$\left[\frac{\partial^2 \boldsymbol{\theta}}{\partial \mathbf{y_s^2}}\right] \approx \mathbf{B_y}\boldsymbol{\theta}^T \tag{40}$$

where $\mathbf{A_x}, \mathbf{B_x} \in \mathbb{R}^{N_x \times N_x}$ and $\mathbf{A_y}, \mathbf{B_y} \in \mathbb{R}^{N_y \times N_y}$ are differentiation weight matrices. $\boldsymbol{\theta} \in \mathbb{R}^{N_x \times N_y}$ is the matrix of the unknown dependent variables at the grid points. $\left[\frac{\partial \boldsymbol{\theta}}{\partial \mathbf{x_s}}\right], \left[\frac{\partial \boldsymbol{\theta}}{\partial \mathbf{y_s}}\right], \left[\frac{\partial^2 \boldsymbol{\theta}}{\partial \mathbf{x_s^2}}\right], \left[\frac{\partial^2 \boldsymbol{\theta}}{\partial \mathbf{y_s^2}}\right] \in \mathbb{R}^{N_x \times N_y}$ are the first and second derivatives of the unknown dependent variable at the grid points. It must be noted that for a circular segment, $\mathbf{A_y}/(y_u + 1)$ and $\mathbf{B_y}/(y_u + 1)^2$ should be used instead of the differentiation weight matrices where y_u is the height of the domain as shown in Fig. 2. This is a consequence of the conformal mapping process applied to transform the rectangular region into a square.

$$[\boldsymbol{\theta}]_{i,j} = \theta(x_{s,i}, y_{s,j}) \tag{41}$$

$$\left[\frac{\partial \boldsymbol{\theta}}{\partial \mathbf{x_s}}\right]_{i,j} = \frac{\partial \theta}{\partial x_s}(x_{s,i}, y_{s,j}) \tag{42}$$

$$\left[\frac{\partial \boldsymbol{\theta}}{\partial \mathbf{y_s}}\right]_{i,j} = \frac{\partial \theta}{\partial y_s}(x_{s,i}, y_{s,j}) \tag{43}$$

$$\left[\frac{\partial^2 \boldsymbol{\theta}}{\partial \mathbf{x_s^2}}\right]_{i,j} = \frac{\partial^2 \theta}{\partial x_s^2}(x_{s,i}, y_{s,j}) \tag{44}$$

$$\left[\frac{\partial^2 \boldsymbol{\theta}}{\partial \mathbf{y_s^2}}\right]_{i,j} = \frac{\partial^2 \theta}{\partial y_s^2}(x_{s,i}, y_{s,j}) \tag{45}$$

The integration can also be performed using the related quadrature weights vectors as follows:

$$\int_{-1}^{1} \varphi dx_s = \mathbf{q_x}^T \boldsymbol{\varphi} \tag{46}$$

$$\int_{-1}^{1} \omega dy_s = \mathbf{q_y}^T \boldsymbol{\omega} \tag{47}$$

where $\mathbf{q_x} \in \mathbb{R}^{N_x}$ and $\mathbf{q_y} \in \mathbb{R}^{N_y}$ are quadrature weight vectors. $\boldsymbol{\varphi} \in \mathbb{R}^{N_x}$ and $\boldsymbol{\omega} \in \mathbb{R}^{N_y}$ are vectors of variables over the x and y grids, respectively.

Similarly, the geometrical mapping coefficient for the transformed PDE ($\mathbf{a}, \mathbf{b}, \mathbf{c}, \mathbf{d}, \mathbf{e} \in \mathbb{R}^{N_x \times N_y}$) can be precalculated and stored in the form of matrices.

$$[\mathbf{a}]_{i,j} = a(x_{c,i,j}, y_{c,i,j}) \tag{48}$$

$$[\mathbf{b}]_{i,j} = b(x_{c,i,j}, y_{c,i,j}) \tag{49}$$

$$[\mathbf{c}]_{i,j} = c(x_{c,i,j}, y_{c,i,j}) \tag{50}$$

$$[\mathbf{d}]_{i,j} = d(x_{c,i,j}, y_{c,i,j}) \tag{51}$$

$$[\mathbf{e}]_{i,j} = e(x_{c,i,j}, y_{c,i,j}) \tag{52}$$

Another implementation issue is undefined numerical expressions (e.g., division by zero). This can happen during the calculation of the mapping coefficients at specific points on the unit circle boundary. It is essential to follow a systematic approach by directly specifying the boundary conditions for these points, thus avoiding facing the consequent numerical difficulties. The reader is referred to the supplementary material for more details regarding these unspecified points.

3.1. Algorithm implementation for steady-state problems

Eq. (16) can be discretized for the steady-state condition through the Legendre–Gauss–Lobatto (LGL) grid. This discretized form of the equation for an internal node (i, j) takes the following form.

$$\begin{aligned}&\mathbf{a}_{i,j}\sum_{k=1}^{N_x}\mathbf{B}_{x,i,k}\boldsymbol{\theta}_{k,j} + \mathbf{b}_{i,j}\sum_{k=1}^{N_x}\sum_{l=1}^{N_y}\mathbf{A}_{x,k,i}\mathbf{A}_{y,j,l}\boldsymbol{\theta}_{k,l} + \mathbf{c}_{i,j}\sum_{k=1}^{N_y}\mathbf{B}_{y,j,k}\boldsymbol{\theta}_{i,k} + \\ &\mathbf{d}_{i,j}\sum_{k=1}^{N_x}\mathbf{A}_{x,i,k}\boldsymbol{\theta}_{k,j} + \mathbf{e}_{i,j}\sum_{k=1}^{N_y}\mathbf{A}_{y,j,k}\boldsymbol{\theta}_{i,k} = -\frac{S}{k}\ \forall i = 2, \ldots, N_x - 1 \quad \& \quad \forall j = 2, \ldots, N_y - 1\end{aligned} \tag{53}$$

A boundary node with a homogeneous Dirichlet boundary condition has the following equation:

$$\boldsymbol{\theta}_{i,j} = 0 \quad \forall (i, j) \in \text{Dirichlet boundary} \tag{54}$$

The homogeneous Neumann boundary condition for a node on the circle boundary can be specified as:

$$\mathbf{f}_{i,j}\sum_{k=1}^{N_x}\mathbf{A}_{x,i,k}\boldsymbol{\theta}_{k,j} + \mathbf{g}_{i,j}\sum_{k=1}^{N_y}\mathbf{A}_{y,j,k}\boldsymbol{\theta}_{i,k} = 0 \quad \forall (i, j) \in \text{Neumann boundary} \tag{55}$$

The homogeneous Neumann boundary condition for a node on the circle boundary can also be written as below.

$$\mathbf{f}_{i,j}\sum_{k=1}^{N_x}\mathbf{A}_{x,i,k}\boldsymbol{\theta}_{k,j} + \mathbf{g}_{i,j}\sum_{k=1}^{N_y}\mathbf{A}_{y,j,k}\boldsymbol{\theta}_{i,k} + \frac{h}{k}\boldsymbol{\theta}_{i,j} = 0 \quad \forall (i, j) \in \text{Robin boundary} \tag{56}$$

For implementation purposes to handle the multidimensionality of the system, global index notation is also used along with the local indexes as below.

$$m = (j - 1)\, N_x + i \tag{57}$$

Eventually, by systematically assembling all the equations for the internal and boundary nodes, the algebraic equation system can be arranged in the following form.

$$\mathbf{C}\boldsymbol{\theta}^* = \mathbf{h} \tag{58}$$

where $\mathbf{C} \in \mathbb{R}^{(N_x \times N_y) \times (N_x \times N_y)}$ is the coefficient matrix, $\mathbf{h} \in \mathbb{R}^{(N_x \times N_y)}$ is the vector of constants, and $\boldsymbol{\theta}^* \in \mathbb{R}^{(N_x \times N_y)}$ is the reshaped $\boldsymbol{\theta}$ matrix in the form of a vector.

The described discretized system of equations was programmed in MATLAB and solved by LU factorization with partial pivoting (‘*linsolve*’). The sequence of numerical operations for steady-state problems is summarized in Fig. 3.

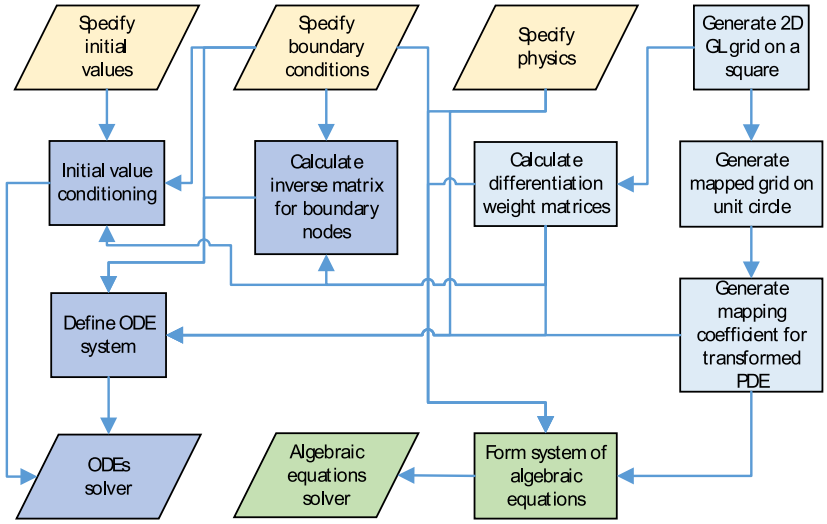

Fig. 3. Indicative numerical algorithm for solving steady-state and transient PDEs.

3.2. Algorithm implementation for transient problems

A semi-discrete formulation for Eq. (16) for an internal node can be written as below:

$$\frac{\partial \boldsymbol{\theta}_{i,j}}{\partial t} = \mathbf{a}_{i,j}k \sum_{k=1}^{N_x} \mathbf{B}_{x,i,k}\boldsymbol{\theta}_{k,j} + \mathbf{b}_{i,j}k \sum_{k=1}^{N_x}\sum_{l=1}^{N_y} \mathbf{A}_{x,k,i}\mathbf{A}_{y,j,l}\boldsymbol{\theta}_{k,l} + \mathbf{c}_{i,j}k \sum_{k=1}^{N_y} \mathbf{B}_{y,j,k}\boldsymbol{\theta}_{i,k} + \mathbf{d}_{i,j}k \sum_{k=1}^{N_x} \mathbf{A}_{x,i,k}\boldsymbol{\theta}_{k,j} + \mathbf{e}_{i,j}k \sum_{k=1}^{N_y} \mathbf{A}_{y,j,k}\boldsymbol{\theta}_{i,k} + S \quad \forall i = 2,\ldots,N_x - 1 \quad \& \quad \forall j = 2,\ldots,N_y - 1 \tag{59}$$

The difficulty arising from the spectral discretization of the problem is that one needs to solve the ordinary differential equations (ODEs) for internal nodes together with the algebraic equations describing the boundary conditions. The mentioned issue leads to a differential–algebraic system of equations (DAEs). One of the main approaches for solving DAEs is converting them to ODEs and applying the available ODE to solve them. However, it is not a trivial task and at the same time, the specified initial condition for the system should hold consistency with the boundary conditions. A good summary of these challenges and the available algorithms for DAEs can be found in [9]. In the current work, instead of using the available DAE solvers, the system of DAEs is converted directly to a system of ODEs taking advantage of the linearity of the algebraic boundary equations. The proposed approach will rectify the need for using a DAE general solver, which can be computationally more expensive and possibly less numerically robust. For this purpose, the strategy is to take the time derivative of the algebraic boundary equations. By doing so, Eqs. (54)–(56) read as:

$$\frac{\partial \boldsymbol{\theta}_{i,j}}{\partial t} = 0 \quad \forall (i,j) \in \text{Dirichlet boundary} \tag{60}$$

$$\mathbf{f}_{i,j} \sum_{k=1}^{N_x} \mathbf{A}_{x,i,k} \frac{\partial \boldsymbol{\theta}_{k,j}}{\partial t} + \mathbf{g}_{i,j} \sum_{k=1}^{N_y} \mathbf{A}_{y,j,k} \frac{\partial \boldsymbol{\theta}_{i,k}}{\partial t} = 0 \quad \forall (i,j) \in \text{Neumann boundary} \tag{61}$$

$$\mathbf{f}_{i,j} \sum_{k=1}^{N_x} \mathbf{A}_{x,i,k} \frac{\partial \boldsymbol{\theta}_{k,j}}{\partial t} + \mathbf{g}_{i,j} \sum_{k=1}^{N_y} \mathbf{A}_{y,j,k} \frac{\partial \boldsymbol{\theta}_{i,k}}{\partial t} + \frac{h}{k}\frac{\partial \boldsymbol{\theta}_{i,j}}{\partial t} = 0 \quad \forall (i,j) \in \text{Robin boundary} \tag{62}$$

When all the boundary conditions are Dirichlet, the numerical scheme can be programmed effortlessly as all the time derivatives dependent variables at the boundary nodes are explicitly specified. Nonetheless, in the case of

spatial derivatives in one or some boundary conditions, the explained approach leads to an implicit system equation for the time derivative of the dependent variable at the boundary nodes (i.e., Eqs. (61)–(62)). Since the boundary equations (Neumann or Robin conditions) are linear, they can be arranged in the following form (all boundary conditions are assumed to be Neumann or Robins):

$$\mathbf{D}\left[\frac{\partial \boldsymbol{\theta}}{\partial \mathbf{t}}\right]_b = \mathbf{k} \tag{63}$$

where $\mathbf{D} \in \mathbb{R}^{(2N_x+2N_y-4)\times(2N_x+2N_y-4)}$ is the coefficient matrix, $\mathbf{k} \in \mathbb{R}^{(2N_x+2N_y-4)}$ is the vector of constants, and $\left[\frac{\partial \boldsymbol{\theta}}{\partial \mathbf{t}}\right]_b \in \mathbb{R}^{(2N_x+2N_y-4)}$ is the vector formed out of the time derivatives of the dependent variable at the boundary nodes using an auxiliary index defined only for the boundary nodes. It must be noted that to arrange Eq. (63), one needs to move all the time derivatives $\frac{\partial \theta}{\partial t}$ at the internal nodes to the right-hand side as they can explicitly be calculated using the variables θ. Consequently, the numerical value for the vector $\mathbf{k}$ should be updated at each time step based on the numerical values of the dependent variable's time derivative at the central nodes. On the contrary, the matrix $\mathbf{D}$ is independent of the dynamic values of variables θ; This issue implies that it can be determined by knowing the geometrical mapping coefficients as well as spatial differentiation weight matrices. Therefore, inverse of matrix $\mathbf{D}$ can be precalculated before starting the time integration to avoid solving the linear system of equations (Eq. (63)) at each time step. Alternatively, the numerical values of the time derivatives $\frac{\partial \theta}{\partial t}$ at the boundary nodes can be calculated using the following matrix operation at each time step.

$$\left[\frac{\partial \boldsymbol{\theta}}{\partial \mathbf{t}}\right]_b = \mathbf{D}^{-1}\mathbf{k} \tag{64}$$

The subsequent system of ODEs was programmed and solved using the MATLAB in-built adaptive ode15s solver, which is a variable-step and variable-order (VSVO) technique based on the numerical differentiation formulas of orders 1 to 5.

Since the algebraic equations for Neumann and Robin conditions at the boundary nodes turned into their equivalent time derivative form, the initial value of the dependent variable at the boundary nodes should now be forced to satisfy the original algebraic boundary equations. Hence, it is vital to undergo a so-called initial value conditioning process by calculating consistent initial numerical values for the dependent variables at boundary nodes before solving the system of ODEs. Similar to the approach previously explained for the time derivative at the boundary nodes, considering all the boundary equations for all the boundary nodes, a linear system of algebraic equations gets formed as below:

$$\mathbf{E}\boldsymbol{\theta}_{b,0} = \mathbf{n} \tag{65}$$

where $\mathbf{E} \in \mathbb{R}^{(2N_x+2N_y-4)\times(2N_x+2N_y-4)}$ is the coefficient matrix, $\mathbf{n} \in \mathbb{R}^{(2N_x+2N_y-4)}$ is the vector of constants, and $\boldsymbol{\theta}_{b,0} \in \mathbb{R}^{(2N_x+2N_y-4)}$ is a matrix assembled out of the dependent variable initial values at the boundary nodes. It must also be noted that to form the mentioned matrix, we have moved all the dependent variables at the internal nodes (with known values) to the right-hand side. The sequence of numerical operations for transient problems is summarized in Fig. 3.

3.3. Vectorization

To maintain the efficiency of the numerical program, it is essential to pre-calculate and store all the matrices that have only dependencies on the geometrical mapping and the OC differentiation coefficients. Additionally, for an interpreted programming language such as MATLAB, it is also vital to perform the matrix operations in a vectorized manner. Notably, the second mixed derivative matrix can be computationally expensive and restrictive when using nested loops. Some examples of pseudocodes for vectorizing the matrix operations in MATLAB are as follows:

$$\frac{\partial^2 \theta}{\partial {x_s}^2}(x_{s,i}, y_{s,j}) \sum_{k=1}^{N_x} \mathbf{B}_{x,i,k}\boldsymbol{\theta}_{k,j} := \mathbf{B}_x(i, :) * \boldsymbol{\theta}(:, j) \tag{66}$$

$$\frac{\partial^2 \theta}{\partial {y_s}^2}(x_{s,i}, y_{s,j}) \sum_{k=1}^{N_y} \mathbf{B}_{y,j,k}\boldsymbol{\theta}_{i,k} : = \mathbf{B}_y(j, :) * \boldsymbol{\theta}^T(:, i) \tag{67}$$

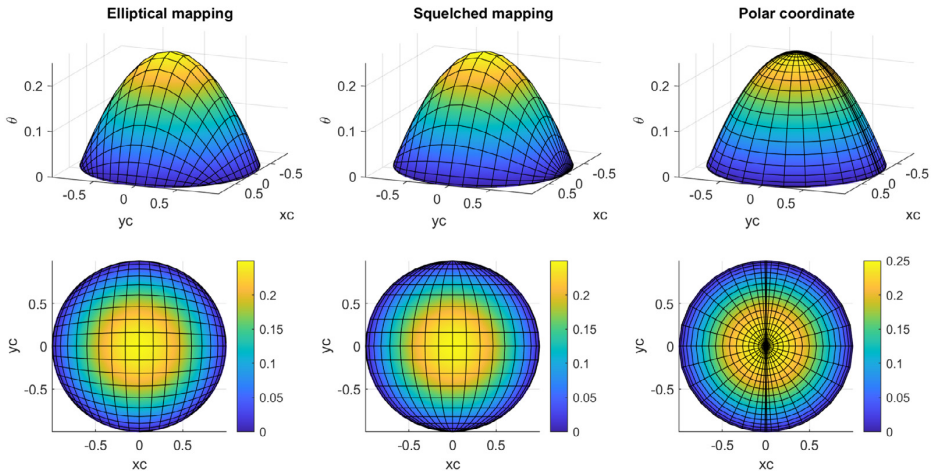

Fig. 4. Steady-state solution of symmetric Poisson Equation with Dirichlet boundary conditions using various discretization techniques, left to right: elliptical grid, squelched grid, and polar grid.

$$\frac{\partial\theta}{\partial x_s}(x_{s,i},\, y_{s,j}) = \sum_{k=1}^{N_x} \mathbf{A}_{x,i,k}\boldsymbol{\theta}_{k,j} \coloneqq \mathbf{A}_x(i,:) * \boldsymbol{\theta}(:,j) \tag{68}$$

$$\frac{\partial\theta}{\partial y_s}(x_{s,i},\, y_{s,j}) = \sum_{k=1}^{N_y} \mathbf{B}_{y,j,k}\boldsymbol{\theta}_{i,k} : = \mathbf{B}_y(j,:) * \boldsymbol{\theta}^T(:,i) \tag{69}$$

$$\frac{\partial^2\theta}{\partial x_s \partial y_s}(x_{s,i},\, y_{s,j}) = \sum_{k=1}^{N_x}\sum_{l=1}^{N_y} \mathbf{A}_{x,k,i}\mathbf{A}_{y,j,l}\boldsymbol{\theta}_{k,l} \coloneqq sum\left(sum\left(\left[\mathbf{A}_x(:,i) * \mathbf{A}_y(j,:)\right] .* \boldsymbol{\theta}\right)\right) \tag{70}$$

$$\int_{-1}^{1}\int_{-1}^{1} \theta dy_s dx_s = \sum_{k=1}^{N_x}\sum_{l=1}^{N_y} \mathbf{q}_{x,k}\mathbf{q}_{y,l}\boldsymbol{\theta}_{k,l} = \mathbf{q}_y{}^T * \left(\mathbf{q}_x{}^T * \boldsymbol{\theta}\right)^T \tag{71}$$

where superscript T shows the transpose operation, '$*$' is matrix multiplication, and '$.*$' refers to the element-wise multiplication operation.

4. Case studies

Diffusion equations with uniform and nonuniform source terms and with various forms of boundary conditions are solved to evaluate and compare multiple aspects of spectral discretization of circular geometries, such as solution accuracy, condition number, and the computational time for the resultant systems of equations. Additionally, the squelched technique has also been employed to solve multi-fluid problems in circular pipes.

4.1. Symmetric Poisson equation

In this section, the results of different techniques for a steady state symmetric Poisson equation (Eq. (15)) are compared with the analytical solution. The following constants were used for the Poisson equation: $S = 1$, $k = 1$ and $h = 0.5$.

Figs. 4 and 5 demonstrate the solution for a symmetric Poisson equation for Dirichlet and Robin boundary conditions, respectively. A grid of size 21×21 is used for all the studied cases. The local relative errors for different cases are calculated with the help of the analytical closed form solution presented previously and depicted in Fig. 6.

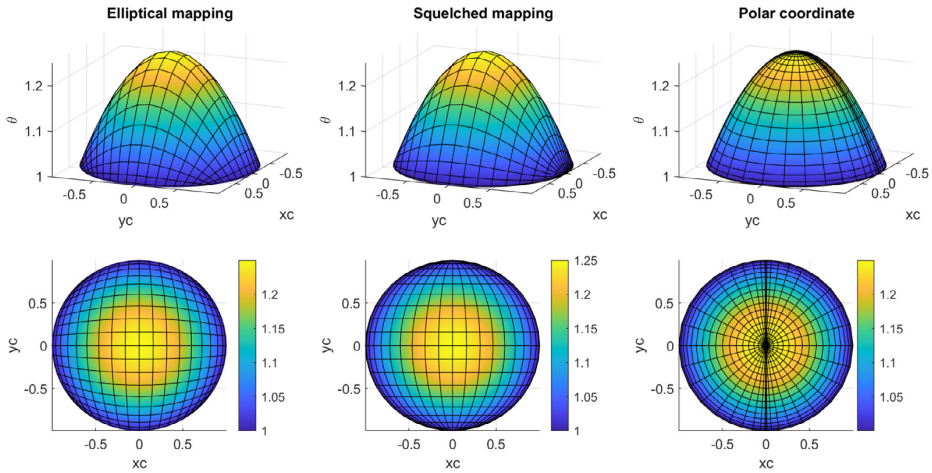

Fig. 5. Steady-state solution of symmetric Poisson Equation with Robin boundary conditions using various discretization techniques, left to right: elliptical grid, squelched grid, and polar grid.

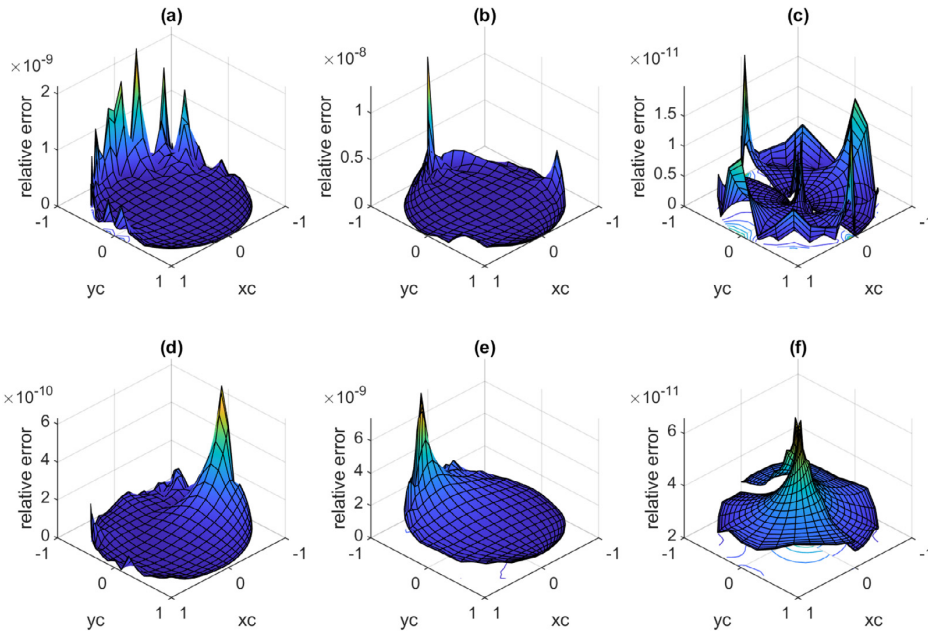

Fig. 6. Numerical local relative error for various techniques and boundary conditions with a grid size of 21 × 21, (a) elliptical mapping — Dirichlet boundary conditions, (b) squelched mapping — Dirichlet boundary conditions, (c) polar coordinate — Dirichlet boundary conditions, (d) elliptical mapping — Robin boundary conditions, (e) squelched mapping — Robin boundary conditions, (f) polar coordinate — Robin boundary conditions.

For both boundary conditions, the local relative error is the lowest in the case of employing the polar coordinate discretization being in the order of 10^{-11}. Elliptical mapping discretization shows somewhat lower relative errors compared to the squelched mapping having values of the order 10^{-10} and 10^{-9} for Robin and Dirichlet boundary conditions, respectively. The effect of the grid size on the average relative error of the whole grid is depicted in Fig. 7 for different discretization techniques and boundary conditions.

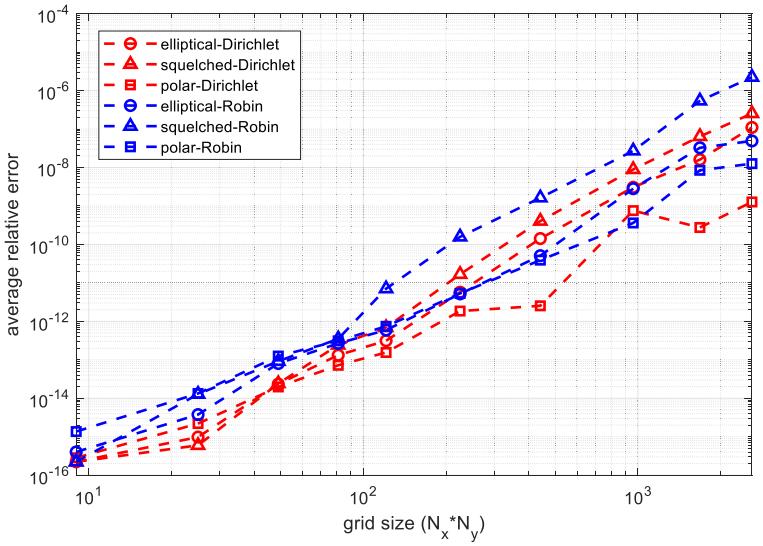

Fig. 7. Numerical average relative error versus grid size for various techniques and boundary conditions.

For all cases, the error generally increases by increasing the grid size (with equal N_x and N_y) with almost the same rate.

In the case of Dirichlet boundary conditions, when using 7 collocation points (a 7×7 grid size), all discretization techniques exhibit relatively similar error properties. However, as the number of collocation points increases, noticeable differences emerge among the techniques. Notably, the polar discretization technique consistently demonstrates the lowest error, followed by the elliptical discretization, while the squelched discretization exhibits the highest average error. A similar trend is observed in the case of Robin boundary conditions, with all techniques showing comparable errors when utilizing 9 collocation points. However, as the number of collocation points increases further, the polar discretization continues to exhibit the lowest error, while the squelched discretization technique consistently produces the highest error.

Moreover, since the studied cases have simple analytical solutions in the forms of polynomials of low order number, the technique with 3 collocation points can generate exact results not allowing to see the exponential decay in the error and rather a continuous increase with number of collocation points due to rounding errors.

It is also important to note that the machine precision was 2.2×10^{-16} and in case of lower error values, they were replaced by the machine precision value for the purpose of generating Fig. 7.

4.2. Asymmetric Poisson equation

In order to generate an asymmetric condition for the Poisson equation, a linear function for the source term S with respect to the y-axis is considered where the value of S is 1 at $y_c = 1$ and 10 at $y_c = -1$. The results are presented in Figs. 8 and 9 for the Dirichlet and Robin boundary conditions, respectively.

An important issue about polar discretization is that the boundary condition at $r = 0$ for a full circle falls inside but not on the outer boundary of the circle. Due to this problem of defining the boundary condition for the circle center, it is not possible to discretize the whole domain directly using polar discretization. However, in the case of dealing with a sector of the circle, boundary conditions can still be defined for the center. Here, the practical mathematical approach is to take advantage of the symmetry in the system, making this approach limited to cases with radial or bi-lateral symmetries so that the boundary condition can be defined at the center. For the current studied case, the following symmetric boundary conditions are considered:

$$\frac{\partial \theta}{\partial r}(0, \phi) = \frac{\partial \theta}{\partial \phi}\left(r, -\frac{\pi}{2}\right) = \frac{\partial \theta}{\partial \phi}\left(r, \frac{\pi}{2}\right) = 0 \tag{72}$$

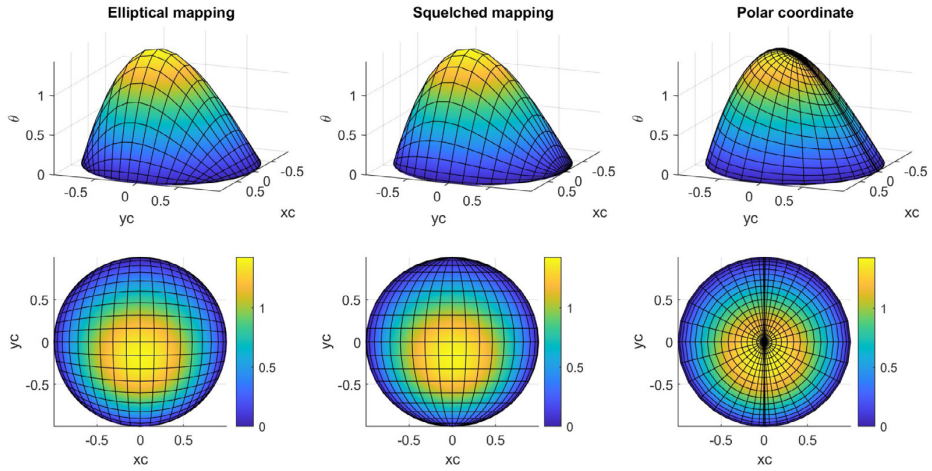

Fig. 8. Steady-state solution of asymmetric Poisson Equation with Dirichlet boundary conditions using various discretization techniques, left to right: elliptical grid, squelched grid, and polar grid.

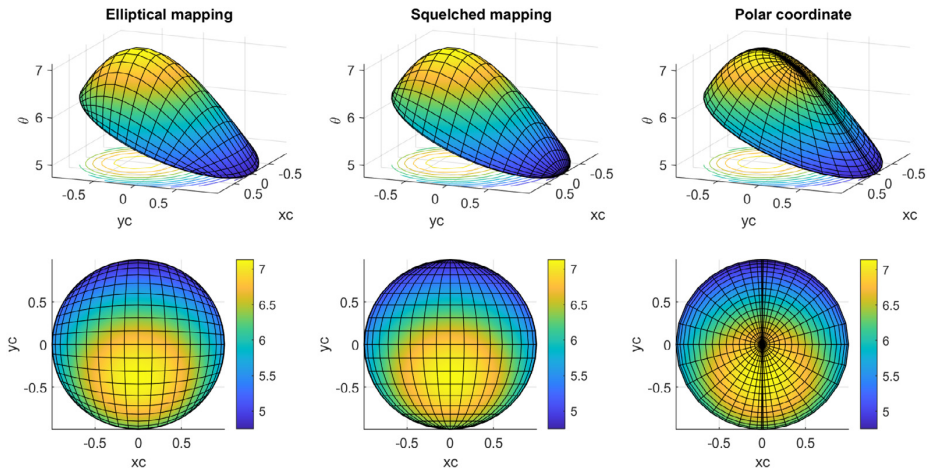

Fig. 9. Steady-state solution of asymmetric Poisson Equation with Robin boundary conditions using various discretization techniques, left to right: elliptical grid, squelched grid, and polar grid.

In other words, polar discretization cannot be applied to a full circle without symmetries. On the contrary, the geometrical mapping techniques (squelched grid and elliptical grid) do not need any symmetries in the system and can always be directly applied to the whole circle.

Another crucial matter is the area coverage of the nodal grid. In a polar grid, a high density of the nodal points is concentrated in the central part with a certain number of points (equal to the grid size for the angular direction) exactly at the center. This results in a fraction of the computational resource being wasted on these redundant points. For the horizontally squelched grid, the redundant points are on the top and bottom of the circle, each having a number equal to the grid size in the x-direction. Despite these redundant points, the rest of the grid points are better distributed over the surface than the polar coordinate. Contrary to polar and squelched grids, elliptical grids offer the best distribution of the grid points over the surface with no redundant points.

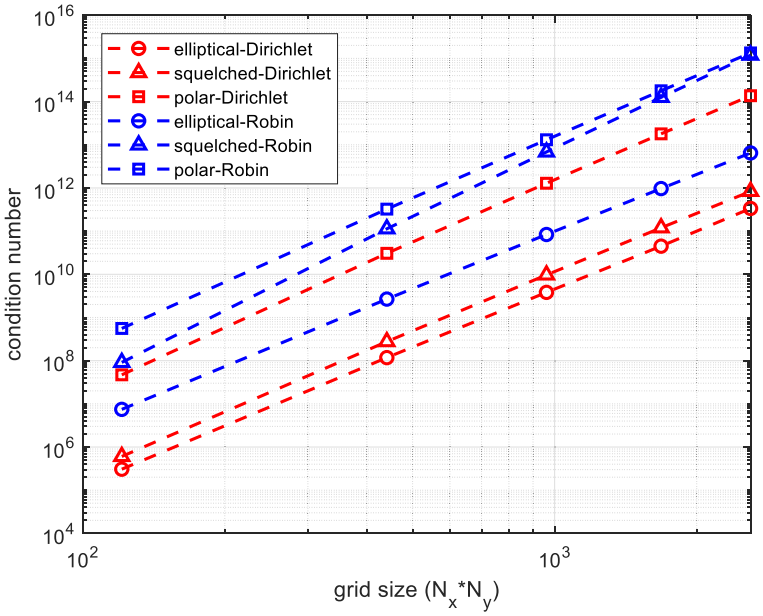

Fig. 10. Condition number of the coefficient matrices versus grid size.

4.3. Condition number for the linear systems

Another essential factor that can affect the accuracy of the solution is the condition number of the coefficient matrix for a linear system. A high condition number does not allow the solution error to decay effectively as the truncation error is decreased by growing the grid size, resulting in an ill-conditioned system of equations. The mentioned issue is studied for different discretization techniques and boundary conditions in Fig. 10.

The condition number curves for various discretization techniques and boundary conditions show almost the same slope in the log–log graph, explaining the similar error trends depicted in Fig. 7. The polar discretization consistently exhibits the highest numerical values for the condition number, while the elliptical discretization shows the lowest values among all techniques for both Dirichlet and Robin boundary conditions.

4.4. Computational efficiency

In this section, the computational times of the developed numerical procedures are evaluated and compared using a desktop computer with an Intel(R) Xeon(R) W-2145 CPU @ 3.70 GHz specification. The computational time for various discretization, boundary conditions, steady state, and transient solvers are presented in Fig. 11.

The cost of computation for the steady state solver is related to two main parts: generating the matrices for the linear algebraic system of equations and the subsequent solution of the system of equations. The direct solution techniques (such as LU decomposition) perform the solution with the same number of floating-point operations for different systems of equations but with the same size. As a result, no difference exists in the absolute computation time of systems of equations resulting from different discretization techniques and boundary conditions. The matter can also be observed in Fig. 11(a). Therefore, the main difference corresponds to the step related to the formation of the coefficient matrix and the vector of constants.

From Fig. 11(a), all the solution techniques for the steady state system using polar discretization and geometrical mapping techniques show approximately quadratic scaling of computation time with the grid size. From Fig. 11(b), the geometrical mapping techniques show around 50%–80% overhead compared to the counterpart polar mapping technique, primarily related to the costly evaluation of the second mixed derivative of the unknown variables. As

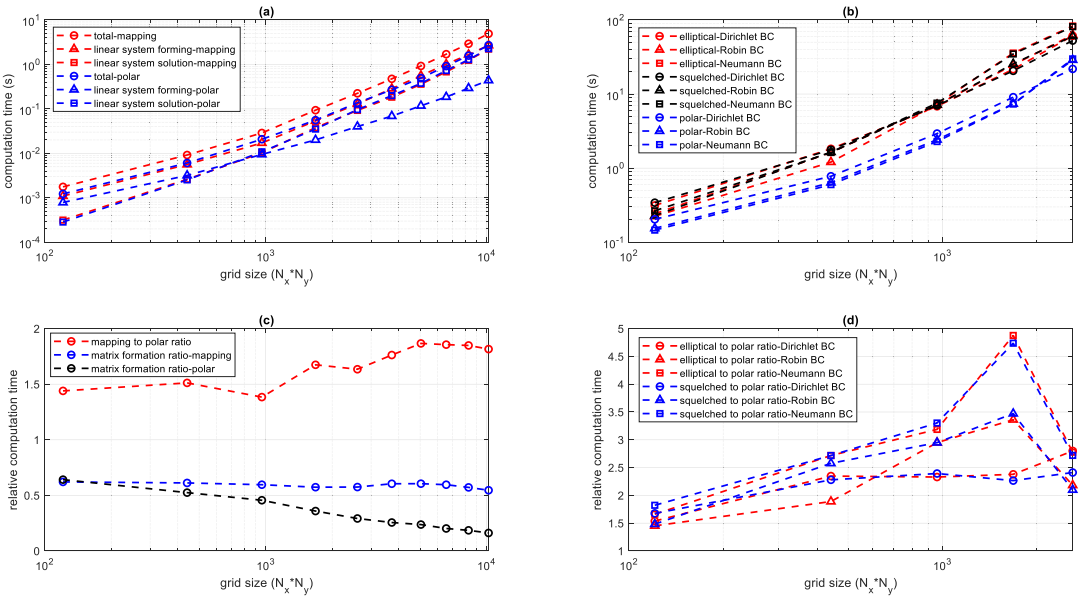

Fig. 11. Computational times, (a) steady state absolute computational times, (b) transient absolute computational times, (c) steady state relative computational times, (d) transient relative computational times.

described, the major difference in the steady state algorithms' computation time corresponds to the computational cost associated with generating the coefficient matrix and the vector of constants for the linear system of equations. This contribution is roughly around 60% for the mapping technique and almost constant at all grid sizes. For the polar coordinate discretization, this value starts from 60% and decreases by grid size growth to 20%. It must be noted that the computation times shown in Fig. 11(a,b) for the mapping case are related to the elliptical mapping technique with the Robin boundary condition. We did not see any significant difference between the squelched and elliptical mappings and different boundary conditions.

The computational time of nine different transient cases with various discretization techniques and boundary conditions are compared in Fig. 11(c). Initial conditions for the Dirichlet and Robin boundary conditions are as below:

$$\theta\left(x_c, y_c, 0\right) = 2 \tag{73}$$

For the cases with the Neumann boundary condition, the source term S was zero, and the initial values were set as the equilibrium steady state of the case with the Dirichlet boundary condition. All the studied transient cases in Fig. 11(c) show approximately quadratic scaling of computation time with the grid size. Fig. 11(d) shows the computational time ratios of mapping techniques to its counterpart polar discretization. For different cases, mapping techniques compared to the polar discretization have overheads between 50%–400%, with little difference between the elliptical mapping and the squelched mapping. These overheads are similarly related to the costly evaluation of the second mixed derivative of the unknown variables.

4.5. Simplified Navier Stokes equation in a circle segment

This section presents applications of the developed technique to solve simplified Navier–Stokes equations for two and three-phase gravity flows in sloped pipes. The following assumptions are made to derive the simplified Navier–Stokes equation for two and three-phase flow in the pipe:

- Inviscid liquid flow (constant density).
- Long homogeneous pipe; flow is assumed fully developed and away from the inlet/outlet effects.

- Stagnant gas phase (constant pressure along the pipe).
- Negligible shear stress at the gas–liquid interface.
- Laminar stratified flow.
- Slip velocity at the pipe wall is considered zero.
- For three-phase flow: slip velocity (velocity difference between phases) at the liquid–liquid interface is assumed to be zero (equal velocities).
- For three-phase flow: equal shear stress for the two liquid phases at the liquid–liquid interface.
- For three-phase flow: the flow rate difference between phases is low so that no vorticity and (3D flow) is formed.

It is worth mentioning that the performed case studies are illustrative, and the simplifying assumptions are only made to make the governing equation 2D avoiding the complexity for better illustration purposes. However, for these studied cases, the axial direction is perpendicular to the pipe cross-section, and the flow can also be considered 3D using this technique. Under the above assumptions, for two-phase flow, the only remaining momentum equation is for the axial velocity direction as below:

$$\frac{\partial^2 U}{\partial x_c^2} + \frac{\partial^2 U}{\partial y_c^2} + \frac{R^2 \rho g sin\,(\alpha)}{\mu} = 0 \tag{74}$$

where U is the axial velocity, ρ is the fluid density, g is the gravitational acceleration, μ is the fluid dynamic viscosity, α is the slope of the pipe from the horizontal line, and R is the pipe radius and has appeared in the source term as the spatial coordinates (x_c and y_c) are made dimensionless. The boundary conditions are also as below:

$$U = 0 \ @ pipewall \tag{75}$$

$$\frac{\partial U}{\partial y_c} = 0 \ @ liquid\text{–}gas\ interface \tag{76}$$

At the same time, since the volumetric flow rate is specified for the system, the liquid level position is unknown. Therefore, the liquid level should be calculated in a way to meet the specified flow rate for the system as below:

$$Q = R^2 \iint U dx_c dy_c \tag{77}$$

In Eq. (77), the differential terms can be substituted according to horizontally squelched mapping as below:

$$dx_c = \sqrt{1 - y_s^2}\, dx_s \tag{78}$$

$$dy_c = dy_s \tag{79}$$

By this substitution, Eq. (77) is turned into the below equation.

$$Q = R^2 \int_{-1}^{y_o} \int_{-1}^{1} U \sqrt{1 - y_s^2}\, dy_s dx_s \tag{80}$$

Eqs. (74) and (80) are the governing equations for the described two-phase flow problem in the pipe. Here, the unknown variables are the velocity field as well as the dimensionless liquid level (y_o). Eq. (80) is a nonlinear equation, while Eq. (74) is linear. As a result, the numerical solution strategy is to initially guess a liquid level, then solve Eq. (74) for the velocity field using the previously described direct technique. Finally, the results can be checked versus Eq. (80) in the form of a numerical residue. The mentioned approach can be translated as solving a one-variable nonlinear equation which was programmed and solved using MATLAB in-built function *fsolve*.

The above problem can be extended to segregated three-phase gravity flow of two immiscible liquids (e.g., water and oil) described by the following equations:

$$\frac{\partial^2 U_h}{\partial x_c^2} + \frac{\partial^2 U_h}{\partial y_c^2} + \frac{R^2 \rho_h g sin\,(\alpha)}{\mu_h} = 0 \tag{81}$$

$$\frac{\partial^2 U_l}{\partial x_c^2} + \frac{\partial^2 U_l}{\partial y_c^2} + \frac{R^2 \rho_l g sin\,(\alpha)}{\mu_l} = 0 \tag{82}$$

Table 1
Physical properties of fluids.

	2phase flow	3phase flow	
		Heavy fluid	Light fluid
Flow rate (m^3/s)	5.0×10^{-5}	5.0×10^{-6}	5.0×10^{-6}
Density (kg/m^3)	1000	1000	900
Viscosity (Pa s)	0.01	0.01	0.1
Pipe internal radius (m)	0.05	0.05	
Pipe angle	0.001°	0.001°	

$$Q_h = R^2 \int_{-1}^{y_i} \int_{-1}^{1} U_h \sqrt{1 - y_s} dx_s dy_s \tag{83}$$

$$Q_l = R^2 \int_{y_i}^{y_o} \int_{-1}^{1} U_l \sqrt{1 - y_s} dx_s dy_s \tag{84}$$

subject to the following boundary conditions:

$$U_h, U_l = 0 \ @pipe\ wall \tag{85}$$

$$\frac{\partial U_l}{\partial y_c} = 0 \ @liquid\text{–}gas\ interface \tag{86}$$

$$\mu_l \frac{\partial U_l}{\partial y_c} = \mu_h \frac{\partial U_h}{\partial y_c} \ @liquid\text{–}liquid\ interface \tag{87}$$

$$U_h = U_l \ @liquid\text{–}liquid\ interface \tag{88}$$

where subscript h and l refer to heavy and light liquid phases, respectively. Similarly, the equations can be discretized (using separate Orthogonal Collocation grids for each of the liquid phases) and arranged as a combination of one linear algebraic solution to calculate the velocity fields for both liquid phases, followed by solving two nonlinear equations for dimensionless liquid levels (y_i as interface level and y_o as the light phase level). The physical constants used for the studied cases are summarized in Table 1.

The calculated velocity fields for two and three-phase fluids are depicted in Fig. 12.

5. Conclusion

In this paper, spectral discretization of 2D circular geometries via orthogonal collocation technique was studied using the geometrical mapping technique. In doing so, two analytical mappings between the circle and square geometries, namely, elliptical and horizontally squelched mappings, were employed. The developed techniques can address the problems of polar discretization for cases without symmetries in which the boundary condition at the center of the circle cannot be defined. Also, contrary to polar discretization, the mapping technique can provide better distribution of the nodal grid as well as fewer redundant grid points. Additionally, the squelched mapping technique enables spectral discretization of the circular segment geometries. This property can be utilized to tackle the irregular geometries formed in multiphase flow problems in pipes. Accordingly, simple to implement while numerically efficient algorithms and procedures are developed for solving PDEs in circular geometries with different boundary conditions for both steady state and transient problems. Special considerations have been devoted to the efficiency of the programs developed in the MATLAB programming language. Various implementation issues are thoroughly discussed, including vectorization and strategies to avoid solving the differential–algebraic system of equations. Several case studies for symmetric and asymmetric Poisson equations with different boundary conditions were performed to evaluate several aspects of these techniques, such as error properties, condition number, and computational time. The followings are the findings:

- The findings highlight the varying performance of the different discretization techniques based on the number of collocation points and the type of boundary condition. The polar discretization technique shows lowest error. Conversely, the squelched discretization technique appears to struggle in achieving that accurate results as the number of collocation points increases.

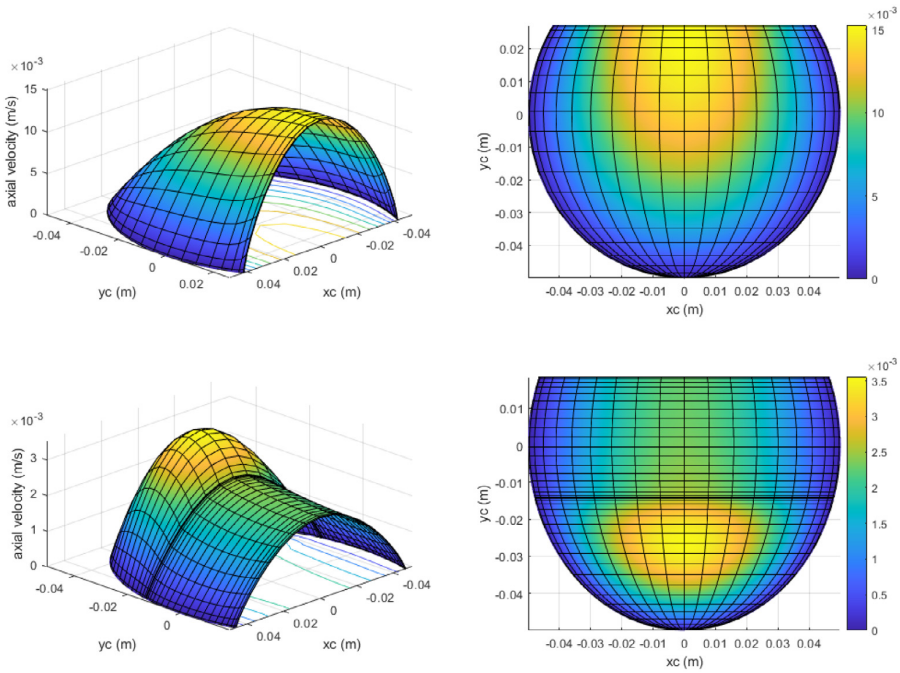

Fig. 12. Simplified Navier–Stokes Equation for multiphase flow, top: two phase stratified flow, bottom: three phase stratified flow.

- The condition number curves for various discretization techniques and boundary conditions show almost the same slope in the log–log graph. This can explain the similar error properties observed among all the studied cases.
- All the solution techniques for both steady-state and transient problems show approximately quadratic scaling of computation time with the grid size. However, the geometrical mapping techniques show around 50%–80% and 50%–400% overhead compared to the counterpart polar mapping technique for steady-state and transient solvers, respectively. These overheads are similarly related to the costly evaluation of the second mixed derivative of the unknown variables.

Among the studied approaches, the squelched mapping technique is the only viable one for the spectral discretization of the circular segments, yet providing reasonable error and computation time. Finally, this technique was successfully employed to discretize the simplified Navier–Stokes equations for two, and three-phase multi-fluid gravity flows in sloped pipes.

In our future work, we will apply the developed techniques to more complex 3D multi-phase flow problems such as a three-phase separator. This task requires the coupling of the Navier–Stokes and population balance equation. Additionally, it is possible to extend the developed program to more complex irregular geometries through numerical mapping and interpolation techniques.

Acknowledgments

This work was carried out as a part of SUBPRO, a Research-Based Innovation Centre within Subsea Production and Processing. The authors gratefully acknowledge the financial support from SUBPRO, which is financed by the Research Council of Norway, major industry partners, and NTNU.

Appendix A. Supplementary data

Supplementary material related to this article can be found online at https://doi.org/10.1016/j.matcom.2023.08.019.

References

[1] J.W. Eaton, Matlab program to calculate collocation weights, 1997, https://github.com/srikanthbojja/matlabtest/blob/master/colloc.m.

[2] M. Elghaoui, R. Pasquetti, A spectral embedding method applied to the advection–diffusion equation, J. Comput. Phys. 125 (1996) 464–476, http://dx.doi.org/10.1006/JCPH.1996.0108.

[3] D. Eskin, A. Vikhansky, Simulation of dispersion of stabilized water droplets in a turbulent oil flow through a horizontal tubing, Chem. Eng. Res. Des. 151 (2019) 261–269, http://dx.doi.org/10.1016/J.CHERD.2019.09.008.

[4] C. Fong, Analytical methods for squaring the disc, 2015, https://doi.org/10.48550/arXiv.1509.06344.

[5] C. Fong, Elliptification of rectangular imagery, 2017, http://dx.doi.org/10.48550/arxiv.1709.07875.

[6] O. Guimarães, J.R.C. Piqueira, Novel approach to spectral methods for irregular domains, Comput. Math. Appl. 80 (2020) 1–12, http://dx.doi.org/10.1016/J.CAMWA.2020.02.016.

[7] B. Khatri Ghimire, H.Y. Tian, A.R. Lamichhane, Numerical solutions of elliptic partial differential equations using Chebyshev polynomials, Comput. Math. Appl. 72 (2016) 1042–1054, http://dx.doi.org/10.1016/J.CAMWA.2016.06.012.

[8] W. Kong, X. Wu, Chebyshev tau matrix method for Poisson-type equations in irregular domain, J. Comput. Appl. Math. 228 (2009) 158–167, http://dx.doi.org/10.1016/J.CAM.2008.09.011.

[9] P. Kunkel, V. Mehrmann, Differential-Algebraic Equations: Analysis and Numerical Solution, European Mathematical Society, 2006.

[10] J. Lovick, P. Angeli, Droplet size and velocity profiles in liquid–liquid horizontal flows, Chem. Eng. Sci. 59 (2004) 3105–3115, http://dx.doi.org/10.1016/J.CES.2004.04.035.

[11] S.H. Lui, Spectral domain embedding for elliptic PDEs in complex domains, J. Comput. Appl. Math. 225 (2009) 541–557, http://dx.doi.org/10.1016/J.CAM.2008.08.034.

[12] L.M. Oshinowo, C.G. Quintero, R.D. Vilagines, CFD and population balance modeling of crude oil emulsions in batch gravity separation—Comparison to ultrasound experiments, J. Dispers. Sci. Technol. 37 (5) (2016) 665–675, http://dx.doi.org/10.1080/01932691.2015.1054508.

[13] L.M. Oshinowo, R.D. Vilagines, Modeling of oil–water separation efficiency in three-phase separators: Effect of emulsion rheology and droplet size distribution, Chem. Eng. Res. Des. 159 (2020) 278–290, http://dx.doi.org/10.1016/J.CHERD.2020.02.022.

[14] B. Panjwani, A. Amiri, S. Mo, M. Fossen, H. Linga, V. Pauchard, Dense packed layer modeling in oil-water dispersions: Model description, experimental verification, and code demonstration, J. Dispers. Sci. Technol. 36 (10) (2015) 1527–1537, http://dx.doi.org/10.1080/01932691.2014.1003221.

[15] A. Quarteroni, A. Valli, Domain decomposition for partial differential equations, Oxford University Press, 1999.

[16] J. Solsvik, H.A. Jakobsen, Evaluation of the least-squares method for the solution of the population balance equation, J. Dispers. Sci. Technol. 36 (2015) 68–82, http://dx.doi.org/10.1080/01932691.2014.880848.

[17] J. Solsvik, H.A. Jakobsen, The foundation of the population balance equation: A review, J. Dispers. Sci. Technol. 36 (2015) 510–520, http://dx.doi.org/10.1080/01932691.2014.909318.

[18] Y. Taitel, D. Barnea, J.P. Brill, Stratified three phase flow in pipes, Int. J. Multiph. Flow 21 (1995) 53–60, http://dx.doi.org/10.1016/0301-9322(94)00058-R.

[19] a. Toselli, O. Widlund, Domain Decomposition Methods — Algorithms and Theory, Springer Berlin, Heidelberg, 2005, http://dx.doi.org/10.1007/b137868.

[20] J. Villadsen, M.L. Michelsen, Solution of Differential Equation Models By Polynomial Approximation, Prentice-Hall, Englewood Cliffs, New York, 1978.

[21] L.C. Young, Computer code documentation, 2019, https://www.tildentechnologies.com/Numerics/Docs/Codes_OC.pdf.

[22] L.C. Young, Implementing weighted residual, spectral and finite element methods orthogonal collocation, pseudospectral, differential quadrature, 2020, https://www.tildentechnologies.com/Numerics/Docs/MWR_Young_20_01_27.pdf.

Supplementary material for chapter 6

1. Comparison of some of the available analytical mapping between square and circle

An equidistant 2D grid (14×14) was initially generated in unit square and mapped into unit circle (radius 1 and center at coordinate origin) using different available analytical mappings. The results are compared in Figure S1.

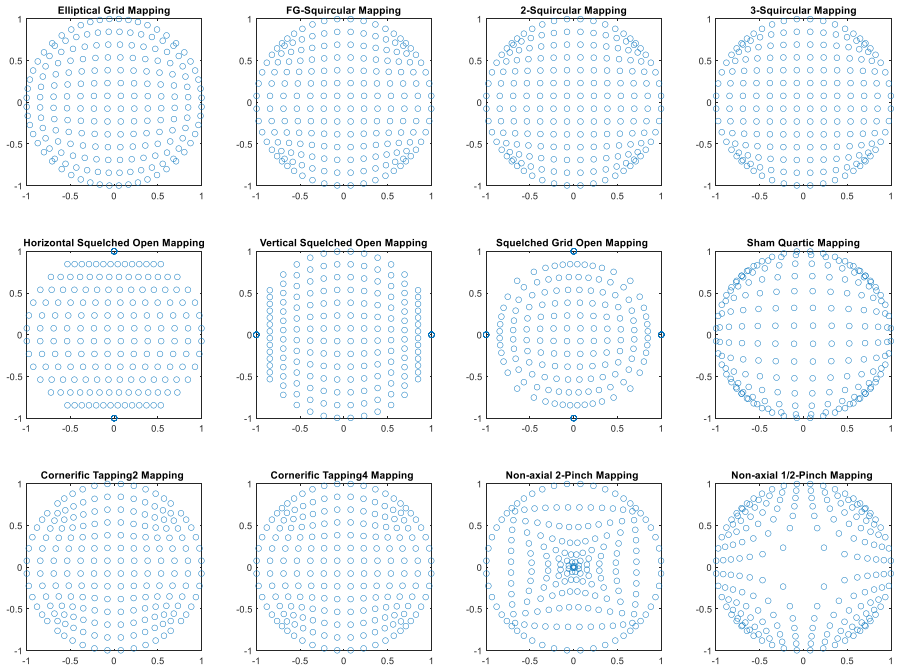

Figure S1: Comparison of different square-circle mappings, original grid is an equidistant 14×14 grid in unit square.

Figure S1, vividly demonstrates the grid distribution of different mapping from unit square to unit circle. Some mappings, such as elliptical mapping, display a more uniform distribution, while others are more unevenly distributed.

2. Squelched mapping coefficients

2.1. Geometrical derivatives

Geometrical map's derivatives which are used to transform the governing equation and boundary conditions to the unit square geometry are presented in this section for horizontal Squelched mapping.

$$\left(\frac{\partial T_x}{\partial x_c}\right) = \frac{1}{\sqrt{1-y_c^2}} \tag{S1}$$

$$\left(\frac{\partial^2 T_x}{\partial {x_c}^2}\right) = 0 \tag{S2}$$

$$\left(\frac{\partial T_x}{\partial y_c}\right) = \frac{x_c y_c}{(1-y_c^2)^{3/2}} \tag{S3}$$

$$\left(\frac{\partial^2 T_x}{\partial {y_c}^2}\right) = \frac{x_c\left(2{y_c}^2+1\right)}{(1-y_c^2)^{5/2}} \tag{S4}$$

$$\left(\frac{\partial T_y}{\partial x_c}\right) = 0 \tag{S5}$$

$$\left(\frac{\partial^2 T_y}{\partial {x_c}^2}\right) = 0 \tag{S6}$$

$$\left(\frac{\partial T_y}{\partial y_c}\right) = 1 \tag{S7}$$

$$\left(\frac{\partial^2 T_y}{\partial {y_c}^2}\right) = 0 \tag{S8}$$

2.2. Mapped Poisson equation coefficients

Derivatives that appear in the mapped 2D Poisson equation have only functionality of the geometrical map derivative. The analytical expressions for these coefficients are presented in this section for horizontal Squelched mapping.

$$a = \frac{-1}{y_c^2-1} + \frac{{x_c}^2{y_c}^2}{(y_c^2-1)^3} \tag{S9}$$

$$b = \frac{2x_c y_c}{(1-y_c^2)^{3/2}} \tag{S10}$$

$$c = 1 \tag{S11}$$

$$d = \frac{x_c\left(2{y_c}^2+1\right)}{(1-y_c^2)^{5/2}} \tag{S12}$$

$$e = 0 \tag{S13}$$

$$f = \frac{x_c}{(1-y_c^2)^{3/2}} \tag{S14}$$

$$g = y_c \tag{S15}$$

The unspecified points in the coefficients are related to $y_c = \pm 1$. These points are located on the circle boundary. As a result, the numerical value of the coefficient f is not bounded in the case of derivatives in the boundary condition (Neumann or Robin boundary conditions). However, in case of $x_c = 0$, the value of f practically becomes zero. Furthermore, since all the grid points on x-axis at $y_c = \pm 1$ collapse to only one point. It is feasible to use the value of the grid point at $x_c = 0$ and keep all other grid points equal to that value.

3. Elliptical mapping coefficients

3.1. Geometrical derivatives

Geometrical map's derivatives which are used to transform the governing equation and boundary conditions to the unit square geometry are presented in this section for elliptical mapping.

$$\left(\frac{\partial T_x}{\partial x_c}\right) = \frac{x_c+\sqrt{2}}{2\#_2} - \frac{x_c-\sqrt{2}}{2\#_1} \tag{S16}$$

$$\left(\frac{\partial^2 T_x}{\partial {x_c}^2}\right) = -\frac{y_c^2\left({\#_1}^3-{\#_2}^3\right)}{2{\#_1}^3{\#_2}^3} \tag{S17}$$

$$\left(\frac{\partial T_x}{\partial y_c}\right) = \frac{y_c}{2\#_1} - \frac{y_c}{2\#_2} \tag{S18}$$

$$\left(\frac{\partial^2 T_x}{\partial {y_c}^2}\right) = \frac{1}{2\#_1} - \frac{1}{2\#_2} + \frac{y_c^2}{2{\#_1}^3} - \frac{y_c^2}{2{\#_2}^3} \tag{S19}$$

$$\left(\frac{\partial T_y}{\partial x_c}\right) = \frac{x_c}{2\#_3} - \frac{x_c}{2\#_4} \tag{S20}$$

$$\left(\frac{\partial^2 T_y}{\partial {x_c}^2}\right) = \frac{1}{2\#_3} - \frac{1}{2\#_4} + \frac{x_c^2}{2{\#_3}^3} - \frac{x_c^2}{2{\#_4}^3} \tag{S21}$$

$$\left(\frac{\partial T_y}{\partial y_c}\right) = \frac{y_c+\sqrt{2}}{2\#_4} - \frac{y_c-\sqrt{2}}{2\#_3} \tag{S22}$$

$$\left(\frac{\partial^2 T_y}{\partial {y_c}^2}\right) = -\frac{x_c^2\left({\#_3}^3 - {\#_4}^3\right)}{2{\#_3}^3{\#_4}^3} \tag{S23}$$

where the auxiliary variables $(\#_1, \#_2, \#_3, \#_4)$ are defined as below.

$$\#_1 = \left({x_c}^2 - {y_c}^2 - 2\sqrt{2}x_c + 2\right)^{1/2} \tag{S24}$$

$$\#_2 = \left({x_c}^2 - {y_c}^2 + 2\sqrt{2}x_c + 2\right)^{1/2} \tag{S25}$$

$$\#_3 = \left({y_c}^2 - {x_c}^2 - 2\sqrt{2}y_c + 2\right)^{1/2} \tag{S26}$$

$$\#_4 = \left({y_c}^2 - {x_c}^2 + 2\sqrt{2}y_c + 2\right)^{1/2} \tag{S27}$$

3.2. Mapped Poisson equation coefficients

Derivatives that appear in the mapped 2D Poisson equation have only functionality of the geometrical map derivative. The analytical expressions for these coefficients are presented in this section for horizontal Squelched mapping.

$$a = \left(\frac{x_c+\sqrt{2}}{2\#_2} - \frac{x_c-\sqrt{2}}{2\#_1}\right)^2 + \left(\frac{y_c}{2\#_1} - \frac{y_c}{2\#_2}\right)^2 \tag{S28}$$

$$b = \left(\frac{x_c+\sqrt{2}}{\#_2} - \frac{x_c-\sqrt{2}}{\#_1}\right)\left(\frac{x_c}{\#_3} - \frac{x_c}{\#_4}\right) + \left(\frac{y_c+\sqrt{2}}{\#_4} - \frac{y_c-\sqrt{2}}{\#_3}\right)\left(\frac{y_c}{\#_1} - \frac{y_c}{\#_2}\right) \tag{S29}$$

$$c = \left(\frac{y_c+\sqrt{2}}{2\#_4} - \frac{y_c-\sqrt{2}}{2\#_3}\right)^2 + \left(\frac{x_c}{2\#_3} - \frac{x_c}{2\#_4}\right)^2 \tag{S30}$$

$$d = \frac{1}{2\#_1} - \frac{1}{2\#_2} + \frac{{y_c}^2}{{\#_1}^3} - \frac{{y_c}^2}{{\#_2}^3} \tag{S31}$$

$$e = \frac{1}{2\#_3} - \frac{1}{2\#_4} + \frac{{x_c}^2}{{\#_3}^3} - \frac{{x_c}^2}{{\#_4}^3} \tag{S32}$$

$$f = x_c\left(\frac{x_c+\sqrt{2}}{2\#_2} - \frac{x_c-\sqrt{2}}{2\#_1}\right) + y_c\left(\frac{y_c}{2\#_1} - \frac{y_c}{2\#_2}\right) \tag{S33}$$

$$g = y_c\left(\frac{y_c+\sqrt{2}}{2\#_4} - \frac{y_c-\sqrt{2}}{2\#_3}\right) + x_c\left(\frac{x_c}{2\#_3} - \frac{x_c}{2\#_4}\right) \tag{S34}$$

The unspecified points in the coefficients are related to $x_c, y_c = \pm\sqrt{2}/2$. These points are located on the circle boundary. As a result, the numerical value of either coefficient f or g are not bounded in the case of derivatives in the boundary condition (Neumann or Robin boundary conditions). However, the absolute values of these two coefficients are the same. This implies

that for (x_c, y_c)=($\sqrt{2}/2$, $\sqrt{2}/2$), ($\sqrt{2}/2$, $-\sqrt{2}/2$), ($-\sqrt{2}/2$, $\sqrt{2}/2$), ($-\sqrt{2}/2$, $-\sqrt{2}/2$), the Eqs. (55)-(56) can be simplified to the below equation:

$$\boldsymbol{sign}(\mathbf{f}_{i,j}) \sum_{k=1}^{N_x} \mathbf{A}_{x,i,k} \frac{\partial \boldsymbol{\theta}_{k,j}}{\partial t} + \boldsymbol{sign}(\mathbf{g}_{i,j}) \sum_{k=1}^{N_y} \mathbf{A}_{y,j,k} \frac{\partial \boldsymbol{\theta}_{i,k}}{\partial t} = 0 \qquad \text{(S35)}$$

4. Discretized Navier-Stokes equations

In this section, the discretized form of the simplified Navier-Stokes equations for two and three-phase gravity flows in sloped pipes are presented.

4.1. Two-phase gravity flow in sloped pipes

The mapped form of Eq. (74) can be discretized using orthogonal collocation technique for internal nodes are as below:

$$\mathbf{a}_{i,j} \sum_{k=1}^{N_x} \mathbf{B}_{x,i,k}\, \mathbf{U}_{k,j} + \frac{\mathbf{b}_{i,j}}{(y_o+1)} \sum_{k=1}^{N_x} \sum_{l=1}^{N_y} \mathbf{A}_{x,k,i} \mathbf{A}_{y,j,l} \mathbf{U}_{k,l} + \frac{\mathbf{c}_{i,j}}{(y_o+1)^2} \sum_{k=1}^{N_y} \mathbf{B}_{y,j,k}\, \mathbf{U}_{i,k} + \mathbf{d}_{i,j} \sum_{k=1}^{N_x} \mathbf{A}_{x,i,k}\, \mathbf{U}_{k,j} + \frac{\mathbf{e}_{i,j}}{(y_o+1)} \sum_{k=1}^{N_y} \mathbf{A}_{y,j,k}\, \mathbf{U}_{i,k} + \frac{R^2 \rho g \sin(\alpha)}{\mu} = 0 \quad \forall\, i = 2, \dots, N_x - 1 \quad \& \quad \forall\, j = 2, \dots, N_y - 1 \qquad \text{(S36)}$$

The no-slip velocity boundary condition at the pipe wall (Eq. (75)) is as below.

$$\mathbf{U}_{i,j} = \mathbf{0} \quad \forall\, i = 1, N_x \quad \& \quad \forall\, j = 1, \dots, N_y \qquad \text{(S37)}$$

$$\mathbf{U}_{i,j} = \mathbf{0} \quad \forall\, i = 2, \dots, N_x - 1 \quad \& \quad \forall\, j = 1 \qquad \text{(S38)}$$

The boundary condition at free liquid surface (Eq. (76)) is as below.

$$\left(\frac{x_{c,i} y_{c,j}}{(1-y_{c,j}^2)^{3/2}}\right) \sum_{k=1}^{N_x} \mathbf{A}_{x,i,k}\, \mathbf{U}_{k,j} + \frac{\mathbf{1}}{(y_o+1)} \sum_{k=1}^{N_y} \mathbf{A}_{y,j,k}\, \mathbf{U}_{i,k} = 0 \quad \forall\, i = 2, \dots, N_x - 1 \quad \& \quad \forall\, j = N_y \qquad \text{(S39)}$$

The discretized form of continuity equation (Eq. (80)) reads as:

$$Q = R^2 (y_o + 1) \sum_{k=1}^{N_x} \sum_{l=1}^{N_y} \sqrt{1 - y_{s,l}^2}\, \mathbf{q}_{x,k} \mathbf{q}_{y,l} \mathbf{U}_{k,l} \qquad \text{(S40)}$$

4.2. Three-phase gravity flow in sloped pipes

The mapped form of Eqs. (81)-(82) can be discretized using orthogonal collocation technique for internal nodes are as below:

$$\mathbf{a}_{i,j}\sum_{k=1}^{N_x}\mathbf{B}_{x,i,k}\,\mathbf{U}_{k,j}^{h}+\frac{\mathbf{b}_{i,j}}{(y_i+1)}\sum_{k=1}^{N_x}\sum_{l=1}^{N_y^h}\mathbf{A}_{x,k,i}\mathbf{A}_{y,j,l}\mathbf{U}_{k,l}^{h}+\frac{\mathbf{c}_{i,j}}{(y_i+1)^2}\sum_{k=1}^{N_y^h}\mathbf{B}_{y,j,k}\,\mathbf{U}_{i,k}^{h}+$$

$$\mathbf{d}_{i,j}\sum_{k=1}^{N_x}\mathbf{A}_{x,i,k}\,\mathbf{U}_{k,j}^{h}+\frac{\mathbf{e}_{i,j}}{(y_i+1)}\sum_{k=1}^{N_y^h}\mathbf{A}_{y,j,k}\,\mathbf{U}_{i,k}^{h}+\frac{R^2\rho_h g\sin(\alpha)}{\mu_h}=0\quad\forall\, i=2,\dots,N_x-1\quad\&\quad\forall\, j=2,\dots,N_y^h-1 \tag{S41}$$

$$\mathbf{a}_{i,m}\sum_{k=1}^{N_x}\mathbf{B}_{x,i,k}\,\mathbf{U}_{k,m}^{l}+\frac{\mathbf{b}_{i,m}}{(y_o-y_i)}\sum_{k=1}^{N_x}\sum_{l=1}^{N_y^l}\mathbf{A}_{x,k,i}\mathbf{A}_{y,m,l}\mathbf{U}_{k,l}^{l}+$$

$$\frac{\mathbf{c}_{i,m}}{(y_o-y_i)^2}\sum_{k=1}^{N_y^l}\mathbf{B}_{y,m,k}\,\mathbf{U}_{i,k}^{l}+\mathbf{d}_{i,m}\sum_{k=1}^{N_x}\mathbf{A}_{x,i,k}\,\mathbf{U}_{k,m}^{l}+\frac{\mathbf{e}_{i,m}}{(y_o-y_i)}\sum_{k=1}^{N_y^l}\mathbf{A}_{y,m,k}\,\mathbf{U}_{i,k}^{l}+\frac{R^2\rho_l g\sin(\alpha)}{\mu_l}=$$

$$0\quad\forall\, i=2,\dots,N_x-1\quad\&\quad\forall\, m=2,\dots,N_y^l-1 \tag{S42}$$

The discretized form of continuity equation (Eqs. (83)-(84)) reads as:

$$Q_h=R^2(y_i+1)\sum_{k=1}^{N_x}\sum_{l=1}^{N_y^h}\sqrt{1-y_{s,l}^2}\,\mathbf{q}_{x,k}\mathbf{q}_{y,l}\mathbf{U}_{k,l}^{h} \tag{S43}$$

$$Q_l=R^2(y_o-y_i)\sum_{k=1}^{N_x}\sum_{l=1}^{N_y^l}\sqrt{1-y_{s,l}^2}\,\mathbf{q}_{x,k}\mathbf{q}_{y,l}\mathbf{U}_{k,l}^{l} \tag{S44}$$

The no-slip velocity boundary condition at the pipe wall (Eq. (85)) is as below.

$$\mathbf{U}_{i,j}^{h}=\mathbf{0}\quad\forall\, i=1,N_x\quad\&\quad\forall\, j=1,\dots,N_y^h \tag{S45}$$

$$\mathbf{U}_{i,j}^{h}=\mathbf{0}\quad\forall\, i=2,\dots,N_x-1\quad\&\quad\forall\, j=1 \tag{S46}$$

$$\mathbf{U}_{i,m}^{l}=\mathbf{0}\quad\forall\, i=1,N_x\quad\&\quad\forall\, m=1,\dots,N_y^l \tag{S47}$$

The boundary condition at free light liquid surface (Eq. (86)) is as below.

$$\left(\frac{x_{c,i}y_{c,m}}{(1-y_{c,m}^2)^{3/2}}\right)\sum_{k=1}^{N_x}\mathbf{A}_{x,i,k}\,\mathbf{U}_{k,m}^{l}+\frac{\mathbf{1}}{(y_o-y_i)}\sum_{k=1}^{N_y^l}\mathbf{A}_{y,m,k}\,\mathbf{U}_{i,k}^{l}=0\quad\forall\, i=2,\dots,N_x-1\quad\&\quad\forall\, m=N_y^l \tag{S48}$$

The discretized form of continuity equations for liquid-liquid interface (Eqs. (87)-(88)) reads as:

$$\mu_h \left[\left(\frac{x_{c,i} y_{c,j}}{(1-y_{c,j}^2)^{3/2}} \right) \sum_{k=1}^{N_x} \mathbf{A}_{x,i,k}\, \mathbf{U}_{k,j}^{h} + \frac{\mathbf{1}}{(y_i+1)} \sum_{k=1}^{N_y^h} \mathbf{A}_{y,j,k}\, \mathbf{U}_{i,k}^{h} \right] =$$

$$\mu_l \left[\left(\frac{x_{c,i} y_{c,m}}{(1-y_{c,m}^2)^{3/2}} \right) \sum_{k=1}^{N_x} \mathbf{A}_{x,i,k}\, \mathbf{U}_{k,m}^{l} + \frac{\mathbf{1}}{(y_o-y_i)} \sum_{k=1}^{N_y^l} \mathbf{A}_{y,m,k}\, \mathbf{U}_{i,k}^{l} \right] \qquad \text{(S49)}$$

$$\mathbf{U}_{i,j}^{h} = \mathbf{U}_{i,m}^{l} \quad \forall\, i = 2, \dots, N_x - 1 \quad \& \quad \forall\, j = N_y^h \quad \& \quad \forall\, m = 1 \qquad \text{(S50)}$$

5. MATLAB Programs

The list of the attached MATLAB m-files are as below:

- ✓ colloc.m

  This program calculates collocation weights (1996, 1997 John W. Eaton).

- ✓ solver_segment_2PhaseFlow_NonLinSolver.m

  This program simulates steady laminar gravity flow in a pipe (described by a simplified 2D steady-state incompressible Navier-Stokes equation). Squelched mapping and orthogonal collocation technique are used together for the discretization. The solution technique is solving momentum equation using a direct method (LU decomposition) for the linear system of equations followed by a nonlinear solver for the continuity equation.

- ✓ solver_segment_3PhaseFlow_NonLinSolver.m

  This program simulates steady laminar gravity 3phase flow in a pipe (described by a simplified 2D steady-state incompressible Navier-Stokes equation). Squelched mapping and orthogonal collocation technique are used together for discretization. The solution technique is solving momentum equation using the direct method (LU decomposition) for the linear systems of equation followed by a nonlinear solver for the continuity equation.

- ✓ solver_SteadyState.m

  This program discretizes a linear steady-state diffusion equation in a circle using three techniques: elliptical mapping, squelched mapping, and polar coordinate, and solves the linear system of equation using the direct method (LU decomposition).

- ✓ solver_transient.m

  This program discretizes a transient diffusion equation in a circle using three techniques: elliptical mapping, squelched mapping, and polar coordinate and solves the ODE system using adaptive ode solver (ode15s).

- ✓ symbolic_coefficient_analysis.m

  This program derives the analytical geometrical mapping coefficients for a Laplace equation using symbolic analysis.

Chapter 7

7. Conclusion and recommendation

7.1. Summary of conclusions

In this project, a model library was developed using the population balance modeling approach for separation and transport processes involving oil and water emulsions. Various models were built to cater to different applications and processes in oil and gas industry, each varying in complexity. The following paragraphs present the primary conclusions drawn from the different models that were developed and employed to investigate various aspects of these processes.

Equilibrium and transient behaviors of a PBM

A novel approach was developed to estimate the equilibrium and transient properties of a system described by a spatially homogenous population balance model. This technique estimates the length and time scales of the system for breakage and coalescence relations through straightforward relationships associated with a dimensionless group. These scales rely on an estimated equilibrium DSD and can be employed to predict the probable direction and rate of evolution of the distribution.

The results were applied to tackle the well-known challenge related to computational efficiency and robustness when solving PBMs. The approximate equilibrium length scales obtained were utilized to construct element-based orthogonal collocation grids for PBMs. At the same time, the timescale can guide the determination of a suitable simulation time to attain steady-state conditions. Additionally, to achieve the steady-state DSD, the study recommends conducting a transient solution with the estimated equilibrium DSD as the initial condition.

Batch gravity separation

A novel method was developed to model the formation of a DPL within a batch gravity separator. This approach involves introducing an effective diffusion mechanism into the model. Consequently, a model was put forth for the effective diffusion coefficient, ensuring that the system's volume fraction remains within physically limits. This

approach was then incorporated into a comprehensive model for the batch gravity separation process. The developed model takes into account gravity-induced settling / rising of droplets, binary and interfacial coalescence. Additionally, the model tracks the interface between the dispersion layer and the homogenous phase as the homogenous phase grows. To validate its accuracy, the proposed closure model for the effective diffusion coefficient was successfully fine-tuned using experimental data obtained through the NMR technique.

Continuous gravity separation

A comprehensive model was developed for 3-phase separators, divided into two main segments: the inlet section and the separation section, separated by a calming baffle.

The inlet section model incorporates a spatially homogeneous PBM that accounts for the turbulent breakage and coalescence of droplets. The calculation of the turbulent energy dissipation rate was done utilizing an averaging strategy, taking into consideration the dynamic head of the multiphase stream in the inlet pipe.

Moving on to the separation section model, it encompasses hydrodynamic models and dispersion models. The hydrodynamic models take care of the transported fluid volume between the dispersion layers as well as the velocity profiles while the dispersion models consider turbulent-induced breakage and coalescence as well as buoyancy-induced coalescence. This versatility enables the model's application under normal operational conditions as well as during upset processes like start-up and shut-down scenarios.

In this study, we also developed a mathematical expression for the interfacial coalescence time of droplets. This expression is derived from the difference between gravitational and buoyant forces within a dense packed layer. Consequently, it enables us to establish a relationship between the thickness of the DPL and the rate of interfacial coalescence.

Furthermore, transient level dynamics have been integrated into the model, enabling the study of control schemes and transient upset conditions. To facilitate this, two separate solvers have been developed to handle both steady-state and transient problems.

To validate the mathematical model, predictions were compared against experimental data gathered from a multi-pipe separator, which shows good agreement.

Application of geometrically transformed spectral methods for multiphase flow

The study focused on the spectral discretization of 2D circular geometries using the orthogonal collocation technique, leveraging the geometrical mapping approach. These developed methods offer effective solutions to address the challenges linked to polar discretization. Furthermore, the squelched mapping technique extends the spectral discretization capabilities to irregular circular segment geometries frequently encountered in multiphase flow scenarios within pipes and separators.

Consequently, user-friendly and computationally efficient numerical procedures have been devised to solve PDEs within circular geometries, accommodating various boundary conditions for both steady-state and transient problems. Various aspects of these techniques, including error properties, condition number, and computational efficiency, underwent evaluation.

Furthermore, this technique was successfully utilized in discretizing the simplified Navier-Stokes equations, particularly for two and three-phase multiphase gravity flows in sloped pipes.

Key Insights and Contributions

In summary, this research work aimed to contribute to the field of oil/water emulsion separation and transport processes in the oil and gas industries. The goal was to propose mathematical models for various processes and equipment related to complex multiphase systems, utilizing a population balance modeling approach. Special attention was dedicated to developing techniques for the efficient numerical analysis of these models with varying complexity.

The study aimed to bridge theoretical insights with practical applications by incorporating experimental data for model validation. In parallel with the theoretical efforts, there was a dedicated initiative to compile these findings into a C++ modular model library for multiphase fluid systems. The primary objective of this library is to furnish researchers and engineers with practical tools for simulating, fine-tuning models, and optimizing separation/transportation processes.

7.2. Recommendations for future works

There is great potential to continue this project either by focusing on applying the developed models or extending the library to more complex / realistic systems. Some of the possibilities to continue the work are listed below:

Comprehensive modeling of subsea oil water separation

It is possible to comprehensively consider various elements of the process within a unified model. The key components in this context include the choke valve, the gathering subsea flowline, and the pipe separator. The model library enables us to construct a modular model suitable for both steady-state and transient conditions.

The steady-state model serves as a tool to investigate the influence of different operational parameters on separation efficiency. These parameters encompass choke pressure drop, pipe separator level, flow rate, volume fraction, as well as design factors like the length and diameter of the pipe separator. Through these studies, optimal designs can be explored for diverse operational scenarios. It is crucial to collaborate closely with experimental findings from an pipe separator to fine-tune the model.

In a subsequent phase, we can investigate the impact of transient disturbances, such as flow fluctuations and potential slugs, on the performance of the pipe separator using the transient model. Consequently, we can analyze and propose a control system tailored to these disturbances.

Extending the model library for more realistic pipe flow applications

Three new modules can be added as below:

- Steady-state model for fully turbulent oil/water vertical pipe,
- Steady-state model for fully turbulent oil/water horizontal pipe,
- Pressure changing element (e.g., pumps, valves, fittings, chokes, etc.) with variable turbulence intensity in the downstream piping.

The mentioned modules can be used to evaluate the piping system's uniformity requirement, which is critical for the design and evaluation of autosamplers used for BS&W (base sediment and water) measurement in surface and custody metering facilities according to API MPMS 8.2 and ISO-3171.

The primary phenomena that need to be captured in a pipe includes the turbulent dispersion of droplets and the radially varying turbulent energy dissipation rate. These factors lead to varying rates of droplet breakage and coalescence along the pipe's radius. To address these phenomena in a vertical pipe, it is necessary to develop steady-state models that account for both radial and axial dependencies and employ a model to capture the turbulent flow properties.

In the case of modeling a horizontal pipe, in addition to the factors mentioned above, one must also account for the effect of gravity. Consequently, a 3D-PBM model is essential to accurately capture this gravitational impact.

To model pressure-changing elements, a steady-state 1D-PBM can be utilized. However, it's crucial to consider the axially variable turbulent energy dissipation rate in the downstream pipe.

A realistic 3D CFD-PBM model for a 3-phase separator

Another module that can be incorporated into the library involves creating a separation-section model for a 3-phase separator that simultaneously considers the Navier-Stokes equations and PBM. This 3D, realistic separator model will enable us to account for the impact of nozzle location and weir arrangement on the separation efficiency of the equipment. Furthermore, a turbulent model can enhance capturing the effects of spatially distributed energy dissipation rate on droplets breakage and coalescence rates.

To develop this model, one can utilize the technique developed through squelched mapping and spectral techniques to discretize the irregular geometries that emerge in multi-phase flow within the separator. This approach leverages the capabilities of spectral techniques for discretization, enabling the use of a coarse grid while preserving the numerical accuracy of the solution.

Developing population balance models for electrostatic dehydration and desalting process

The library modules can be employed to simulate an electrical dehydrator and desalter effectively. This can be achieved by utilizing a 0D-PBM module for the mixing valve and a 1D-PBM module for the separation section. Research in this area can be advanced by establishing a coalescence closure model, which establishes a connection between the

coalescence rate and the physio-chemical properties of the fluid as well as the applied electrical field. Subsequently, the proposed closure model can be fine-tuned using either experimental data or field data.

Enriching the library's numerical techniques

Various problems may find value in distinct numerical methods, particularly those related to discretizing the droplet size domain. Furthermore, the library's code architecture accommodates the integration of additional functions for discretizing birth and death source terms. This flexibility enables a broader range of users to take advantage of alternative techniques, each offering unique features such as computational efficiency and conservation properties. Therefore, an option worth considering is the incorporation of additional techniques, such as the finite volume method, to expand the library's capabilities.

Utilizing the squelch mapping and spectral techniques to handle irregular geometries

The technique developed using squelched mapping and spectral techniques can be extended to almost all 2D irregular geometries. To accomplish this, it is necessary to delineate the geometry's boundary either analytically or by employing interpolation techniques. We have established the underlying concept, and we are planning to publish a paper on this topic in the near future.

Further development of the effective diffusion model for DPL prediction

The effective diffusion model developed in this study effectively captures the primary functionality of the dispersed phase volume fraction. Nevertheless, there remains two adjustable parameters within this model: the model coefficient and the maximum volume fraction parameter. These parameters can be further refined to encompass the characteristics of fluid physical properties and droplet size distributions. The model coefficient is directly proportional to interfacial tension and inversely correlated with the phase density difference. Meanwhile, the maximum volume-fraction parameter relies on two key factors: polydispersity (can be quantified by the standard deviation of the DSD), and deformation (related to the compressive force within the DPL, surface tension as well

as droplet size). Exploring further refinement of these parameters is an interesting future research, possibly necessitating a broader range of experimental cases with greater variations in DSDs.

ISBN 978-82-326-7586-9 (printed ver.)
ISBN 978-82-326-7585-2 (electronic ver.)
ISSN 1503-8181 (printed ver.)
ISSN 2703-8084 (online ver.)

NTNU
Norwegian University of
Science and Technology